



Energy Performance Enhancement of Crystalline
Silicon Photovoltaic Solar Cells

A thesis submitted for the degree of Doctor of Philosophy

by

Abdulla Tahhan

Department of Mechanical, Aerospace and Civil Engineering

College of Engineering, Design and Physical Sciences

Brunel University

2016

Abstract

The work in this thesis examines the effects of the application of oxide coatings on the performance of the single crystalline silicon photovoltaic solar cells. A variety of potential oxide materials for solar cells performance enhancement are investigated. These films are silicon oxide, titanium oxide and rare earth ion-doped gadolinium oxysulfide phosphor. This study compares the electrical characteristics, optical properties and surface chemical composition of mono-crystalline silicon cells before and after coating.

The first study investigates the potential for using single and double layers of silicon oxide films produced by low-temperature Plasma Enhanced Chemical Vapour Deposition (PECVD) using tetramethylsilane as a silicon precursor and potassium permanganate oxidising agent for efficiency enhancement of solar cells at low manufacturing cost. Deposition of the films contributes to the increase of the conversion energy of the solar cells on one hand while the variety of colours obtained in this study can be of great importance for building-integrated photovoltaic application on the other hand. The obtained results demonstrated a relative enhancement of 3% in the conversion efficiency of the crystalline silicon solar cell.

In the second study, the effects of using a single layer of titanium oxide and a stack of silicon oxide and titanium oxide on the performance of solar cell are demonstrated. Moreover, this study shows the use of different sputtering configurations and oxidation methods. The experimental results showed a relative enhancement of 1.6% for solar cells coated with a stack of silicon oxide/titanium oxide.

In the third study, silicon cells were coated with a luminescent layer consisting of down-converting phosphor, gadolinium oxysulfide doped with erbium and terbium, and a polymeric binder of EVA using doctor-blade screen printing technique. A relative enhancement of 4.45% in the energy conversion efficiency of PV solar cell was achieved. Also, the effects of combining silicon oxide layers together with the luminescent composite are also presented in this study.

Acknowledgements

This work would never see the light without the support from my family. This work is the least I could bring back home after their long term sacrifice providing me with the best possible education opportunity throughout my life.

I can not express my sincere gratitude to Dr Zahir Dehouche and Dr George Fern. It is been a privilege to work with this supervisory team. I feel like I absorbed how to be energetic and creative with science just being around them.

I would like to thank many people who provided me with guidance, training and assistance in the laboratories during my study at Brunel. I would like to thank the staff from the Experimental Techniques Centre at Brunel University, including Prof Tony Anson and Mr Nico Nelson for their expertise in PECVD processes, Mrs Nita Verma and Dr Ashley Howkins for TEM and SEM imaging, Dr Terry Ireland for his help for introducing for chemistry lab and photoluminescence measurements, Mr Alex Metcalfe for his expertise in sputtering techniques and Dr Lorna Anguilano for XRD Analysis. Also, I would like to thank Mr Erik Haverkamp from ReRa solutions for quantum efficiency measurements.

I would like to express my appreciations to all my colleagues and friends at Brunel University for their help and support.

Declaration

I declare that this thesis is the result of my work and includes nothing which is the outcome of work done in collaboration except where explicitly indicated in the acknowledgement. This thesis is an account of research undertaken for the degree of doctor of philosophy at Centre for Energy and Built Environment Research, Brunel University London, Uxbridge, Middlesex, UK. This thesis has not been previously submitted for a degree or examination in any institution.

Signed:

Abdulla Tahhan

Date:

Contents

1	Introduction	1
1.1	Motivation	3
1.2	Thesis Layout	4
2	Background	5
2.1	Solar Irradiation	5
2.2	Type of Solar Cells	10
2.2.1	First Generation PV	10
2.2.1.1	Monocrystalline Solar Cells	11
2.2.1.2	Multicrystalline Solar Cells	11
2.2.1.3	Ribbon Solar Cells	11
2.2.2	Second Generation PV	12
2.2.2.1	Amorphous Silicon Cells	12
2.2.2.2	Copper Indium Selenide Cells	13
2.2.2.3	Cadmium Telluride Cells	13
2.2.3	Third Generation PV	14
2.2.3.1	Dye Sensitised and Organic cells	14
2.2.3.2	Perovskite Solar Cell	15
2.2.3.3	The Multi-Junction III-V Solar Cells	16
2.3	Principles of Solar Cells Operation	19
2.4	IV Characteristic of C-Si Solar Cell	20

2.4.1	Practical Solar Cells Devices	23
2.4.2	Design of Antireflection Coatings	25
2.4.3	Quantum Efficiency	28
2.5	Energy Losses of p-n Junction Solar Cell	29
2.5.1	Energy Losses of Ideal Solar Cell	29
2.5.2	Energy Losses of Real Solar Cell	31
2.6	Shockley-Queisser Limit	33
2.7	Improving Conversion Efficiency of PV Cells	34
2.7.1	Spectral Conversion	34
2.8	Building Integrated Photovoltaics	37
3	Characterization of Crystalline Silicon Solar Cells	40
3.1	Silicon Solar Cells	40
3.2	Preparation of Silicon Solar Cells	41
3.3	Electrical Measurements of the Solar Cells	42
3.4	Material Deposition Machines	46
3.4.1	PECVD Machine	46
3.4.2	Sputtering Deposition Process and QBox	46
3.4.2.1	DC Sputtering	47
3.4.2.2	RF Sputtering	48
3.4.2.3	QBox Series System	48
3.5	UV/Vis Spectrophotometer	49
3.6	Scanning Electron Microscopy	51
3.6.1	SEM Sample Preparation	52
3.6.1.1	Epoxy Preparation	53
3.6.1.2	Sputter Coater	53
3.7	High Pressure Stirred Reactor and Furnace	53
3.8	Phosphor Material Characterization	55

3.8.1	X-ray Powder Diffraction	55
3.8.2	Photo-luminescence Spectroscopy	56
3.8.3	Differential Scanning Calorimetry	56
3.9	Measurements	57
4	Silicon Oxide for PV Solar Cell	60
4.1	Introduction	61
4.2	Related Work	62
4.3	Experimental Method	64
4.3.1	Silicon Precursor	64
4.3.2	Oxidation Agent	68
4.3.3	PECVD Coating Process	69
4.4	Results and Discussion	72
4.5	Summary	81
5	Titanium Oxide for PV Solar Cell	83
5.1	Introduction	84
5.2	Related work	86
5.3	Experimental Method	87
5.3.1	Deposition of Thin Films	87
5.4	Results and Discussion	91
5.4.1	Single Layer Titanium Oxide	91
5.4.2	Energy Band Gap	97
5.4.3	Double Layers Titanium/Silicon Oxide	101
5.5	Summary	105
6	Phosphor for PV Solar Cell	106
6.1	Introduction	107
6.2	Aim and Objectives	109

6.3	Related Work	110
6.3.1	Energy Enhancement Using Luminescence Species	110
6.3.2	Encapsulation of the Luminescence Species	111
6.4	Experimental Method	111
6.4.1	Materials	111
6.4.1.1	Luminescent Material	111
6.4.2	Binder	116
6.4.3	Solvent	117
6.4.4	Coating Process	118
6.4.4.1	EVA Layer	119
6.4.4.2	EVA+Phosphor Preparation	119
6.4.4.3	Layer Application	119
6.5	Results and Discussion	122
6.5.1	EVA Layer	122
6.5.2	EVA/Phosphor Layer	125
6.5.2.1	Optical Properties	125
6.5.2.2	Electrical Characteristics	126
6.5.3	Microstructure of the Phosphor-Coated Solar Cell	132
6.5.4	Combined EVA/Phosphor/Silicon Oxide layer	134
6.6	Conclusion	138
7	Conclusions and Future Work	139
	References	143
	Appendices	156

List of Figures

2.1	The radiation spectrum of a black body at 5762K compared with solar AM0 and AM1.5 global spectra.	6
2.2	A sketch showing definitions for AM factor	8
2.3	Average hourly radiation data for each month of the year in W/m ² for Gatwick, London.	9
2.4	PV technologies tree.	10
2.5	A schematic of amorphous silicon p-i-n solar cell structure.	12
2.6	A schematic of the structure of Pervoskite solar cell.	15
2.7	A schematic structure of 3,4,5,6 junctions solar cell with their maximum theoretical efficiency.	17
2.8	Timeline of solar cell energy conversion efficiencies records.	18
2.9	Schematic of the fundamental architecture of a p-n junction Si solar cell	20
2.10	The equivalent circuit model of an ideal solar cell.	20
2.11	I-V characteristics curves of p-n junction solar cell under dark and light illumination conditions	21
2.12	The equivalent circuit model of a practical solar cell.	24
2.13	Effects of parasitic resistances: (A) series and (B) on the I-V curve. . .	24
2.14	Energy band diagram of p-n junction under illumination.	29
2.15	Spectral distribution of sunlight and energy losses	30
2.16	Schematic of a photovoltaic solar cell with down-converter layer on top (left) and up-converter layer on the backside of the solar cell (right) . .	35

2.17	Schematics of energy diagrams demonstrating and subsequent down- conversion, downshifting and upconversion	36
2.18	Photographs showing different examples of the BIPV systems.	38
2.19	Various colours of solar cells can be obtained in the PECVD coating.	39
3.1	Motech crystalline silicon solar cell	41
3.2	Laser cutter (Top), software set-up in computer (Left) and solar cell layout on laser cutter (Right).	43
3.3	Electrical measurements set up.	43
3.4	Spectral distribution of the illumination source	44
3.5	Reference cell calibrated by GBsol	45
3.6	Schematic of the Mask used in the electrical measurements.	45
3.7	Photograph of PECVD Coating System.	47
3.8	Photographs of the Mantis deposition system - QBox Series System.	49
3.9	Photograph of PerkinElmer Precisely Lambda 650S UV/Vis Spectrom- eter.	50
3.10	ZEISS SUPRA 35 VP Scanning Electron Microscope.	52
3.11	Polarab sputter coater.	54
3.12	High pressure stirred reactor and furnace.	55
3.13	Bentham M300 monochromator detector system (left) and Bruker D8 ADVANCED X-ray powder diffractometer (right).	57
3.14	Differential scanning calorimetry system.	58
4.1	Tetramethylsilane molecular structure.	65
4.2	Photographs of the TMS-coated solar cells at different coating conditions.	67
4.3	The schematic structures of commercial solar cell before and after coat- ing with a single and double layer of silicon oxide.	69
4.4	Schematic of the PECVD reactor and the substrate positioning.	70

4.5	I-V curves of solar cells before and after coating with single layer of silicon oxide film under UV light illumination.	72
4.6	Reflection spectra of the coated and uncoated solar cells with single anti-reflection layer of silicon oxide.	74
4.7	Efficiency versus KMnO_4 mass under visible and ultraviolet light illumination.	75
4.8	Reflection spectra of coated cells with double anti-reflection coating. . .	76
4.9	Photographs of mono-crystalline silicon solar cell coated with double layers of silicon oxide.	77
4.10	I-V and P-V curves of the coated cell at the maximum enhancement obtained under visible light illumination.	78
4.11	Absorption and reflection spectra of the single and double anti-reflection layers for solar cells with optimum enhancement obtained.	79
4.12	EDX spectrum of the coated and uncoated solar cell.	80
5.1	Schematic of the Qbox sputtering system.	87
5.2	Schematic shows PECVD configuration for oxidation process.	89
5.3	Thickness of Ti oxidised to TiO_2 versus the required time.	90
5.4	Flow chart illustrates the coating steps.	91
5.5	Efficiency drop of solar cells coated with plasma oxidised titanium films. . .	92
5.6	I-V curve of the solar cell coated 4 nm titanium before and after plasma oxidation.	93
5.7	Absorption spectra of titanium films processed by plasma oxidation. . .	93
5.8	Efficiency drop using different techniques.	94
5.9	Absorption spectra of 4 nm TiO_2 coated with various conditions.	95
5.10	Transmission spectra of 4 nm TiO_2 coated with various conditions. . .	96
5.11	Illustration of the steps for preparation of titanium dioxide nanoparticles. . .	97
5.12	TEM images of Anatase (aerogel) titanium dioxide nanoparticles.	98

5.13	XRD patterns of Anatase (aerogel) titanium dioxide nanoparticles.	98
5.14	Energy bandgap obtained by extrapolating the linear portion of the versus $h\nu$ curve.	99
5.15	Titanium coated slides using plasma and thermal annealing.	100
5.16	Reflection spectra of double layer coating.	101
5.17	Transmission spectra of double layer coating.	102
5.18	Absorption spectra of double layer coating.	103
5.19	I-V and P-V curve of solar cells with double layer coating.	104
6.1	Typical spectral response (SR) vs wavelength of Motech silicon photo- voltaic solar cell	107
6.2	Operating principle of the luminescent material	108
6.3	SEM images of $Gd_2O_2S(Er_{0.2},Tb)_{0.01}$ particles.	112
6.4	XRPD patterns of Tb^{3+} and Er^{3+} co-doped Gd_2O_2S	113
6.5	Luminescent material used in the experiment.	114
6.6	PLE and PL of the phosphor at room temperature.	115
6.7	Emission of the phosphor at different temperatures.	115
6.8	Chemical structures of ethylene and vinyl acetate monomers and poly (ethylene vinyl acetate)	117
6.9	EVA+Phosphor coated (top) and EVA coated (bottom) solar cell under UV light excitation.	120
6.10	Doctor blade screen printing technique.	121
6.11	A schematic of the textured mono-crystalline solar cell with DC layer. .	121
6.12	The first (blue) and second (green) heating curve of raw EVA material.	122
6.13	Transmission spectra for EVA layers dissolved in different concentra- tions of the solvent.	123
6.14	Reflection spectra for EVA layers dissolved in different concentrations of the solvent.	124

6.15	I-V curve of EVA coating before and after heat treatment.	125
6.16	Comparison of reflectance spectra for uncoated and coated cells.	126
6.17	I-V and P-V curves of the solar cells at the maximum enhancement.	127
6.18	Efficiency enhancement of the coated solar cells.	128
6.19	Transmission spectra of the Phosphor+EVA layers.	129
6.20	Absorption spectra of the Phosphor+EVA layers.	130
6.21	Temperature coefficient of solar cells.	130
6.22	IQE spectra of the solar cells.	131
6.23	Cross section SEM image of the coated cell with EVA+phosphor.	132
6.24	EDX spectrum and top SEM image of the coated solar cell with EVA and phosphor.	133
6.25	EDX images of the EVA + Phosphor (left) and EVA (right) coated cell.	133
6.26	A schematic of the textured mono-crystalline solar cell with SiO ₂ and DC layers.	135
6.27	Transmission and absorption spectra of the layers.	136
6.28	Conversion efficiency of the solar cells.	136
1	Schematic of the temperature data acquisition system.	161
2	Calibration of thermocouples and data logger.	162
3	Calibration curve for thermocouples.	162

List of Tables

2.1	Confirmed efficiencies of solar cells and commercial PV modules	17
3.1	Spectral distribution with percentage contributions for each wavelength band.	44
4.1	Physical and chemical properties of TMS.	65
4.2	Summary of the coating conditions for solar cells using TMS precursor.	66
4.3	Summary of the coating conditions for solar cells with a single anti- reflection layer of silicon oxide.	70
4.4	Summary of the coating conditions for solar cells with a double anti- reflection layer of silicon oxide.	71
4.5	Electrical characteristics of the uncoated (S_0) and coated cells ($S_1, S_2,$ S_3, S_4, S_5, S_6) under UV light illumination.	73
4.6	Electrical characteristics of the uncoated (S_0) and coated cells ($S_1, S_2,$ S_3, S_4, S_5, S_6) under visible light illumination.	76
4.7	Electrical characteristics of the uncoated (D_0) and coated solar cells (D_1, D_2, D_3) under visible light illumination.	77
4.8	Values of the EDX spectra of the coated silicon solar cells (S_2, S_3, S_4).	81
5.1	The deposition conditions of titanium films.	88
5.2	Summary of the coating conditions of silicon oxide layer for solar cells with a double anti-reflection layer of silicon oxide/titanium oxide. . . .	90

5.3	Electrical characteristics of the uncoated and coated cells with a double anti-reflection layers.	104
6.1	Crystal size and lattice parameters of the phosphor particles.	113
6.2	Physical properties of the solvents	118
6.3	Electrical characteristics of the uncoated and coated cells.	127
6.4	Values of the EDX spectra of the coated silicon solar cells with EVA+phosphor and EVA only.	134
6.5	Electrical characteristics of the uncoated and coated cells.	137
1	Physical properties of the Sn-Pb-Ag solder	160
2	Calibration data for 1.5 mm thermocouple.	163

Nomenclature

Roman Symbols

I	Current	A
FF	Fill factor	–
I_{mp}	Maximum power current	A
P_{max}	Maximum power point	W
V_{mp}	Maximum power voltage	V
V_{oc}	Open circuit voltage	V
E_{ph}	Photon energy	eV
E_g	Semiconductor bandgap energy	eV
I_{sc}	Short circuit current	A
R_{sh}	Shunt resistance	Ω
A	Solar cell surface area	m^2
G	Solar irradiance	W/m^2
V	Voltage	V

Greek Symbols

θ	Angle	$^\circ$
η	Efficiency	%
h	Planck's constant (6.626×10^{-34})	J.s
λ	Wavelength	nm

Acronyms

AM	A ir M ass
ARC	A nti R eflection C oating
BIPV	B uilding I ntegrated P hoto- V oltaic
CVD	C hemical V apour D eposition
DAS	D ata A cquisition S ystem
DC	D own C onversion
DSC	D ifferential S canning C alorimetry
EDXA	E nergy D ispersive X -ray A nalysis
EQE	E xternal Q uantum E fficiency
ETC	E xperimental T echniques C entre
EVA	E thylene V inyl A cetate
IPA	I sopropyl A lcohol
IQE	I nternal Q uantum E fficiency
LPD	L iquid P hase D eposition
mc-Si	M ulti- C rystalline S ilicon
PL	P hoto- L uminescence
PLE	P hoto- L uminescence E xcitation
PV	P hoto- V oltaic
PACVD	P lasma A ssisted C hemical V apour D eposition
PECVD	P lasma E nhanced C hemical V apor D eposition
PMMA	P oly- M ethyl M eth- A crylate
PVA	P oly- V inyl A lcohol
R	R eflectance
RF	R adio F requency
SEM	S canning E lectron M icroscopy
TMS	T etra- M ethyl S ilane
UC	U P C onversion

Publications

Portions of the work detailed in this thesis have been presented in national and international scholarly publications, as follows:

Tahhan, A., Dehouche, Z., Anson, T., and Nelson, N. (2016). “Silicon oxide antireflection coating for crystalline silicon solar cell”. Submitted to Journal of Energy Report-Elsevier, Under Review.

Tahhan, A., Dehouche, Z., Fern, G. R., and Haverkamp, E. (2015). “Photovoltaic cells energy performance enhancement with downconverting photoluminescence phosphors”. International Journal of Energy Research, 39(12), pp. 1616-1622.

Tahhan, A., Dehouche, Z., Anson, T., and Fern, G. (2014). “Nanostructured silicon oxide film for enhanced crystalline solar cell”. In 40th IEEE Photovoltaic Specialist Conference (PVSC), pp. 1296-1298.

Breda, C., Dehouche, Z., **Tahhan, A.**, Anson, T. and Fern, G.R. (2014). “Titanium dioxide nanoparticles for enhanced monocrystalline solar cell”. In 40th IEEE Photovoltaic Specialist Conference (PVSC), pp. 1299-1304.

Tahhan, A., Dehouche, Z., and Fern, G. (2012). “Nanostructured materials for silicon solar cells grown by PECVD”. In World Congress on Sustainable Technologies (WCST), pp. 116-116.

Events and Presentations

WCST 2012: poster presentation titled “Nanostructured materials for silicon solar cells grown by PECVD,” at the World Congress on Sustainable Technologies Conference, London, UK.

ResCon 2013: oral presentation titled “The application of nanostructured materials for enhanced crystalline solar cell” at the 6th Annual Student Research Conference, Brunel University, UK.

Research Student Poster Conference 2013: poster presentation titled “Nanostructured silicon oxide film for enhanced crystalline solar cell” at Brunel Graduate School, Brunel University, UK.

NANOENERGY 2014: oral presentation entitled “Phosphor coating for enhanced crystalline silicon solar PV cell” at the International Conference on Nanotechnology, Nanomaterials & Thin Films for Energy Application, University College London, UK.

PVSC 2014: poster presentation titled “Nanostructured silicon oxide film for enhanced crystalline solar cell” at the 40th IEEE Photovoltaic Specialist Conference, Denver, USA.

PVSC 2014: poster presentation titled “Titanium dioxide nanoparticles for enhanced monocrystalline solar cell” at the 40th IEEE Photovoltaic Specialist Conference, Denver, USA.

ResCon 2014: oral presentation titled “Nanostructured materials for enhanced photovoltaic solar cell” at the 7th Annual Student Research Conference, Brunel University, UK.

Chapter 1

Introduction

Energy is the most important issue associated with the growth of developing countries and to sustain the lifestyle in the developed countries. The availability and accessibility of sufficient amount of energy accelerate the development of nations. It is a well-established relationship that countries with more use of energy are in a more advanced state of development. Therefore, higher energy supply is needed for the growth of developing countries and to sustain the lifestyle in the developed countries.

The world energy requirements are ever growing due to the increase in global population and the techno-economic growth of the countries. Currently, the need for energy is fulfilled by the conventional energy sources (oil, gas and coal). However, the fossil fuel based energy sources are limited in quantity and also cause environmental pollution.

Fossil fuel is not a sustainable source of energy in the long term. It is estimated that 1.3 trillion barrels of proven oil reserve left in the worlds major fields, which at present rates of consumption will be sufficient to last for 40 years [1]. Fossil fuel is not uniformly available in the world where two-thirds of the worlds remaining reserves are in the Middle East. According to Solanki [2], countries with insufficient resources will always feel insecure concerning their supply and will always be dependent on other

nations. This dependency could result in conflict and possibly war. The other insecurity comes from pricing these fuels is not stable. The world witnessed oil shocks due to war and instability in the region of Middle East which resulted in an increase in the oil price. Also, the rise in oil prices could be as a consequence that oil producing countries are not able to increase their production to meet the increasing demands of fuels [3]. The undisclosed price of using fossil fuels comes from its negative impact on the environment including, global warming, air quality deterioration, thermal pollution, oil spills and acid rain. This hidden price of using fossil fuels carries a significant threat to environment and existence of humankind.

The increase of global awareness on the impact of the use of conventional energy sources on the environmental, political and economic aspects of the society is a great drive for the search for a new source of energy. A greater global desire to gain independence from the use of fossil fuel and to replace it with the utilisation of the sustainable energy sources for power generation was shown through governmental plans.

Renewable energies such as wind, solar, geothermal, hydroelectric, and biomass have provided a new strategy for energy generation by using free available and sustainable natural resources without harm to the environment. In many nations around the world, there is an increasing number of policies, roadmaps, and studies which all share the vision of reducing CO₂ emission and obtaining the majority of its energy from renewables. In 2007, the European Union defined a target of 20% renewable energy for the year 2020 and reducing the EUs greenhouse gas emissions by 20% [4].

Among various solar power technologies of sustainable energy sources, it is believed that solar energy including photovoltaic is capable of generating as much as 50% of the world energy demands by 2050 [5]. Photovoltaic has received considerable attention for the clean energy resource to solve the environmental problem on the worldwide scale. Its popularity for electricity generation comes from its noiseless

with zero carbon dioxide emission during its operation, scale flexibility and rather a simple operation and maintenance [6]. It has been fifty years since the introduction of photovoltaics into the consumer market. From its earliest application in space where the cost was never a factor on the large scale of energy production on earth where the main concern is the price per kilowatt-hour. Since the introduction of PV to its current status, PV has evolved along the way due to considerable research and effort. The primary objective of the research in solar cells is mainly focused on improving the cell efficiency and reducing the cost. Among the various available PV technologies in the market, the production of solar cells was and is still based mainly on crystalline silicon cells, often called first generation PV, which dominates the PV market. It holds about 90% of the photovoltaic world market [7].

The main challenge for commercial crystalline silicon is the cost of bulk material as well as their limited conversion efficiency. A considerable amount of research is undergoing to improve the conversion efficiency of silicon solar cells and their integration in building through the application of the thin films and materials in nanosized scale which has demonstrated a capability of these approaches for energy performance enhancement of crystalline silicon photovoltaic solar cells.

1.1 Motivation

The growth of global energy demands and the need for a sustainable and environmentally friendly source of energy is the drive for this study through the investigation of enhancing the performance of silicon solar photovoltaic cells.

The aim of this work is to improve the performance of the solar cells via the application of oxide coatings while utilising safer processing methods in comparison to the conventional ones. A variety of potential oxide materials for solar cells light-absorption performance enhancement are investigated. These films are silicon oxide,

titanium oxide, and rare earth ion-doped gadolinium oxysulfide phosphor.

1.2 Thesis Layout

This thesis consists of seven chapters in which the relevant details are explained comprehensively in the respective chapter. This section briefly highlights the content of each chapter where the organisation of the thesis is as follow:

Chapter 1: introduced the reader to the global energy status and its environmental, political and economic aspects of the society. Also, it showed the role of photovoltaic as a new strategy for energy generation.

Chapter 2: provides the relevant background regarding the photovoltaic solar cell operation and the parameters affecting its conversion efficiency. Moreover, it gives a perspective of the current development concepts for enhancing the performance of the crystalline silicon solar cell.

Chapter 3: presents the equipment and instruments used for solar cells characterisation at Brunel University. It describes the functions of particular devices, the experimental procedures and the approach in carrying out of these experiments.

Chapter 4: illustrates the experimental work and results on silicon oxide films for single and double anti-reflection layer for crystalline silicon solar cells.

Chapter 5: shows the work done on silicon solar cells coated with thin films of titanium oxide and a stack of titanium/silicon oxide.

Chapter 6: demonstrates the work carried out on photovoltaic cells energy performance enhancement with downconverting photoluminescence phosphor.

Chapter 7: provides a conclusion about the findings obtained from the experimental results and gives recommendations for further studies of this work.

Chapter 2

Background

Photovoltaic-based crystalline silicon solar cells are simply semiconductors that have the ability to absorb the sunlight and convert a portion of the energy of the absorbed incident light into electrical energy. Photovoltaic solar cells can be simply described as a semiconductor diode that separates and collects the photo-generated charge carriers, electron-hole pairs, and conduct current in a specific direction. This chapter describes concisely the relevant background for the fundamental principles of solar cells operation.

2.1 Solar Irradiation

The operation of the crystalline photovoltaic solar cell is based on the generation of the charge carriers due partial absorption of sunlight by its semiconductor material. Sunlight is an electromagnetic radiation which can be viewed as being composed of particles called photons. These photons convey a specific amount of energy determined by the spectral properties of their source.

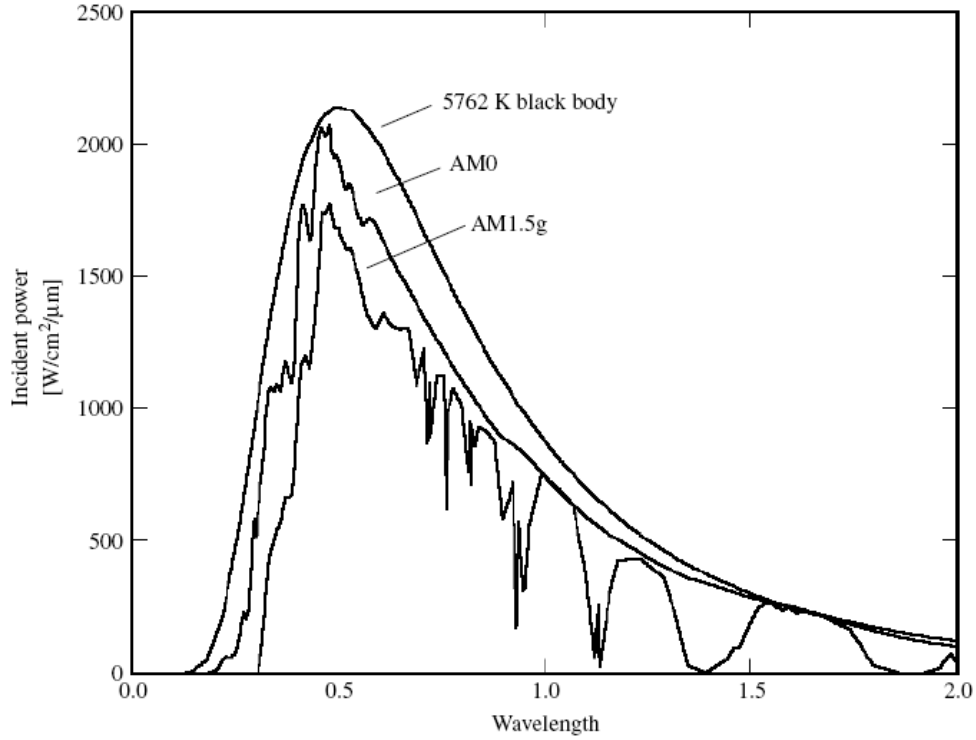


Figure 2.1: The radiation spectrum of a black body at 5762K compared with solar AM0 and AM1.5 global spectra [8].

The electromagnetic radiation can be characterized by wavelength (λ) and frequency (ν) or in terms of photons which characterised by energy ($h\nu$) expressed in electron volts where the energy carried by a single photon depends on its wavelength (E_λ). The relation between these quantities are shown in the following equations:

$$\nu = \frac{c}{\lambda} \quad (2.1)$$

$$E_\lambda = \frac{hc}{\lambda} \quad (2.2)$$

In Equations 2.1 and 2.2, c is the speed of light in vacuum (2.998×10^8 m/s), where h is Planck's constant (6.626×10^{-34} J.s).

The sun possesses many properties that could be discussed extensively. However, the most important parameters for photovoltaic solar cells studies are the irradiance, the amount power incidence on a surface per unit area, and the spectral characteris-

tics of the light [9]. Figure 2.1 shows the spectral distributions of various sources of the light. The irradiance value outside the Earth's atmosphere is called the solar constant, and it is equal to 1365 W/m^2 . However, once the irradiance enters the earth's atmosphere, it suffers from absorption losses due to the presence of molecules composing atmosphere such as ozone, oxygen, carbon dioxide and water vapour. Moreover, aerosol and dust induce absorption losses nearly over the entire spectral range which leads to a global reduction of the incident power [10].

Therefore, the radiation on the earth's surface reaching a particular place is variable. Also, other factors affect this variation including the daily and yearly variation due to the motion of the sun, local atmospheric conditions such as the sun. The mentioned conditions influence the spectral component of the sunlight, the direct and the diffused components. The direct component of the solar irradiation is part of the sunlight that reaches the earth's surface directly whereas the diffused component is generated due to scattering of the sunlight in the atmosphere. Also, albedo could be presented to the total solar spectrum which refers to the reflected part of the solar irradiation from the earth's surface. The total solar radiation, also called global radiation, is composed of these three components.

The standard solar spectrum is normally referred as AM1.5G where G stands for global sun and AM stands for Air Mass. It is determined by the angle of the incidence (θ), $\theta=0^\circ$ when the sun is directly overhead; AM is defined in the Equation 2.3:

$$AirMass(number) = \frac{L_S}{L_A} = \frac{1}{\cos \theta} \quad (2.3)$$

Where L_S is the effective solar radiation path length in the atmosphere, L_A is the thickness of the atmosphere and also: the overhead path length of the light, vertical positioning of the sun for the angle of the incidence (θ) relative to the normal of the earth's surface and irradiation flux of 1000 W/m^2 ($\equiv 100 \text{ mW/cm}^2$ or 1 sun).

The AM factor refers to the information about absorption losses and changes to the spectrum due to absorption in the atmosphere before reaching the solar converter. Therefore, it varies with the latitude and the time of the day and the year.

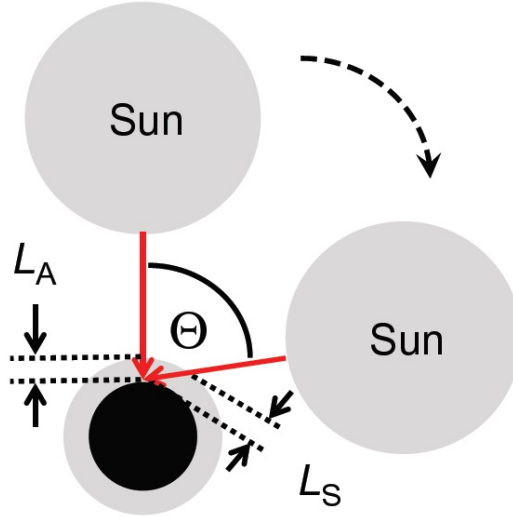


Figure 2.2: A sketch showing definitions for AM factor [11].

The definition of AM is given in Figure 2.2 and Equation 2.3. The most commonly used AM factor values are:

- AM0: defines the extra-terrestrial spectrum at the boundary of the atmosphere which is the irradiance of 5800 K black body with intensity about 28% higher than AM1.5G.
- AM1: measured at ground level for the sun at Zenith.
- AM1.5: correspond to an angle 48.2° . It is the standard for evaluation of the performance of solar panels. For solar concentrators, direct irradiation is used and the corresponding spectrum is AM1.5D, which is 10% less intense in comparison to AM1.5G.

Weather station can provide measurements of the solar irradiation, and historical data can be recorded. Solar radiation database is available to access by the US Department of Energy from EnergyPlus website [12]. Also, it can be obtained

through Photovoltaic Geographical Information System (PVGIS) Website by Institute for Energy and Transport (IET) by the European Commission, which provides with a map-based inventory of solar energy resource [13]. Figure 2.3 illustrates an example of the average hourly radiation data for each month of the year for the location of Gatwick, London obtained from EnergyPlus website.

Irradiance data is an essential component of the weather files for the assessment of the electricity generation from photovoltaic systems. Despite the fact, that many weather/meteorological stations measure the received irradiation, solar radiation can be estimated with the knowledge of the local climate for a particular location using solar radiation models. These models vary in complexity and summaries of these approaches for the estimation for radiation data is given in [14, 15].

	Jan	Feb	Mar	Apr	May	Jun	Jul	Aug	Sep	Oct	Nov	Dec	hour	Avg year	
0:01-1:00	0	0	0	0	0	0	0	0	0	0	0	0	0	1	0
1:01-2:00	0	0	0	0	0	0	0	0	0	0	0	0	0	2	0
2:01-3:00	0	0	0	0	0	0	0	0	0	0	0	0	0	3	0
3:01-4:00	0	0	0	0	0	0	0	0	0	0	0	0	0	4	0
4:01-5:00	0	0	0	0	8	13	9	1	0	0	0	0	0	5	3
5:01-6:00	0	0	0	13	60	64	56	20	2	0	0	0	0	6	18
6:01-7:00	0	0	9	72	155	153	148	99	38	7	0	0	0	7	57
7:01-8:00	0	6	60	167	276	253	249	198	128	57	9	0	0	8	117
8:01-9:00	17	53	135	279	381	352	366	317	221	137	57	13	9	9	194
9:01-10:00	65	121	225	349	460	462	440	405	312	212	119	54	10	10	269
10:01-11:00	108	164	263	411	516	539	523	479	383	272	167	89	11	11	326
11:01-12:00	140	195	289	453	564	594	580	518	412	290	173	116	12	12	360
12:01-13:00	142	204	331	464	565	560	536	518	400	269	180	124	13	13	363
13:01-14:00	128	187	296	467	537	510	567	549	365	218	148	94	14	14	339
14:01-15:00	78	151	229	381	480	471	503	469	318	165	87	48	15	15	282
15:01-16:00	31	87	167	296	379	378	400	373	234	93	28	11	16	16	206
16:01-17:00	2	25	89	189	286	282	290	251	125	26	1	0	17	17	131
17:01-18:00	0	1	22	84	176	180	192	120	34	1	0	0	18	18	68
18:01-19:00	0	0	1	14	62	80	84	31	2	0	0	0	19	19	23
19:01-20:00	0	0	0	0	7	17	15	2	0	0	0	0	20	20	3
20:01-21:00	0	0	0	0	0	0	0	0	0	0	0	0	21	21	0
21:01-22:00	0	0	0	0	0	0	0	0	0	0	0	0	22	22	0
22:01-23:00	0	0	0	0	0	0	0	0	0	0	0	0	23	23	0
23:01-24:00	0	0	0	0	0	0	0	0	0	0	0	0	24	24	0

Figure 2.3: Average hourly radiation data for each month of the year in W/m^2 for Gatwick, London [16].

2.2 Type of Solar Cells

Photovoltaic solar cells are typically divided into three categories called generations, depending on the basic material used [17]:

- First Generation: Crystalline silicon.
- Second Generation: Thin film technologies.
- Third Generation: includes new concept devices.

Figure 2.4 shows a tree of PV technologies while the recorded efficiencies of solar cells and commercial PV modules are presented in Table 2.1 and the time-line of the solar cell energy conversion efficiencies records is shown in Figure 2.8.

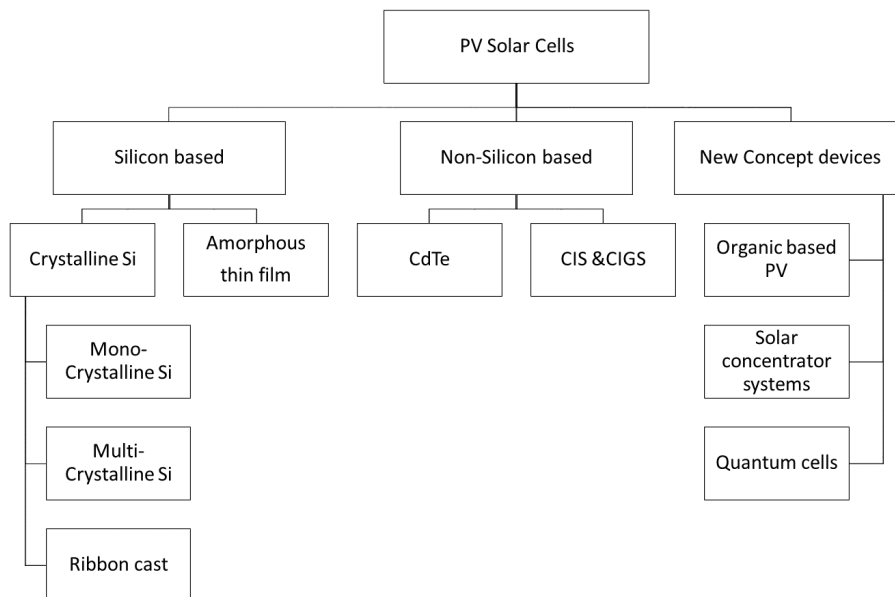


Figure 2.4: PV technologies tree. Redrawn from Jelle et al.[17].

2.2.1 First Generation PV

The first generation includes solar cells that are relatively expensive to produce. It includes mono-crystalline, multi-crystalline and ribbon silicon solar cells.

2.2.1.1 Monocrystalline Solar Cells

Monocrystalline silicon solar cells are produced from a single crystal silicon structure high purity silicon ingot are extracted from a cast then cut into thin wafers and then processed into PV cells. The corners of the cells are cropped because the silicon wafer is cut from cylindrical ingots which is grown by the Czochralski process. The estimated life span of these solar cells is around 25-30 years [18]. Mono-crystalline silicon solar cells are expensive but more efficient than other type of solar cells. The highest recorded efficiency of mono-crystalline solar cells is 25.6% by Panasonic[19].

2.2.1.2 Multicrystalline Solar Cells

Production of multi-crystalline silicon solar cells is more economical and efficient in comparison to mono-crystalline solar cells. However, multi-crystalline solar cell have a lower efficiency than a mono-crystalline solar cell. In multi-crystalline silicon, the silicon is cast in blocks. When it hardens, it results in crystal structures of different sizes and exhibits defects which reduces the degree of efficiency of the solar cell. The highest recorded efficiency of the multi-crystalline solar cell is 21.3% by Trina Solar [20].

2.2.1.3 Ribbon Solar Cells

Ribbon silicon cells are also called string ribbon cells. It is a type of multi-crystalline silicon which is produced by extracting a flat thin films from molten silicon and results in a polycrystalline structure. This technique provides low-cost Si due to the high utilisation of the Si feedstock. Therefore, These cells are cheaper to make than multi-Si, due to a significant reduction in silicon waste but they are also less efficient.

2.2.2 Second Generation PV

The second generation covers types of solar cells with lower efficiency than the first generation but is much cheaper to manufacture. The second generation photovoltaic are often called thin-film solar cells because when compared to crystalline silicon-based cells they are made of layers of semiconductor materials that is only a few micrometres thick.

2.2.2.1 Amorphous Silicon Cells

The main difference between crystalline silicon and amorphous silicon (a-Si) that in the later, the silicon atoms are located at various distances from each other unlike crystalline and the angles between the Si-Si bonds do not have a unique value. Amorphous silicon solar cells are incorporated with hydrogen which increases the photo-conductivity significantly while pure silicon exhibit poor optical and electrical properties [21]. It is important to mention that when the amorphous silicon solar cell

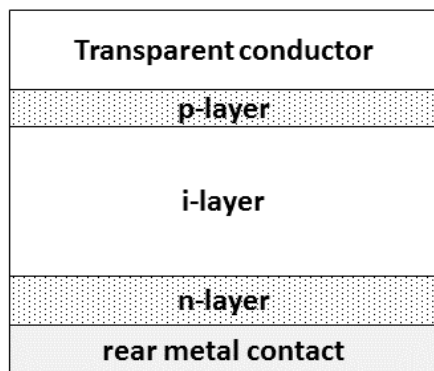


Figure 2.5: A schematic of amorphous silicon p-i-n solar cell structure.

is made of a p-n junction, the p and n material showed poor transport properties of electrons and the p-n junction amorphous silicon solar cell had low efficiency. The p-i-n junction cell as shown in Figure 2.5 was developed to enhance the poor transport properties. Unlike crystalline silicon cells which feature a grid contacts on the top surface, the p-i-n amorphous silicon solar has a transparent conducting contact deposited

as a thin film of Tin oxide of at the surface of the p+ layer and a metal contact is located at the rear of the cell [2]. The highest recorded efficiency of amorphous silicon solar cells is 13.6% by AIST research centre for photovoltaic [20].

2.2.2.2 Copper Indium Selenide Cells

Overall, elements from the group I, III, VI in the periodic table are of great potential for applications in photovoltaic and in particular for thin film solar cell application. Copper Indium Gallium Selenide (CIGS) cells are made with a thin layer of copper indium gallium diselenide Cu(In, Ga)Se_2 . CIGS solar cells are manufactured by the deposition of a thin layer of the following materials: copper, indium, gallium and selenide on a substrate of glass or plastic with electrodes collect the current on the front and back. The highest recorded efficiency of CIGS cells is 22.3% by Solar Frontier with similar durability as silicon solar cells. However, manufacturing costs CIGS solar cells are high when compared with amorphous silicon solar cells.

2.2.2.3 Cadmium Telluride Cells

Cadmium telluride (CdTe) solar cells are often produced using manufacturing processes such as screen-printing, galvanic disposition or spray pyrolysis can be used to produce the CdTe cells. The structure of CdTe solar cells consists of a glass substrate with a transparent conduction layer and an indium tin oxide (ITO) coated front contact cover which is sandwiched with Cadmium Sulphide (CdS) to form a p-n junction photovoltaic solar cell. Typically, CdTe cells use an n-i-p structure. However, Large-scale of CdTe modules can be achieved through a vapour deposition process. First Solar announced achieving a record 22.1% conversion efficiency in their CdTe cells [19].

2.2.3 Third Generation PV

The term third generation is used to describe solar cells that are very efficient. Most technologies in this generation are not yet commercial, but there is an extensive research is being carried out in this area.

2.2.3.1 Dye Sensitised and Organic cells

The primary material of a Dye Sensitised Solar Cells (DSSCs) is the semiconductor titanium dioxide. In comparison to p-n junction cells, dye-sensitised cells have a different mode of function. Light absorption occurs at a very specific location in the dye molecules which covers a porous layer of titania nanoparticles [22]. This is similar to the way plants use chlorophyll to capture energy from sunlight through photosynthesis. Most of the materials for DSSCs are non-toxic and inexpensive to produce. DSSCs are attractive as a replacement for existing technologies in "low-density" applications like rooftop solar collectors, where the light weight of the glass-less collector is a significant advantage.

The main disadvantage to the design of DSSCs is the use of the liquid electrolyte, which results in temperature stability issues. At low temperatures, the electrolyte can freeze, terminating the generation of power while at higher temperatures can cause the liquid to expand, making sealing the panels a serious problem. Dye-sensitised cells are tolerant to poor incidence angles and shading with solar to electrical conversion efficiency increasing at higher temperatures in contrast to crystalline silicon cells. The highest reported DSSC efficiency achieved to date was 11.9% by Sharp [20]. Due to the compatibility of solution-processible organic semiconductors with printing-based production and low-cost, flexible substrates, organic cells offer a substantial potential for photovoltaic systems in the future. Materials of particular interests are molecular, and polymeric semiconductors and fullerene (C60) and its derivatives are attractive

materials for the development of organic cells [23]. Recently, significant progress has been made in enhancing the performance of organic solar cells. However, they still do not achieve the requirements of practical applications. The highest achieved efficiency reported for organic cells to date by Hong Kong UST who achieved an efficiency of 11.5% [20].

2.2.3.2 Perovskite Solar Cell

Perovskite solar cells have attracted a noticeable attention in a short period. The conversion efficiency of perovskite solar cells improved from under 4% in 2010 to 22% in 2016. Perovskite solar cells features a high absorption coefficient with a thickness of around 500 nm to absorb solar energy, but perovskite solar cell degrade quickly in a moist environment [24]. The perovskite structure can be defined as any compound that has the generic form ABX_3 and the same crystallographic structure as perovskite mineral. Perovskite can be illustrated as a large positively charged atomic or molecular cation of type A in the centre of a cube. Also, positively charged cations have occupied on the corners of the cube represented as atoms B where a smaller atom X occupies the faces of the cube with a negative charge. The most efficient perovskite

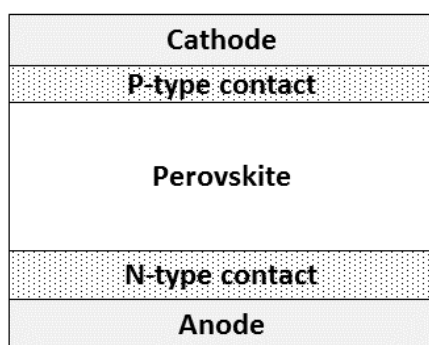


Figure 2.6: A schematic of the structure of Pervoskite solar cell.

solar cells so far have been produced with the following combination of materials in the usual perovskite form ABX_3 : A = an organic cation - methylammonium, B = a big inorganic cation - typically lead, and X_3 = a slightly smaller anion typically chloride

or iodide. Figure 2.6 shows a schematic of Perovskite solar cell where a perovskite solar cells can be integrated very easily into a standard organic PV or other thin film architecture.

2.2.3.3 The Multi-Junction III-V Solar Cells

III-V semiconductors such as Gallium Arsenide (GaAs), gallium aluminium arsenide (GaAlAs), Indium antimonide (InSb) and Indium phosphide (InP) have received growing attention as photovoltaic materials. The III-V cells have a solar-electrical conversion efficiency higher than that of Si cells. The highest recorded multi-junctions solar cells under the non-concentrate light are 38.8% by Boeing Spectrolab. Although multi-junction III-V solar cells have high conversion efficiency, they have a disadvantage of using rare materials and have high production costs.

The multi-junction III-V solar cells is an ideal device for achieving the best efficient use of the solar spectrum. The device is constituted by stacking some pn junction, each with a bandgap, with the highest gap being at the top of the illuminated device and the lowest at the bottom. This design allows every photon with energy (E_g) will be absorbed and converted by an appropriate semiconductor without any thermalisation loss. Herry et al. indicated that a predicted theoretical efficiency of 72% could be achieved for Multi-junction (MJ) III-V solar cells with 32 bandgaps [25]. Figure Schematic of 3,4,5,6 junction solar cells with their maximum theoretical efficiency [26, 27].

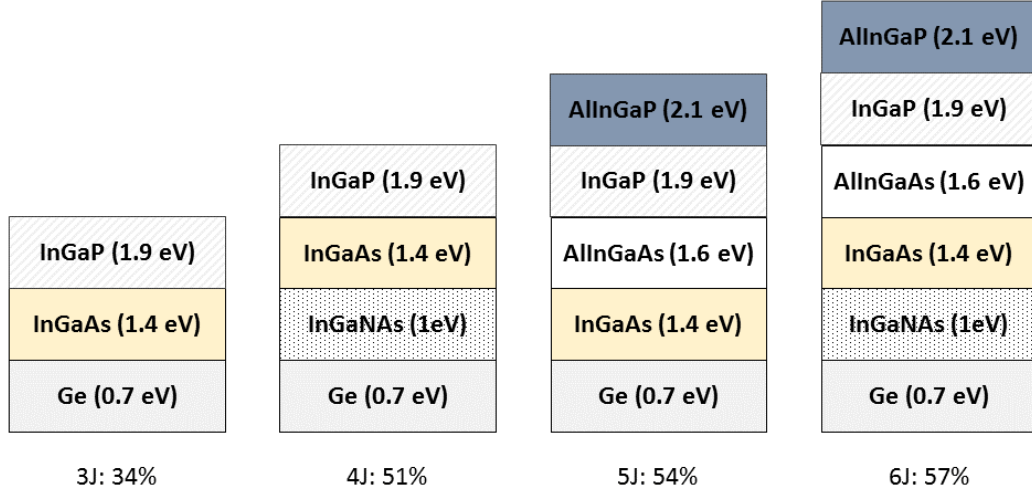


Figure 2.7: A schematic structure of 3,4,5,6 junctions solar cell with their maximum theoretical efficiency.

Table 2.1: Confirmed efficiencies of solar cells and commercial PV modules [19].

Generation	Technology	Efficiency (%)	
		Cell	Module
1st	Mono-crystalline Silicon	25.6	22.9
	Multicrystalline Silicon	20.4	18.5
2nd	CIGS	20.5	15.7
	CdTe	19.6	17.5
	Amorphous Silicon	10.1	11.6
	Thin Film Polycrystalline Silicon	11.0	8.2
3rd	Multijunction	37.9	NA
	Organic	10.7	NA
	Dye Sensitised	11.9	NA

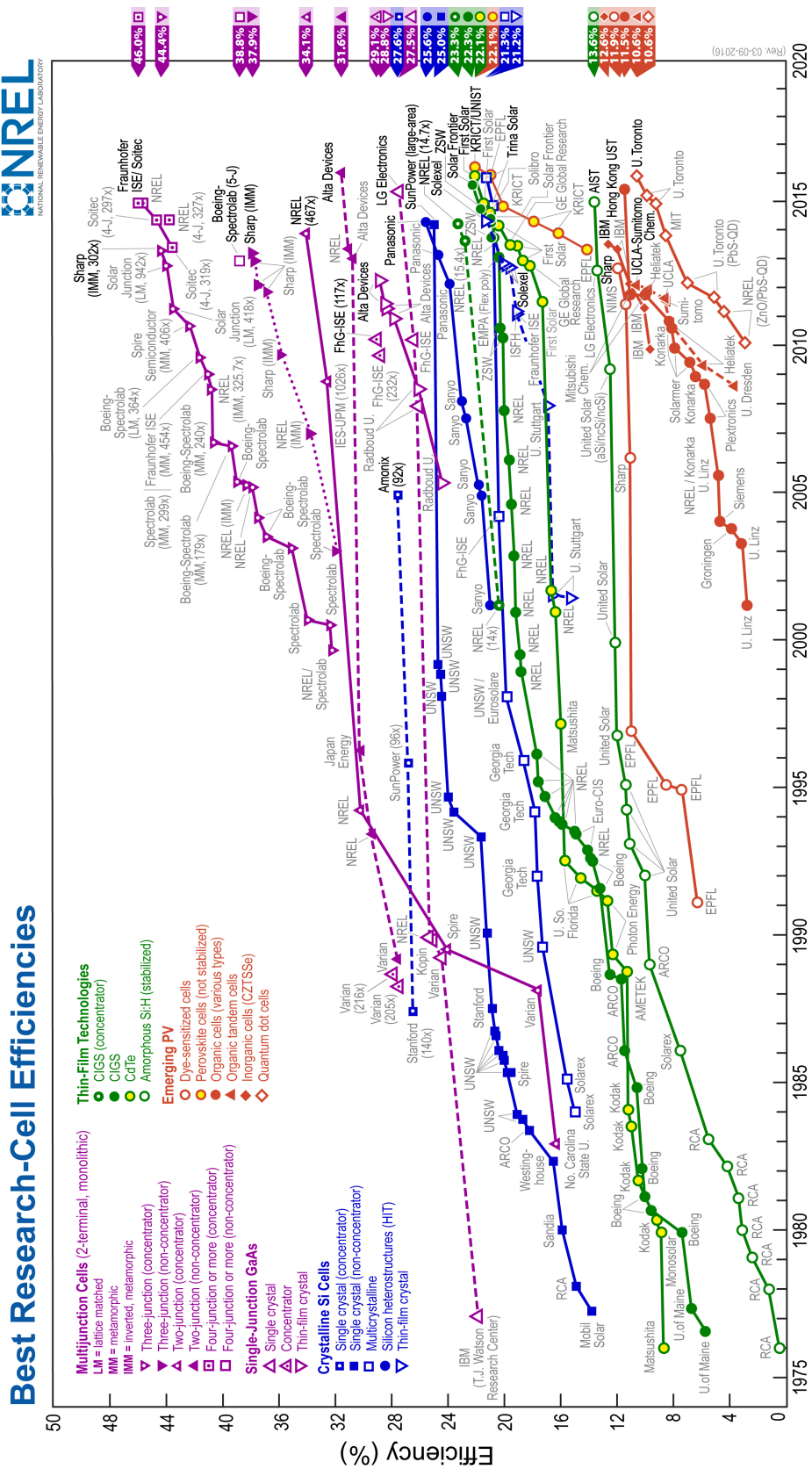


Figure 2.8: Timeline of solar cell energy conversion efficiencies records [20].

2.3 Principles of Solar Cells Operation

The concept of energy conversion of the p-n junction solar cells can be summarised as follow [28, 2, 29]:

A photovoltaic solar cell is an electronic device that can convert sunlight into electricity directly. Exposing the solar cell into light produces both current and voltage which generate electrical power. This process, called photovoltaic effect, requires a material where its absorption of the light raises an electron to a higher energy state and then the movement of this higher energy electron from the solar cell into an external load where it dissipates its energy in the external circuit and returns to the solar cell. In general, the majority of the photovoltaic devices need an internal electric field that leads to the separation of the photo-generated charge carriers (electrons and holes) where this separation occurs at the p-n junction of the PV cell.

Figure 2.9 represents the common design pattern of the single p-n junction crystalline solar cells (mono or multi-crystalline silicon wafer), with a crystalline silicon wafer 200-300 micron thick [30]. The electrical contacts in the cell are the front grid and back contact. The front metallic grid pattern is designed in a way to maximise the collection of photo-generated current by reducing the coverage of the front surface of the cell by widely spacing the grid to allow the light to enter the cell but not extent to raise a struggle for the fingers to collect the current produced by the cell. On the other side of the cell, these restrictions do not apply to the rear metallic contact layer which serves only as a metallic contact. The silicon wafer reflects 30% of the incident light on the cell [31]. Therefore, an anti-reflection coating is applied to the front surface of the solar cell to minimise the reflection losses from the top surface of the wafer and increase the amount of light absorbed by the cell which leads to improving the conversion efficiency of the silicon solar cell.

Silicon nitride is commonly used as an anti-reflection layer for commercial silicon

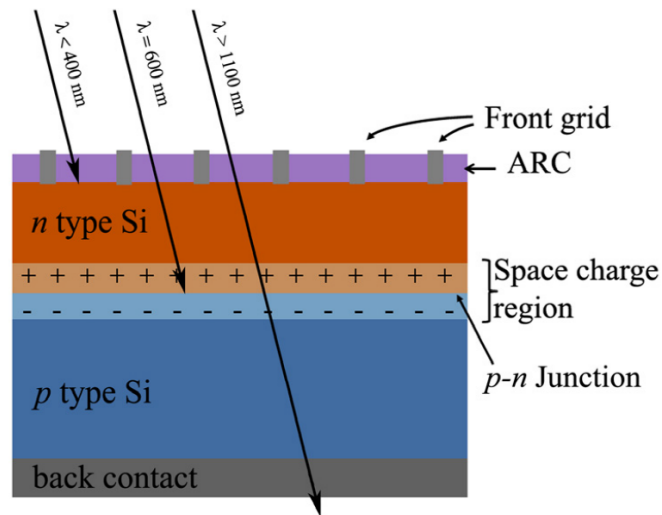


Figure 2.9: Schematic of the architecture of a p-n junction Si solar cell [30].

solar cells due to its excellent passivation properties that prevent carrier recombination at the surface of the solar cell. Silicon nitride is deposited on the solar cell as a thin film with a thickness of about 80 nm using PECVD [30].

2.4 IV Characteristic of C-Si Solar Cell

Solar cells are semiconductors that can absorb the electromagnetic waves and generate charge carriers. An ideal solar cell can be represented as a diode connected in parallel with a light controlled current source as shown in Figure 2.10 [32, 33]:

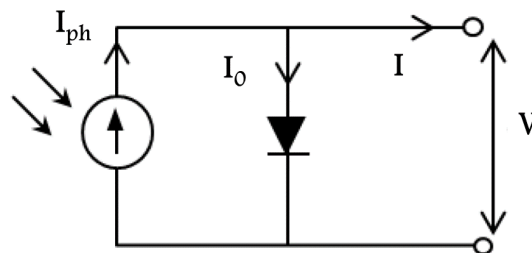


Figure 2.10: The equivalent circuit model of an ideal solar cell.

The performance of crystalline silicon solar cells is evaluated by current-voltage (I-V) measurement. Based on the standard diode equation, I-V characteristics of a

single junction solar cell under illumination can be written as the linear superposition of the I-V curve of the solar cell diode in the dark with the light-generated current [2]:

$$I = I_{ph} - I_o \left\{ \exp \left(\frac{qV}{nkT} \right) - 1 \right\} \quad (2.4)$$

Where I_o is the reverse saturation current, q is the elementary charge, T the absolute temperature and n the ideality factor ($n=1$ for ideal p-n junction where the current is dominated by diffusion mechanism whereas $n=2$ when the current is dominated by the recombination phenomena in the space charge region), k the Boltzmann constant, I_{ph} is the photo-generated current. When the PV cell is not illuminated (dark condition), there is no contributions from the photo-generated current and the resulting diode characteristic curve is shown in Figure 2.11. By illuminating the PV cell, reported in the same figure, the dark curve is shifted down into the fourth quadrant by the current I_{ph} where the power can be extracted from the cell.

The output of the solar cell is characterized using four main parameters:

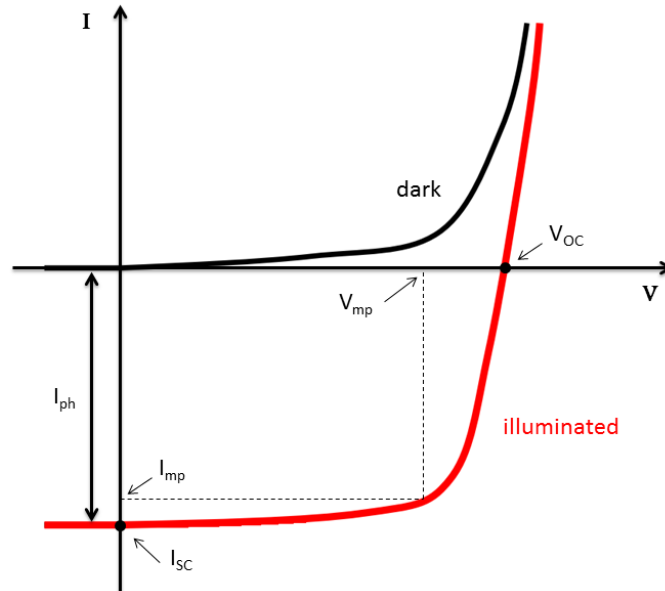


Figure 2.11: I-V characteristics curves of p-n junction solar cell under dark and light illumination conditions [2].

- Short circuit current (I_{sc}): is current that can be reached through the solar cell under illumination when the voltage across the solar cell is zero. (i.e., when the PV device is short-circuited. In other words, when the terminals of the PV device are connected with each other). Ideally, this parameter is equal to the light-generated current under illumination (I_{ph}).
- Open-circuit voltage (V_{oc}): is the maximum voltage available from a solar cell established under illumination, and this occurs when the current through the PV device is zero, (i.e., when the circuit is not closed). V_{oc} can be calculated from Equation 2.4 with the condition $I=0$:

$$V_{oc} = \frac{nkT}{q} \ln \left(\frac{I_{ph}}{I_o} + 1 \right) \quad (2.5)$$

- Fill Factor (FF): is a measure of the squareness of the solar cell characteristics and it is defined as:

$$FF = \frac{V_{mp}I_{mp}}{V_{oc}I_{sc}} \quad (2.6)$$

Where (I_{mp} , V_{mp}) is a particular operating point, corresponding to the maximum power output. Graphically, FF corresponds to the area of the dashed rectangle in Figure 2.11. The higher the FF, the higher the power that can be extracted from the cell.

- Energy conversion efficiency is defined as:

$$\eta = \frac{P_{mp}}{GA} = \frac{V_{oc}I_{sc}FF}{GA} \quad (2.7)$$

Where G is the incident solar radiation and A is the effective solar cell area which represents the illuminated area of the solar cell. The efficiency of the device depends on the parameters I_{sc} , V_{oc} and FF where the higher values of these parameters, the higher efficiency of the PV device will be.

The energy conversion efficiency of the photovoltaic solar cell depends on several different external factors. Among these factors are:

- The conversion efficiency relies on the wavelength of the light. Therefore, the efficiency of the photovoltaic cell will change with the variations in the spectrum of the sunlight [34, 35].
- The conversion efficiency depends on the temperature. The photovoltaic module will depend on the temperature of the surrounding air and also on the light intensity and the local wind speed [36, 37].
- The conversion efficiency of the module depends on the reflectivity of the solar cell, encapsulation material, and the glass which accommodates the cells. The effects depend in particular on the angle on which the incoming light hits the module's surface [38, 39].

By taking in account all of the mentioned effects above, the operational conversion efficiency of the photovoltaic modules results in a deviation from the conversion efficiency of the solar cell under Standard Test Condition (STC). STC defines the measurements conditions at temperature of 25 °C, 1000 W/m² irradiance and AM1.5 Air Mass global spectrum [40].

2.4.1 Practical Solar Cells Devices

In practice, I-V characteristics of the solar cell differ from the ideal one. Figure 2.12 shows the equivalent circuit model of a practical solar cell where a two diode model is used where the second diode has a value of 2 of the ideality factor.

The circuit model also includes a series (R_s) and parallel or shunt (R_{sh}) resistances

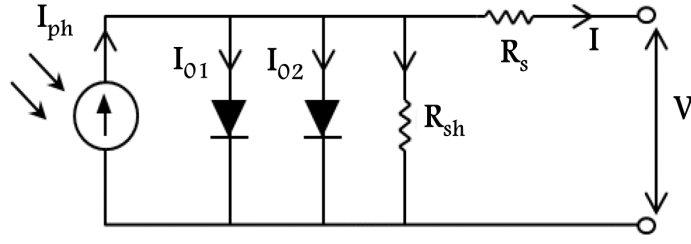


Figure 2.12: The equivalent circuit model of a practical solar cell.

resulting in characteristics in the following form:

$$I = I_{ph} - I_{01} \left\{ \exp \left(\frac{V + IR_s}{nk_B T} \right) - 1 \right\} - I_{02} \left\{ \exp \left(\frac{V + IR_s}{nk_B T} \right) - 1 \right\} - \frac{V + IR_s}{R_{sh}} \quad (2.8)$$

Actual devices are less efficient than ideal solar cells. Recombination of photo-generated electron-hole pairs in the bulk and at surfaces are responsible for losses, thus reducing the FF too. These mechanisms are taken into account in Equation 2.4 by the introduction of the ideality factor n . Moreover, the resistance of the semiconductor materials and metal contacts give rise to a parasitic series resistance associated with the solar cell. Also, leakage across p-n junction, due to the presence of crystal defects, impurities, precipitates, create current shunting paths, which can be described as a shunt resistance.

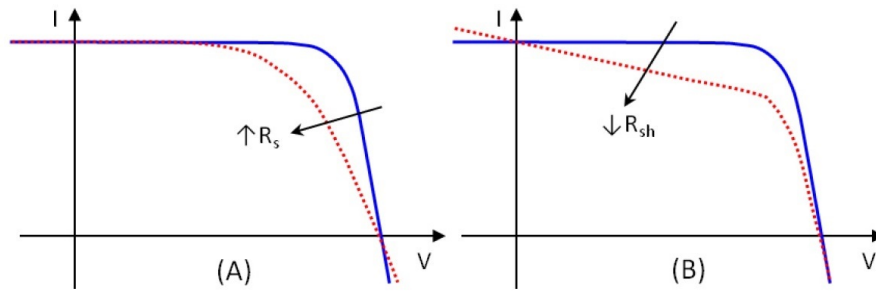


Figure 2.13: Effects of parasitic resistances: (A) series and (B) on the I-V curve.

The effects of the parasitics resistances on the I-V curve is shown in Figure 2.13. The main impact of the parasitic resistances is to reduce the fill factor and thus the conversion efficiency.

As the series resistance increases, the voltage drop between the output terminal becomes greater for the same current. As a result, the current controlled part of the IV curve starts to sag toward the origin. High values of series resistance may also reduce the short-circuit current. Therefore, the series resistance is of great concern at higher light intensities, especially in solar concentrator systems.

On the other hand, the effects of shunt resistance are severe at low light levels since the shunting pathway bleeds current away reducing output current, the loss of this current due to shunt resistance would result in reducing the solar cell efficiency. As the shunt resistance decreases, this causes the voltage controlled portion of the I-V curve to be shifted down toward the origin. At low resistances, open circuit voltage is severely reduced. Low shunt resistances refer to a leaky device with poor rectifying characteristics.

Under illumination, the I-V curve of a PV device is a strong function of temperature that must be considered in measuring the electrical characteristics of the solar cell. The short circuit current has the smallest temperature dependence which is caused by the semiconductor bandgap shifting to longer wavelengths with higher temperatures [41]. On the other hand, the open circuit voltage circuit and maximum power degrade rapidly with increasing temperature. Due to these strong dependencies, a fixed temperature of 25 °C under standard test conditions [21].

2.4.2 Design of Antireflection Coatings

This section presents the theory of designing an antireflection coating for a Single Layer Antireflection (SLAR) and Double Layer Antireflection (DLAR).

SLAR coating is the minimum requirement for the production of silicon solar cells. The semiconducting materials such as silicon absorb light and exhibit high refractive indices. For instance, silicon has a refractive index of $n_{Si} = 3.939$ at 600

nm.8 which is much greater than air and glass. The refractive index of air and glass at 600 nm are $n_{air}= 1.0$ and $n_0=1.52$ respectively [42]. The reflectance of incident light at such an interface is given by Equation 2.9:

$$R = \left(\frac{n_{Si} - n_o}{n_{Si} + n_o} \right)^2 \quad (2.9)$$

This means that 35.4% or 19.6% of the light is reflected off an air:silicon or glass:silicon interface in the first bounce, respectively. When the optimum thickness antireflection coating is introduced between the silicon and ambient medium, the minimum reflectance is given by Equation 2.10:

$$R = \left(\frac{n_{AR} - n_o n_{Si}}{n_{AR} + n_o n_{Si}} \right)^2 \quad (2.10)$$

where n_{AR} is the refractive index of the coating. Zero reflectance at one wavelength can be achieved when the value n_{AR} is calculated using Equation 2.11:

$$n_{AR} = \sqrt{n_o n_{Si}} \quad (2.11)$$

and the film thickness d_{AR} must meet the quarterwave optical thickness requirement where λ is the wavelength of zero or minimum reflectivity where the film thickness d_{AR} is given by Equation 2.12:

$$d_{AR} = \frac{\lambda_o}{n_{AR}} \quad (2.12)$$

The previous equations show that an antireflection coating for a silicon solar cell in air should have a refractive index of 1.985 and a thickness of 75.6 nm, while a glass encapsulated cell requires an AR coating with $n_{AR}= 2.447$ and $d_{AR}= 61.3$ nm.

In the design of SLAR coating, zero reflectance can be achieved at one wavelength while a DLAR coating can offer a further reduction in reflectance. In DLAR, the refractive indices are stacked as follows $n_{Si} > n_{AR2} > n_{AR1} > n_o$, where n_{AR2} and n_{AR1}

represent antireflection coatings with high and low refractive indices, respectively. For layers with equal optical thickness, such that $n_{AR2} d_{AR2} = n_{AR1} d_{AR1} = \lambda_0/4$, the reflectance at λ_0 becomes:

$$R = \left(\frac{n_{AR1}^2 n_{Si} - n_{AR2}^2 n_o}{n_{AR1}^2 n_{Si} + n_{AR2}^2 n_o} \right)^2 \quad (2.13)$$

The reflectance (R) will be either a maximum or minimum at λ_0 depending on the relationship between the refractive indices. From Equation 2.13, it can be seen that if $n_{AR1}^2 n_{Si} = n_{AR2}^2 n_o$, zero reflectance at λ_0 can be achieved.

However, if $n_{AR1} n_{AR2} = n_o n_{Si}$ a maximum of R will occur at λ_0 and double zero reflectance will be achieved at two wavelengths either side of λ_0 . In case of two quarter-wavelength coatings, the optimal refractive indices of each layer in a DLAR stack can be obtained by Equations 2.14 and 2.15[43]:

$$n_{AR1}^3 = n_o^3 n_{Si} \quad (2.14)$$

$$n_{AR1}^3 = n_o^3 n_{Si} \quad (2.15)$$

2.4.3 Quantum Efficiency

The quantum efficiency of the solar cell represents the percentage of photons that are converted to electrical current when the solar cell is operated under short circuit current conditions. Quantum efficiency of solar cell is represented by External Quantum Efficiency (EQE) or Internal Quantum Efficiency (IQE).

EQE gives information about the fraction of incident photons that are being converted to electrons in the device. Moreover, EQE can be seen as an indicator of the severity of surface reflection as it consist of the effect of optical losses such as transmission through the solar cell and reflection of light away from the cell.

IQE gives information about the fraction of absorbed photons that are being converted to electrons in the device. It discounts the light that is not transmitted through or reflected away from the cell.

$$IQE = \frac{EQE}{1 - R - T} \quad (2.16)$$

Where R and T are the reflection and transmission coefficient respectively. IQE is a direct measurement of recombination and refers to solar cells ability to utilise photons. In general, IQE is higher than EQE for a given device because the factor 1-R is always less than 1.

2.5 Energy Losses of p-n Junction Solar Cell

2.5.1 Energy Losses of Ideal Solar Cell

The photons of the radiation incident on the surface of a semiconductor can be either reflected from the top surface, absorbed or transmitted through the semiconductor material. Absorption of the photon by the semiconductor material will raise

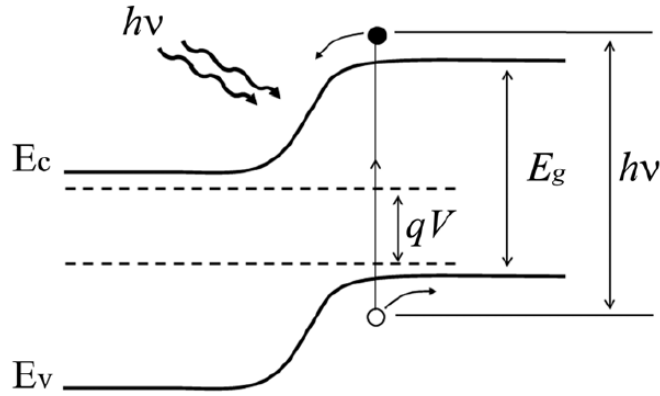


Figure 2.14: Energy band diagram of p-n junction under illumination.

an electron from the valence band (E_v) to the conductive (E_c) band as illustrated in Figure 2.14. However, reflection and transmission of the semiconductor are considered as a loss mechanism in photovoltaic because these mechanisms do not contribute to the generation of charge carriers.

The fundamental spectral losses in single junction silicon-based photovoltaic solar cells can be large as results of the mismatch between the incident sunlight spectrum and the spectral absorption properties of the semiconductor material.

It can be determined if a photon is absorbed or transmitted through the photovoltaic material by the energy of the photon. Photons striking the photovoltaic semiconductor material can be classified into three groups based on their energy compared to that of the semiconductor energy band gap:

1. $E_{ph} < E_g$: photons with an energy E_{ph} smaller than the band gap E_g are not ab-

sorbed by the semiconductor even if the thickness is sufficiently thick. Therefore, the inability of the semiconductor to absorb photons below bandgap energy will not result in the generation of charge carriers. This energy loss is indicated by A in Figure 2.15 which shows the solar energy spectrum assuming the black body radiation at 6000K. This loss is referred to as transmission loss which accounts for about 23% for single junction silicon solar cell.

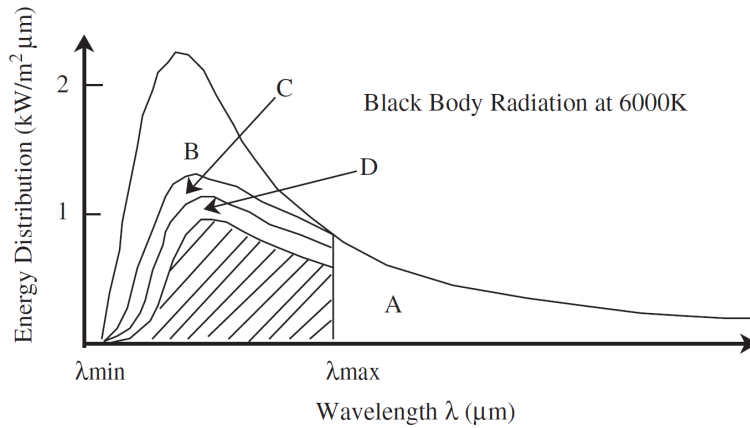


Figure 2.15: Spectral distribution of sunlight and energy losses [29]. A represents the energy that is not absorbed by semiconductor, B represents the excess energy loss, C to the voltage factor loss and D to the fill factor loss.

2. $E_{ph}=E_g$: photons with an energy E_{ph} close to the semiconductor bandgap E_g can create an electron-hole pair.
3. $E_{ph}>E_g$: photons with energy E_{ph} larger than the semiconductor bandgap energy E_g are absorbed, but the excess energy is lost as a form of heat. The excess energy $E_{ph}-E_g$ contributes to the lattice vibration, the loss of energy due to thermalisation is indicated by B in Figure 2.15, this loss occurs even if the electrons are created at the bottom of the conduction band and holes are created at the top of the valence band.

The third reason for the energy loss in the p-n junction solar cell is because the open circuit voltage is always smaller than the band gap energy because the Fermi level is located inside the energy bandgap. This loss is shown in Figure 2.15 by C. The fourth

reason is due to the fill factor is less than unity. This can be clearly noticed when the maximum power is extracted from the electrical characteristics of the photovoltaic solar cell where the operational voltage is always less than the open circuit voltage. Energy loss due to this mechanism is represented by D in Figure 2.15. Due to these mechanisms for energy loss of single p-n junction solar cells, what is converted by the photovoltaic cell into electrical energy is shown in the hatched part in Figure 2.15.

2.5.2 Energy Losses of Real Solar Cell

The energy conversion efficiency of the solar cells in practice is lower than the ideal solar cells due to additional losses which can be added to the fundamental losses mentioned in the previous section. These losses come from the fact that obtaining an ideal material quality for solar energy conversion under limited production processes capabilities and cost. The main three factors which degrade the performance of the solar cell are as follow:

- Reflection losses:

reflection losses come from the bare silicon wafer of the solar cells which reflects around 30% of the incident light. Therefore, around 70% of the solar energy is used in the conversion process by the cell. Minimising these losses can be through coating the front surface of the solar cell with anti-reflection coating material, texturing of the cell surface, the design of the front metal contacts which block portions of the incident light reaching the solar cell.

- Recombination losses:

not all the generated charge carriers can contribute to the solar cell current and voltage due to recombination which can occur on the surfaces or in the bulk material. The most significant recombination process in the p-n junction silicon solar cells is associated with the surface due to crystal lattice defects. This type

of recombination can be minimised with anti-reflection thin film deposition.

- Resistance losses:

The parasitic resistance losses include series and shunt resistances. Series resistance is caused by the sum of all the components that come in the path of current, the resistance of semiconductor bulk due to the movement of current through the emitter and base of the solar cell, semi conductor-metal contact resistance and the resistance of the metal contacts. It is favourable for the solar cell to have the series resistance as low a possible. However, the shunt resistance is due to manufacturing defects such as crystal defects or precipitates of impurity in the junction region. The effect of the shunt resistance of the solar cell is severe at low light irradiances since there will be less light-generated current. As opposite to series resistance, it is desirable to have the value of shunt resistance as high as possible.

In summary, it is necessary to reduce all these losses to increase solar cell conversion efficiency toward the ideal one. These losses due to technological reasons can be minimised by adopting special fabrication processes. Several ways to overcome the intrinsic properties of the semiconductor solar cells have been proposed to increase their energy conversion. These concepts are focused on a better use of the solar spectrum and referred as third generation photovoltaic [44].

2.6 Shockley-Queisser Limit

Shockley-Queisser (SQ) limit, also known as detailed balance limit, refers to the calculation done by William Shockley and Hans Queisser, which presents the maximum theoretical efficiency that can be achieved by a solar cell made from a single p-n junction under solar AM1.5 illumination [45]. The SQ limit is established by examining the amount of electrical energy that is extracted per incident photon. The calculations of SQ are based on the main followings assumptions:

- Illumination of the solar cell is performed under unconcentrated sunlight.
- The solar cell consists of one p-n junction.
- The solar cell is made from a single material, excluding doping materials.
- Photons with energy below the band gap energy of the semiconductor material is not absorbed.
- All recombination losses in the solar cell are radiative (i.e., no non-radiative recombination losses).
- One electron-hole pair is excited per incident photon. Energy is converted to heat from photons with energy in excess to the bandgap energy of the semiconductor material.

The calculations state that the calculated maximum conversion efficiency of 33% with regards to an illumination source of AM 1.5 solar spectrum and band-gap material of 1.34 eV.

2.7 Improving Conversion Efficiency of PV Cells

The fundamental spectral losses, discussed earlier in the chapter, can be as large as 50% for single junction silicon solar cell [46], while the detailed balance limit of conversion efficiency for single junction silicon solar cell determined by Shockley and Queisser to be 33% [45]. Several ways of maximising the conversion efficiency of solar cells have been proposed to address spectral losses and surpass the detailed balance limit through a better exploitation of the solar spectrum such as:

- Minimising reflection losses.
- Concentrating the irradiation.

Using Third or Next Generation photovoltaics [47, 48, 49] where the achieved results of using these concepts is due to advances in nanotechnology research. The conducted research is focused on down conversion concept of the third generation photovoltaics where some of the other concepts are listed below:

- Intermediate band gaps [50, 51].
- Multiple exciton generation [52, 53].
- Using multi junction/stacked cells [54, 55].
- Spectral conversion using Down/Up-Conversion [56, 57].

2.7.1 Spectral Conversion

Tuning the chemical and physical properties of the materials in nanometre-size has a significant impact on a broad range of technological applications, including photovoltaics. One of the important research areas of nanometre-sized materials for photovoltaic solar cells involves spectral conversion. Using nanomaterials for modification of the solar spectrum for single junction solar cells using down or upconverters

as a simple and cost effective method to enhance the conversion efficiency of solar cells [58].

Downconverters are located on top of solar cells as shown in Figure 2.16 as they are designed to modify the solar spectrum in which UV and visible light photons are converted to a more red rich photons where the silicon solar cell has better response leading to enhance the conversion efficiency of the solar cells.

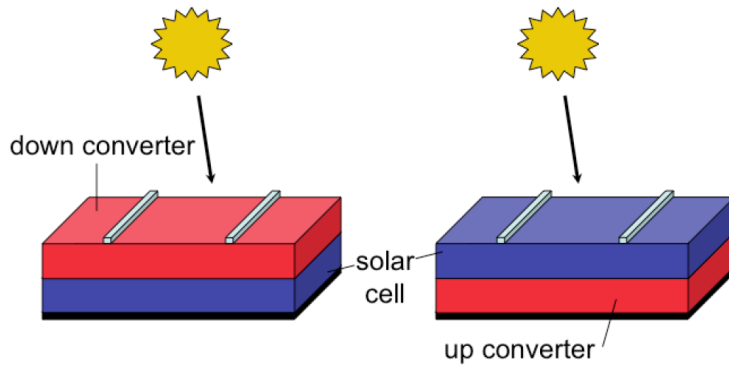


Figure 2.16: Schematic of a photovoltaic solar cell with down-converter layer on top (left) and up-converter layer on the backside of the solar cell (right) [59].

On contrary to downconversion, upconversion layer is required to be placed on the back of the solar cell as shown in Figure 2.16. Upconverter layer modifies the solar spectrum where it converts photons that are not absorbed by the solar cells to effectively shift infra-red part of the transmitted photons. Low energy photons into Near infra-red or visible photos where a reflector on the back surface of the solar cell is required. Figure 2.17 shows schematics of the energy diagrams showing photon absorption and subsequent down conversion, downshifting and upconversion.

For down conversion, high energy photons are converted into lower energy photons which can lead to quantum efficiency exceeding 100%. Thus, it is also known as 'quantum cutting' [60, 61].

Downconversion or downshifting is associated with one incident photon per conversion. Therefore, the intensity of the downconverted/downshifted emitted photons

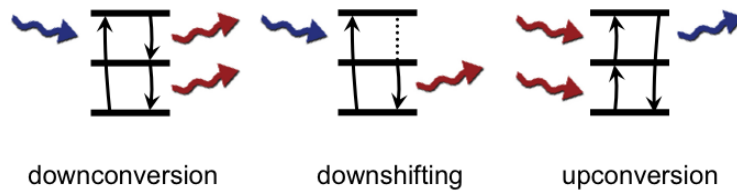


Figure 2.17: Schematics of energy diagrams demonstrating and subsequent downconversion, downshifting and upconversion [59].

scales linearly with light intensity where for upconverting which involves two photons, the intensity of the converted emitted photon scales quadratically with incident light intensity.

In the case of upconversion, two or more low energy photons are converted into high energy photons [35]. Also, as can be seen from Figure 2.17 Down shifting is similar to down conversion with the main difference that is one photon is emitted and therefore the quantum efficiency of the quantum efficiency of the conversion process is lower than unity [58, 61]. Therefore, it is preferable to use a downshifting with quantum efficiency close to unity to minimise losses. Downshifting is also known as Photo-luminescence [35].

By using upconversion, downshifting or downconversion layers, the performance of the solar cell is affected optically where the changes in the values of the short circuit current will be noticed through the application of these converters.

2.8 Building Integrated Photovoltaics

PV modules are commonly installed on supporting structures but in BIPV instead of mounting the PV modules on separate structures, it can be mounted directly onto the building or integrated into the building structure [62]. BIPV systems represent a remarkable, alternative approach for increasing the available area for electricity production and potentially for further reduction in the cost of solar electricity.

PV modules are integrated into the buildings with roof or facade mounting. Figure 2.18 shows photographs illustrate different examples of the BIPV systems. BIPV systems combine other functions of the building envelope with electricity generation. Some of these advantages are summarised as follows [63]:

- External shading devices containing PV cells.
- Roofing tiles, replacing traditional pitched-roof materials.
- PV systems integrated into or mounted onto buildings save the cost of land.
- Cutting down the cost of cabling because buildings are normally connected to the grid.
- Ventilated facades where PV is used as the external cladding element.

Two elements of the solar modules namely the glass and solar cells provide architects an enormous degree of freedom in the designing possibilities in BIPV. Opportunities in the design of the solar cells include cell shape, cell colour, cell size and geometric arrangement of the cells within the solar module [65, 66].

Solar cells are coated with an anti-reflection material to optimise its light collection and thus its electrical conversion efficiency. Commercial solar cells with a single layer of anti-reflection coating of silicon nitride on multi-crystalline solar usually have bluish reflection colour while the best mono-crystalline cells usually have a black appearance. By variation of the thickness and the surface texture, a variety of colours



Figure 2.18: Photographs showing different examples of the BIPV systems.

A shows PV systems mounted onto the existing roof [64], B shows an example of roofing PV system replacing the roof tiles [65], C shows a prominent example of the facade integration of solar modules at Doxford Business Park in Sunderland [65], D shows monocrystalline PV in a semitransparent module [65].

can be obtained. The selection of the colour is often combined with a suitable glass colour to enhance or reduce the colour contrast. Figure 2.19 illustrates the variety of colours that can be obtained in the PECVD coating.

The aesthetic impression of a solar module becomes necessary in BIPV, including its colour. The variety of solar cell colours and shapes available to architects and BIPV system designers is still very limited. As a result, this is a barrier to the widespread use of PV modules as a constructional material [67].

Two elements of the solar modules namely the glass and solar cells provide architects an enormous degree of freedom in the designing possibilities in BIPV. Opportunities in the design of the solar cells include cell shape, cell colour, cell size and geometric arrangement of the cells within the solar module [65, 66]. The design pos-

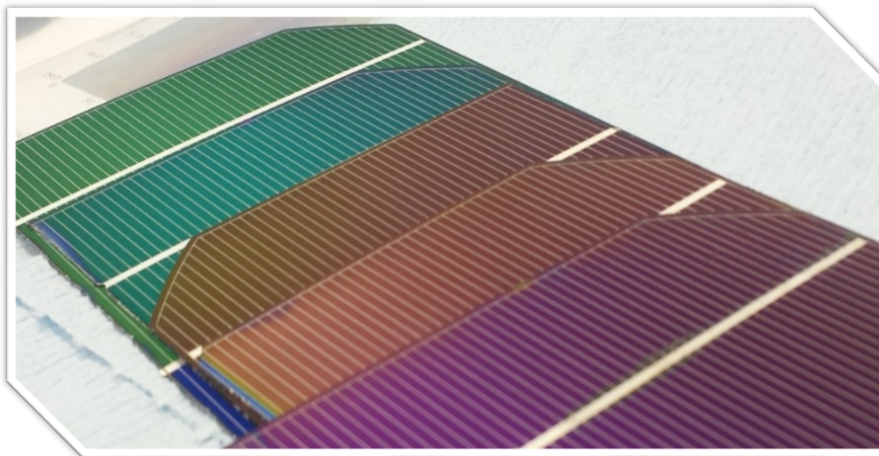


Figure 2.19: Various colours of solar cells can be obtained in the PECVD coating.

sibilities of the present day in BIPV requires engineers to find a solution for every taste. When the aesthetic concerns of BIPV are of importance, the efficiency of the solar module could be compromised. Therefore, access to efficient and coloured solar cells is essential for the further development of BIPV systems.

Chapter 3

Characterization of Crystalline

Silicon Solar Cells

This chapter presents the equipment and instruments used for solar cells characterisation at Brunel University. It describes the functions of particular devices, the experimental procedures and the approach in carrying out of these experiments.

3.1 Silicon Solar Cells

Photovoltaic solar cells used in the experiments were a mono-crystalline silicon solar cells model XS156B3 from (Motech Industries, Taiwan). The essential features of the mono-crystalline silicon solar cells are shown in Figure 3.1. It is made from a thin (200 ± 20 micron) wafer cut from a pure silicon crystal which has been doped with boron. The cuts have a square shape of 156×156 mm² with cropped corners. Phosphorus is diffused into the wafer cut to form a p-n junction a fraction of a micron below the front surface. This type is called "n-on-p" which is the opposite to the p-on-n cell by diffusing boron into a phosphorus doped wafer. It is common in commercial cells to have an n-on-p type where p-layer is thicker than n-layer because n-type silicon

has a higher surface quality than p-type silicon. Moreover, phosphorous diffusion is easier compared with boron diffusion and the minority carrier in p-type base is electron, which features a higher mobility. However, n-type substrate is more tolerant to chemical and crystallographic defects. Therefore, it is placed at the front of the cell where most of the light are absorbed. N-on-p type makes the top of the cell a negative terminal and the rear of the cell a positive terminal. The front metal contact is in the form of a narrow fingered grid with 1.4 mm silver busbars, while the back contact is made of 2.5 mm discontinuous soldering pads of silver on the aluminium surface which cover the entire back surface of the solar cell. The front surface of the silicon solar cell is textured using an anisotropic etch during the manufacturing process. The etching process of the solar cells forms small pyramids structures on the surface of the PV solar cell. Moreover, the front has a dark silicon nitride anti-reflection coatings with a thickness of 80 nm.



Figure 3.1: Motech crystalline silicon solar cell [68].

3.2 Preparation of Silicon Solar Cells

Solar cells were split into three equal parts by CO2 laser cutting model machine TMX90 from (CTR Lasers, UK). Solar cells were cut into smaller sizes due to technological limitations such as the size of the coating chamber or due to economical reasons

to minimise the waste of the material used especially in the initial experiments.

The CO₂ laser cutting system is capable of cutting and engraving a broad range of materials, including acrylics, woods, fabrics and even thin sheet metals. The laser cutter is computerised and operated under the supervision of a skilled technician. The DC laser cutter is shown in Figure 3.2 is equipped with a water chiller unit fitted with interlocks to ensure the protection of the laser tube. The cutting process occurs when the laser source generated a laser beam and directed to the cutting head by mirrors where a lens focuses it to a small spot. The spot is placed on the surface of the material to be cut. Solar cells were cut using 100 W DC CO₂ laser power. Laser power is the total energy emitted in the form of laser light per second. The intensity of a laser beam is equal to its power divided by the area over which the power is concentrated.

In the experiments, focusing a 100 W laser beam with a diameter of 0.1 mm will result in a power density of approximately 125 W/mm². The design of the cut is made using Easycut 5.3 software. Before cutting the solar cells, a square of 15.6×15.6 cm² with cropped corners similar to the shape of the solar cell is engraved on a wooden plate. This step is made to ensure an accurate cutting process of the silicon solar cell. After that, the solar cell is placed on the engraved square properly. Then, the fume of the laser machine is shut and the cutting process starts by pressing START button. Once cutting process is completed, the solar cell is removed and cutting a new solar cell can not be started until warning light stop flashing which indicates that the water temperature of the cooling system is outside the operating range (22±3°C).

3.3 Electrical Measurements of the Solar Cells

Electrical measurements were carried out on the illuminated solar cells where solar cells are connected to a temperature and electrical measurement units controlled by



Figure 3.2: Laser cutter (Top), software set-up in computer (Left) and solar cell layout on laser cutter (Right).

a computer as shown in the schematic in Figure 3.3

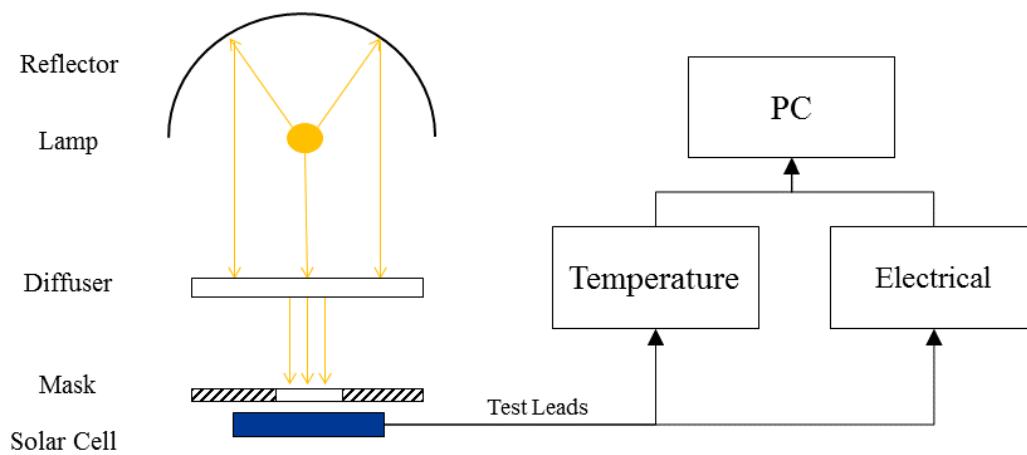


Figure 3.3: Electrical measurements set up.

The set-up of the system shown in Figure 3.3 is established to simulate the standard test conditions of the silicon solar cells. The illumination source of the solar

simulator is Metal Halide 1000W lamp. Metal Halide lamp has a colour temperature of 6000K which closely matches that of natural sunlight 5800K. The spectral distribution of the lamp is obtained from the manufacturer specification as shown in Figure 3.4 where it shows the spectrum of the lamps and the estimated amount of irradiance in each wavelength interval is presented in Table 3.1. Obtaining an illumination in-

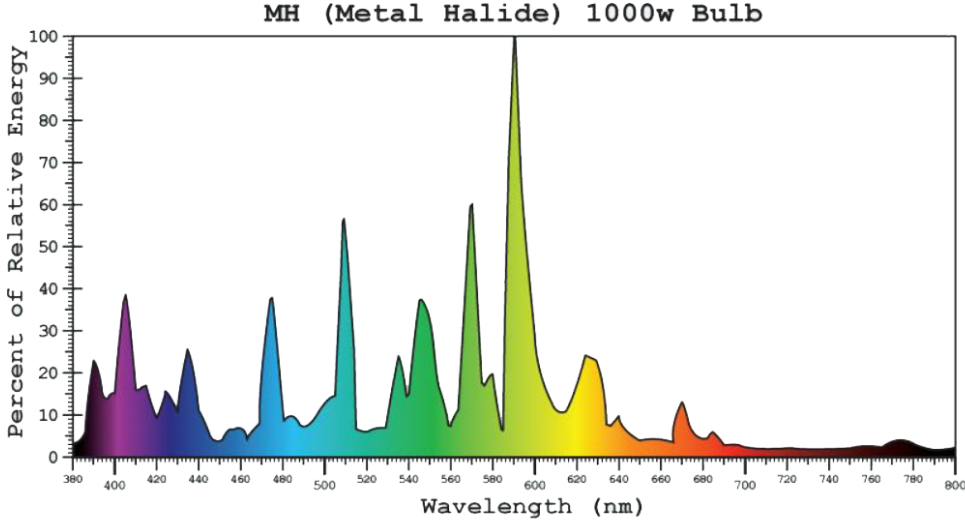


Figure 3.4: Spectral distribution of the illumination source [16].

tensity of one sun in the study is established by adjusting the distance between the illumination source and the solar cell and also by adjusting the power of the illumination source which is controlled by adaptable ballasts. The illumination intensity can be obtained from a reference cell calibrated cell by GBsol. A photograph of the reference solar cells is shown in Figure 3.5. The study of the spectral distribution of illumination source over a large is reported in [16].

Table 3.1: Spectral distribution with percentage contributions each for wavelength band [16].

Wavelength Band (nm)	Value (W/m ²)
300-1100	815±13.7
1100-2800	46±26.6
>2800	64 ± 33.3

Using a mask on the solar cells plays many advantages when testing the solar cell



Figure 3.5: Reference cell calibrated by GBsol.[16].

such as minimise the spectral variation over the illuminated area as well as in cases when the coating material is applied partially on the solar cell [69]. In the experiments, a mask from an acrylic material with a circular hole with a diameter of 32 mm is made for covering the solar cell during the electrical testing. The acrylic mask is covered with an adhesive mirror roll to make sure that infrared radiation cannot pass through it. Figure 3.6 shows a schematic of the mask used in the experiments. The method for

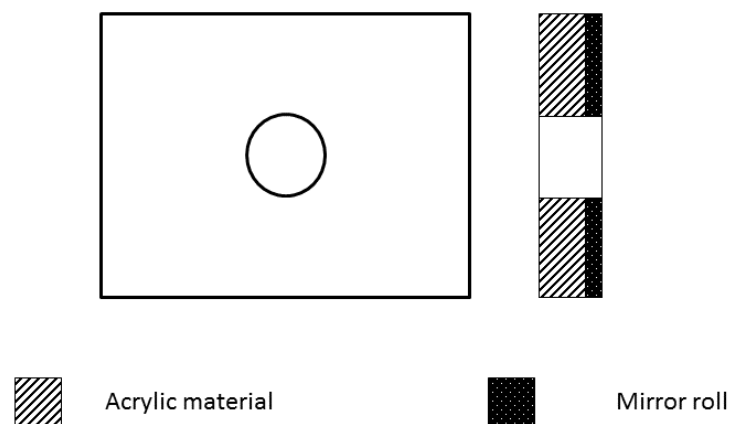


Figure 3.6: Schematic of the Mask used in the electrical measurements.

characterising the voltage-current characteristics of solar cells is to use a parameter analyser which employs measurements ports known as Source-Measurement Units (SMUs). SMU is capable of providing a known current and measuring the resulting current or vice versa. The used SMU in the experiments is Keithley 2601B source-meter and the I-V curves were obtained by sweeping the voltage across the solar cell

electrodes using an embedded TSPEXpress software.

Analysing I-V parameters have been obtained from the I-V curves by numerical interpolation I-V measurements of the measurements performed under conditions of $T=25\text{ }^{\circ}\text{C}$ and illumination of 1000 W/m^2 and illumination surface area of 8.544 cm^2 .

3.4 Material Deposition Machines

This section shows the equipment used for deposition of thin films on the crystalline silicon solar cells using PECVD system and sputtering deposition machine.

3.4.1 PECVD Machine

Deposition of silicon oxide films on silicon solar cells was conducted using a 13.6 MHz rf powered, capacitively coupled, PECVD process (sometimes referred to as plasma assisted, PACVD) at Experimental Techniques Centre (ETC). The experimental configuration of the PECVD machine is shown in the Figure 3.7. The samples are placed horizontally on the cathode plate which is mounted in a stainless steel grounded chamber of 50 cm in diameter and 50 cm in height. For deposition process, a mixture of argon and Tetramethylsilane (TMS) gas was used. The flow rate of the gases is controlled through Mass Flow Controllers (MFC). The gas was introduced into the reactor through a grating at the top of the chamber and evacuated off axis at the base below the cathode.

3.4.2 Sputtering Deposition Process and QBox

Sputtering deposition is widely used technique to deposit thin films of material onto a surface of the substrate. This technique is part of the Physical Vapour Deposition (PVD) techniques which include thermal evaporation and pulsed laser deposition.

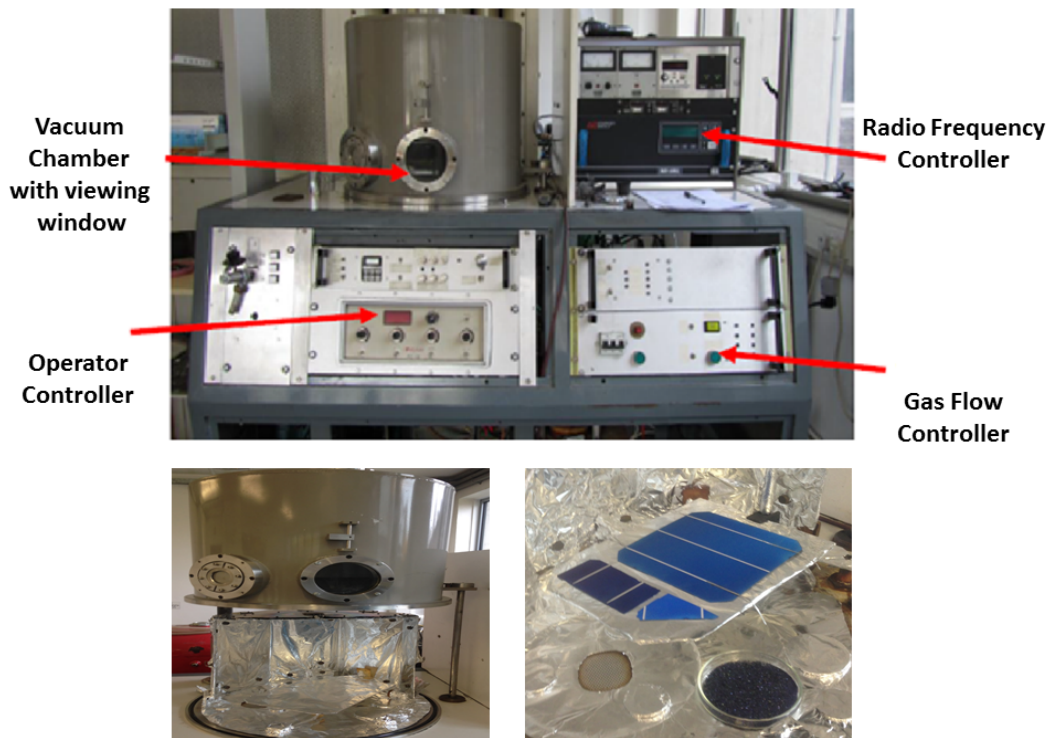


Figure 3.7: Photograph of PECVD Coating System.

Sputtering is based on creating a gaseous plasma and then accelerating the ions of this plasma into the source material, the target, the source material is eroded by ion bombardment via energy transfer resulting in atoms or/and cluster of atoms are being ejected from the target and deposited on the substrate. Sputtering system can be powered by a variety of methods. It can be powered using Radio Frequency (RF) or Direct Current (DC) modes.

3.4.2.1 DC Sputtering

This method is considered the simplest and least expensive way to operate the machine is by using a DC power supply. It is a very efficient method of thin films deposition for conductive materials. Using this method, a constant voltage can be used to accelerate the ions bombardment to the desired velocity. Once the ions strike the surface, the resulting charges can move freely about the material to prevent any charge build up. However, this method is not suitable for using a dielectric material

as this will accumulate the sputtered charged ions at the cathode leading to a positive charge build up which neutralise the cathode bias and stop the deposition process [70].

3.4.2.2 RF Sputtering

In DC systems, preventing positive charge builds up on the cathode (target) for depositing insulating materials would require high unachievable voltage. Therefore, RF sputtering is suitable for dielectric targets where the charge builds up is prevented by an alternating voltage which allows the ions to repel from the surface during the positive half of the cycle.

3.4.2.3 QBox Series System

The system features a large access door allowing the user to place the substrate on the stage by hand quickly and easily. The coating system is fully automated by computer using TITANIUM Control System Software package which logs and controls all features of the system. Automatic pump down and vent of coating chamber can be performed using a pre-programmed feature of the software. The system is equipped with a 300l/s turbo pump that is backed by a dry scroll pump. This combination allows for the sputtering system to maintain a base pressure of 2×10^{-7} torr. The thickness of the coating can be monitored by a Quartz Crystal deposition Monitor (QCM) which is placed directly below the substrate for calibration. The system is equipped with three CUSP series magnetron sputter sources mounted on flanges located at the base of the system and are arranged in a circular pattern aimed at a common focal point with a 30 degrees tilt angle from the table normal. The distance between the target and the substrate is 16 cm to the centre of the table.

The CUSP sources can be used for RF and DC power. The RF power supply to

bias the target during deposition work at 13.5 MHz. Figure 3.8 shows photographs of the Mantis deposition system where (A) displays the deposition and control units, (B) shows the coating chamber and (C) illustrates the coating chamber during the deposition process.

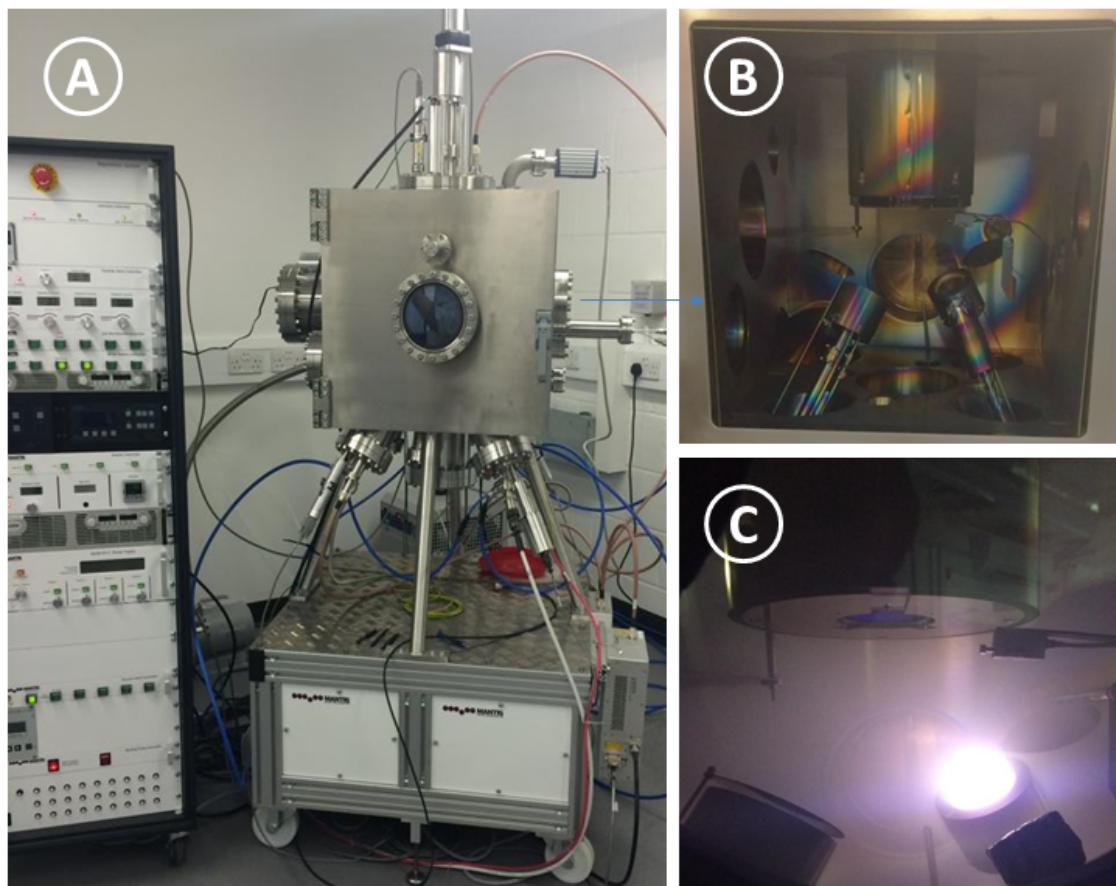


Figure 3.8: Photographs of the Mantis deposition system - QBox Series System. (A) displays the deposition and control units, (B) the coating chamber and (C) the coating chamber during the deposition process.

3.5 UV/Vis Spectrophotometer

A spectrophotometer is a device that measures the light intensity over a defined electromagnetic spectrum. A conventional spectrometer system includes a broadband light source, a light diffraction splitter and a detector where the system is connected

to a computer for data acquisition and processing through a specific software.

In this work, optical properties of the photovoltaic solar cells are measured using PerkinElmer Precisely Lambda 650S UV/Vis Spectrometer at Brunel University. The spectrometer features a double beam, double monochromator and ratio recording optical system where all the optical components in this system are coated with silica for durability. The spectrometer contains two radiation sources, a pre-aligned Deuterium (UV) Lamp (DL) and tungsten-Halogen Lamp (HL) over the working range of the spectrometer which extends from 900 to 190 nm. The spectrometer scans from higher toward lower wavelength with spectral bandwidth from (0.17-5) nm in 0.01 nm increments of the UV/Vis range [71]. During the course of measurements, a source of

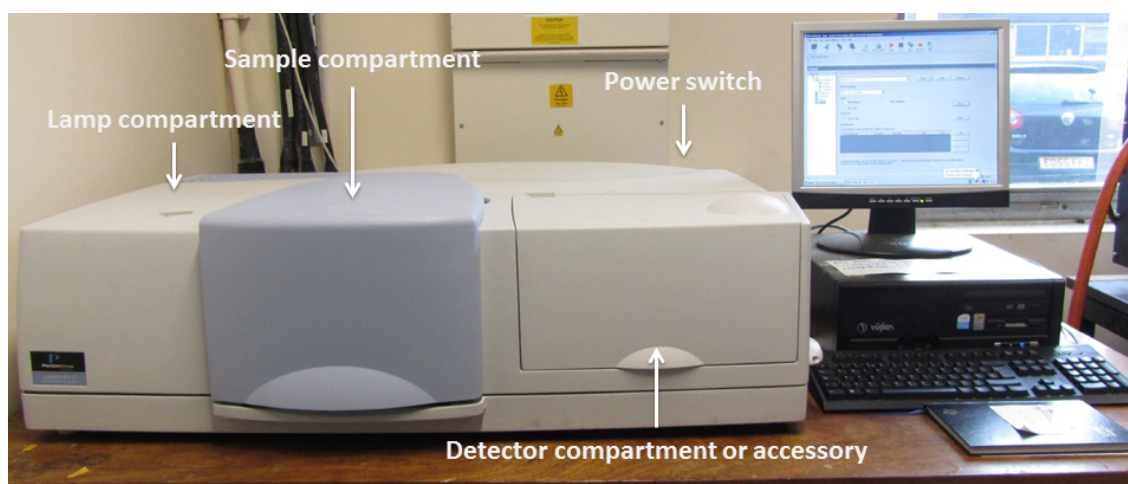


Figure 3.9: Photograph of PerkinElmer Precisely Lambda 650S UV/Vis Spectrometer.

light impinges on diffraction gratings is split into a single wavelength. Then, through a series of mirrors and other optical elements, the path of wavelength selected beam of light is directed to the measured object. The light reflected or transmitted by the sample is captured by an optical detector, R955 Photomultiplier model which gives high energy throughout the whole UV/Vis range, sensitive in a wavelength range compatible with the selected beam. The collected information from the detector is then compared wavelength by wavelength to reference transmittance and reflectance spectra. The optical information is recorded using UV Winlab Software Kit. Therefore,

the measured spectra are reported in percentage.

A photograph of the used spectrometer in this thesis is shown in Figure 3.9. This technique allows the measurement of transmittance and reflectance of a specimen with respect to the wavelength of incoming light. Thus, the absorption of the material can be calculated from equation 3.1 where absorption is light that is not transmitted or reflected by material:

$$A(\%) = 100(\%) - T(\%) - R(\%) \quad (3.1)$$

where A=absorptance, T=transmittance, and R=reflectance.

Two types of the slides were used in the experiment. Clear quartz and glass slides with 1 mm thick from (AdValue Technology, USA) are used. Before any deposition, slides were ultrasonically cleaned in the following sequence: 10 minutes in deionised water; 20 minutes in isopropanol alcohol; then left over night to dry in the laboratory fume hood.

3.6 Scanning Electron Microscopy

Scanning Electron Microscopy (SEM) was used for both structural and morphology analysis of coated samples. An ultra high-performance field emission scanning electron microscope, ZEISS SUPRA 35VP field emission SEM, located at Brunel Experimental Techniques Centre (ETC), shown in Figure 3.10 is used in this study to observe the microstructures of the coated solar cells and to record images.

The microscope is equipped with both high vacuum and variable pressure capability. The field emission source and Gemini column provide with a high-resolution capability while the variable pressure system enables imaging and analysis of the specimen in their natural state which allows non-destructive examination of the environmentally sensitive specimen as well as an insulating specimen. The SEM is also

equipped with a suite of analytical techniques such as Energy Dispersive X-ray Analysis (EDXA) for material composition and phase detection.

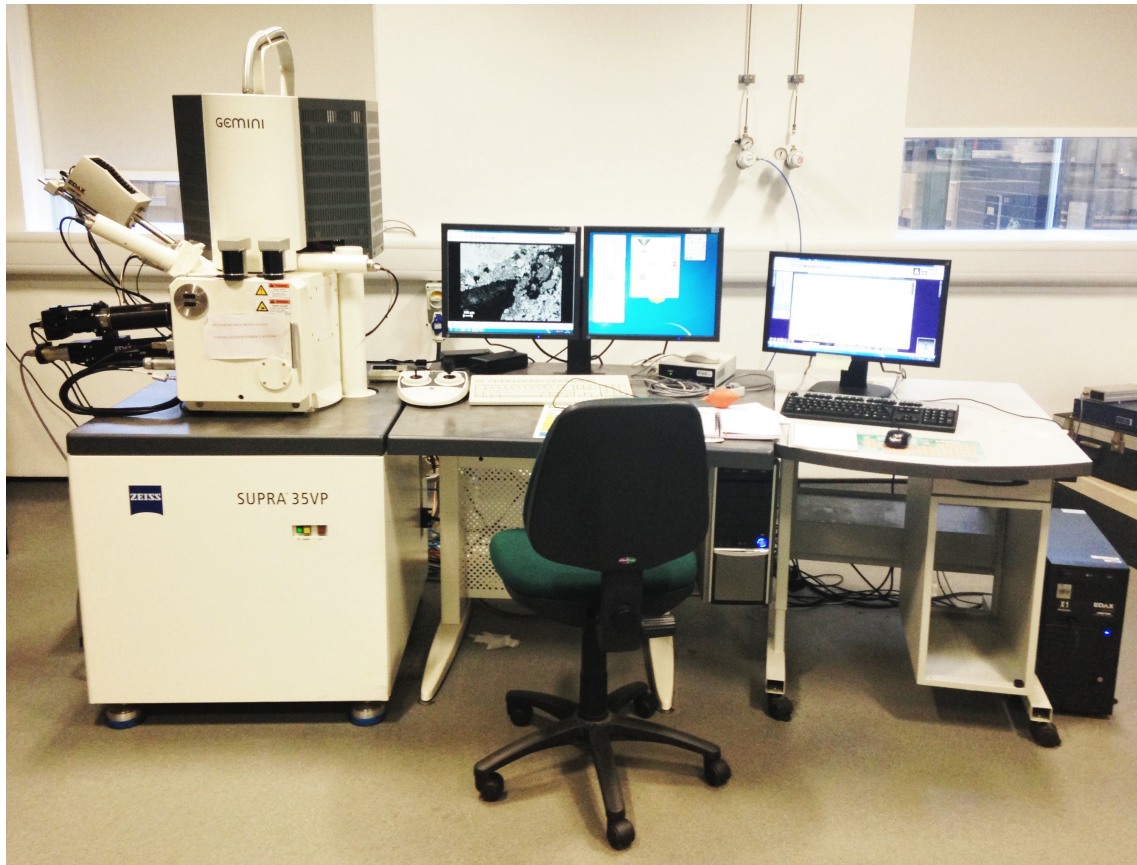


Figure 3.10: ZEISS SUPRA 35 VP Scanning Electron Microscope.

3.6.1 SEM Sample Preparation

For the purpose of obtaining a high-quality SEM image, the specimen should present an excellent electrical conductivity to prevent charging, good thermal conductivity to reduce damage due to the heating effect of the electron beam, mechanical rigidity to reduced the effects of vibration and stability under vacuum [72]. Preparation of the samples for SEM imaging can be divided into two stages: epoxy preparation and sputter coater.

3.6.1.1 Epoxy Preparation

The first stage starts with slicing the sample using a clean diamond cutter to cut the required size of the coated silicon solar cell to fit the mould. Then, the moulds are produced using EpoxiCure obtained from Buehler company. EpoxiCure consists of two parts, a resin and a hardener. Three parts of the resin are mixed with one part of the hardener in a disposable mixing cup for two minutes using a mixing stick. Then, the mixture is poured into the mould where the sample is resting on a metal mounting clip if necessarily. The epoxy resin takes approximately 6 to 8 hours to cure at 28 degrees.

The next step is to grind the surface of the mould on abrasive paper. Silicon carbide abrasive papers discs from MetPrep Metallographic Materials are used. The grinding starts using a coarse grit and gradually toward a finer grit sizes. The samples are held with moderate pressure on the polishing wheel on which the abrasive is placed on.

3.6.1.2 Sputter Coater

Samples are coated with platinum using a sputter coater which is a standard method for preparation of the non-conductive or poorly conductive specimen for observation in SEM. In this study, POLARON sputter coater shown in Figure 3.11 is used. Details on the coating procedures can be found in the appendices.

3.7 High Pressure Stirred Reactor and Furnace

Figure 3.12 shows the fume-hood at the lab which contains an autoclave and a furnace. The used autoclave model is Parr Model 5500 high-pressure compact stirred reactor with a volume of 300 ml. The reactor is connected with a temperature



Figure 3.11: Polarab sputter coater.

controller Parr-4836.

Thermal annealing for the material is carried out using Lindberg/Blue M Mol-datherm 1100 °C box furnace which includes ceramic fibre insulation and heating element composites to minimize outer surface temperatures while maintaining uniform heat distribution within the chamber [73]. In chapter 5, the stirred reactor is used to fabricate titania nanoparticles. In Chapter 6, the furnace is used to oxidise titanium films and also to curve EVA layer.



Figure 3.12: High pressure stirred reactor and furnace.

3.8 Phosphor Material Characterization

Details on the instruments and sample preparation methodology used in Chapter 7 including X-ray powder diffraction, photo-luminescence spectroscopy and differential scanning calorimetry are described in the following subsections:

3.8.1 X-ray Powder Diffraction

The crystallinity and phase identification of the rare earth material is analysed using X-ray Powder Diffraction (XRPD). Bruker D8 ADVANCED X-ray powder diffractometer, shown in Figure 3.13 (right), equipped with copper source and LynxEyeTM silicon strip detector is used to record diffraction pattern of the sample.

The machine is operated by a personal computer, and the resulting XRPD patterns are refined, and the average size of crystallites are calculated by Total Pattern Analysis Solution (TOPAS) software. Preparation of powder specimen for XRD material is carried out by pressing the powder in a standard sample holder by glass slide

to make a flat surface before placing the specimen holder in XRD scanning chamber. Data were collected from 5° to 100° (2θ) for 35 minutes in the step scan mode.

3.8.2 Photo-luminescence Spectroscopy

The absorbed incident light by the down-converting phosphor material is re-emitted at longer wavelength producing photons that better match the solar cell spectral response. Thus, the physical process of the luminescence may enhance the efficiency of the solar cell. Characterization of luminescence properties of the rare earth doped phosphor material requires a dual monochromator system in which it includes an excitation and an emission monochromator.

Both monochromators showed in Figure 3.13 (left) can be used together to record material excitation and emission properties. Bentham M300 phosphor research spectrometer embedded BenWin⁺ software. The emission spectrum is recorded from 300 nm to 800 nm using 291 nm UV light as an exciting source.

3.8.3 Differential Scanning Calorimetry

Differential Scanning Calorimetry (DSC) is a thermal analysis technique that measures the temperature and heat flow accompanying with transitions in materials as a function of time and temperature in a controlled environment. These measurements provide with quantitative and qualitative information about the physical and chemical changes that involve an endothermic or exothermic process or changes in heat capacity [74]. The DSC instrument was also used to determine the curing process of EVA utilised as binder in the phosphor composite coating. In the past, this was determined using a method based on solvent extraction. Recently, it was shown that DSC measurements can also be used [75].

DSC measurements were carried out using a single-furnace DSC 6000 controlled

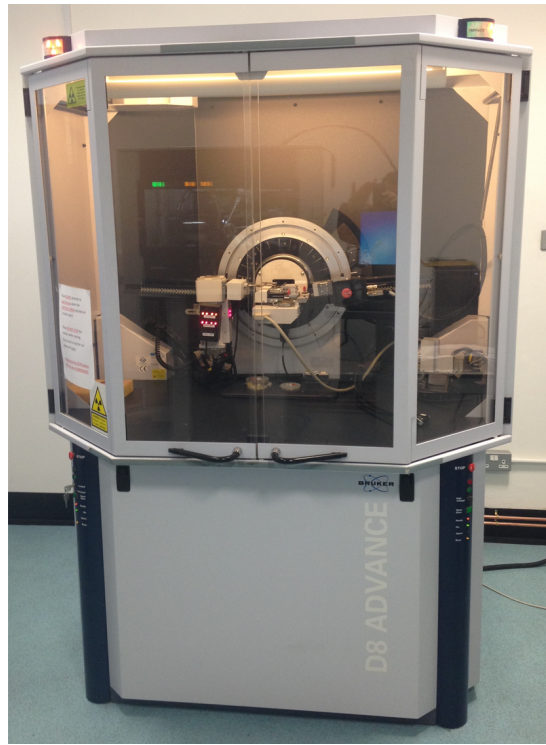
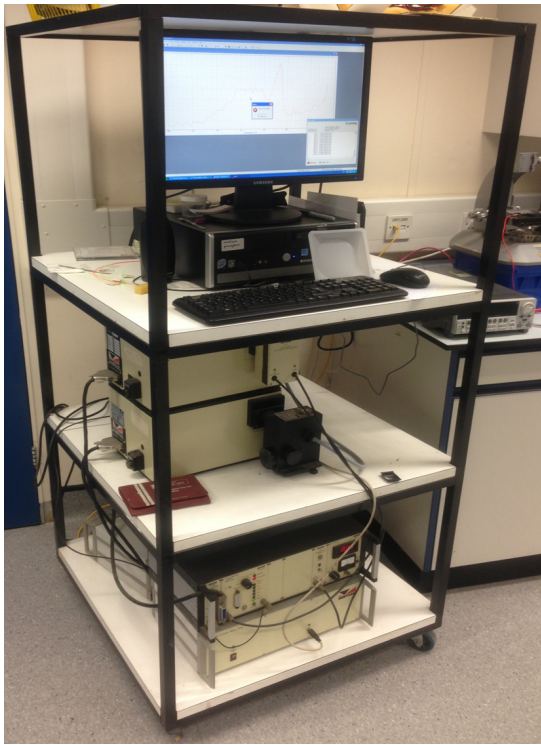


Figure 3.13: Bentham M300 monochromator detector system (left) and Bruker D8 ADVANCED X-ray powder diffractometer (right).

by a personal computer from (PerkinElmer, USA) equipped with cooling accessory Intracooler 2P mechanical refrigerator as shown in Figure 3.14. Nitrogen zero grade from (BOC, UK) is used as the sample purge gas at 20 ml/min. For, DSC measurements, small EVA discs of about 10 mg were cut and encapsulated in a standard aluminium pan.

3.9 Measurements

Electrical characteristics of the coated and uncoated solar cells were determined through comparative current versus voltage (I-V) and power versus voltage (P-V) curves. Electrical characteristics of the solar cells were obtained by connecting the cell to a Keithley 2601B source-meter with an embedded TSPExpress software.

Solar cells were tested with illumination surface area of 8.544 cm^2 using a visible

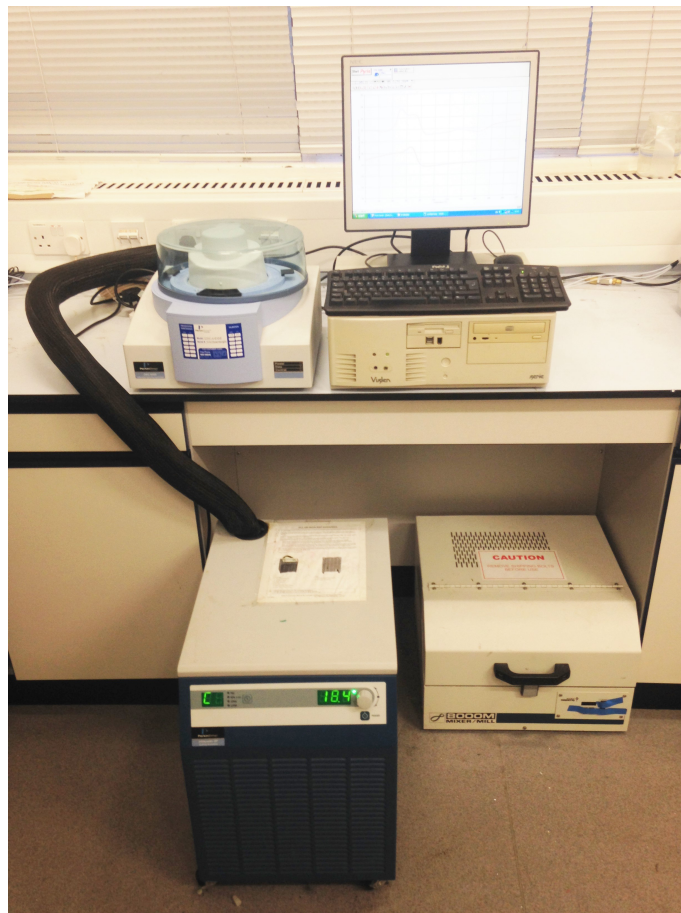


Figure 3.14: Differential scanning calorimetry system.

and ultraviolet light sources at a temperature of 25 °C and light intensity of 1000 W/m² and 46.1 W/m² respectively. Electrical measurements of the solar cell parameters are short circuit current (I_{sc}), open circuit voltage (V_{oc}), fill factor (FF) and the maximum power (P_{max}) can be obtained from these curves.

Prior to the measurements, the light intensity was measured with a reference cell calibrated by GBSOL and solar power metre (Di LOG-model: S102) instrument to check the visible irradiance and UV light metre (LT Luton-model: UV-340) device was used to check ultraviolet irradiance. All the samples were tested using the same conditions.

Reflectance spectra were measured at room temperature using PerkinElmer Lambda 650 UV/Vis spectrophotometer in a spectral range from 200 to 850 nm. The structural and chemical composition analysis of the solar cells were carried out before and after deposition of silicon oxide films using a ZEISS SUPRA 35VP field emission Scanning Electron Microscope with associated Energy Dispersive X-ray (EDX) analysis was used to confirm the presence of the coating.

Photoluminescence (PL) and Photoluminescence Excitation (PLE) spectra were obtained using Bentham M300 monochromator with Xenon lamp as light source. Reflectance spectra were measured at room temperature using Perkin-Elmer Lambda 650S UV-Vis spectrophotometer in a spectral range from 200 to 800 nm.

The film morphology is analysed using a ZEISS SUPRA 35VP field emission scanning electron microscope (SEM). Energy dispersive X-ray analysis (EDX) was used to confirm the presence of the coating. IQE measurements were carried out using SPEQUEST system by LOT-QuantumDesign.

Chapter 4

Silicon Oxide for PV Solar Cell

Silicon oxide ARC films can reduce sunlight reflection and increase the energy conversion of industrially manufactured crystalline silicon solar cells. In this chapter, single and double layers of silicon oxide films produced by low-temperature PECVD are deposited on commercial mono-crystalline silicon solar cells as one possible way to increase the efficiency of silicon solar cell at low cost. TetramethylSilane, ($C_4H_{12}Si$), and potassium permanganate ($KMnO_4$) materials are respectively used as a precursor for silicon layer deposition onto the cells and an in situ oxidation agent. The nanofilm of silicon is simultaneously oxidised using potassium permanganate compound present in the PECVD chamber.

This study compares the electrical characteristics and optical properties of mono-crystalline silicon cells before and after coating with single and double layers of silicon oxide films. The PV cells surface chemical composition was analysed using SEM. Reflectance analysis results are also presented. The experimental results show that various colours of the mono-crystalline silicon solar cells can be obtained using PECVD technique that can be of great importance for BIPV.

4.1 Introduction

Silicon is a leading material for the commercial production of low-cost PV solar cells given the non-toxicity, raw material cost and abundance of silicon [76]. PV solar cells based on crystalline silicon account for the largest share of production of all types of solar cells on the market, representing about 90% of the world total PV cell production in 2014 [7]. The cost effectiveness of silicon solar cells can be further reduced by improving the solar cell efficiency while maintaining low fabrication costs.

The primary spectral losses in a single junction solar cell are high due to the mismatch between the irradiance incident of the solar spectrum and the spectral absorption properties of the material leading to the thermalisation of the charge carriers [57]. Enhancing the energy conversion of the conventional solar cell above the theoretical limit of 33% calculated by Shockley and Queisser could be approached by preventing thermalisation of the charge carriers with the help of down conversion materials [45, 77].

To improve the competitiveness of crystalline silicon solar cells through reduction of the optical and electrical losses, thin films ARC can play a significance role in enhancing light absorption and reducing the surface reflection of incident light which can result in an increase in the conversion efficiency of the solar cell. Without a proper ARC layer on the surface of silicon solar cells, around 37% of the solar irradiation is reflected from the cell's surface under terrestrial solar irradiation of Air Mass 1.5 [31].

Commercial silicon solar cells are usually coated with silicon nitride deposited by low-temperature PECVD as ARC layer due to its unique combination of good electronic and optical properties which contributes to solar cell conversion efficiency enhancement as a result of maximising the photo-generated current with the silicon substrate and reducing recombination at the surface of the silicon solar cell [78]. However, it has the disadvantage of narrow wavelength range for light absorption and

high absorption in the UV light band reducing the short circuit current and thus the solar cell conversion efficiency [79]. To solve these problems, a double ARC is applied to the solar cell using silicon oxide.

The silicon oxide/silicon nitride stack is more promising due to its advantages of surface passivation, absorbing light in broader wavelength region and has lower reflectance compared to single layer ARC. Moreover, silicon oxide film can serve as an ARC and down conversion layer on the Si solar cells due to its optical property of absorbing ultraviolet radiation and re-emitting the absorbed energy by these films as red light where the Si solar cell has greater response [44].

4.2 Related Work

The need for cost reduction in the fabrication of crystalline silicon solar cells involves new technological solutions such as the use of safer processes and maintaining low processing temperature.

Silicon oxide films can be grown out on a silicon substrate by thermal oxidation. However, thermal oxidation is high-temperature processing (reaching about 1000°C) and relies on Si substrate consumption. For the low-temperature processing, alternative deposition techniques have to be employed. Among various deposition techniques such as Liquid Phase Deposition (LPD), sputtering, spin-on glass, etc. Chemical Vapour Deposition (CVD) is a superior approach for silicon dioxide deposition due to its unique versatility, possibility of deposition at low temperature. As for photovoltaics, the device continues to scale down the diffusion of the dopant in the semiconductor must be minimised to make the junction shallow. Therefore, the fabrication temperature must be as low as possible. Also, low-temperature deposition can reduce process induced crystallographic damages, degradation of metal contacts and contamination by impurities diffusion due to the requirement for low-temperature

deposition.

In recent decades, silane has been widely used a raw material when preparing silicon containing thin films using PECVD systems [80, 81]. However, silane gas is toxic and has a pyrophoric nature that can initialise an explosion hazard especially in mass manufacturing processes which require a considerable amount of silane gas to be stored on site increasing the explosion danger. Currently, organosilicon as in liquid/vapour-phase TMS has been adopted as a source of silicon instead of hazardous silane gas.

Cojocar et al. showed that the tetramethylsilane is a good candidate for replacing the silane gas in photovoltaic cell manufacturing processes [82]. TMS is stable, non-pyrophoric and volatile at room temperature. The TMS volatility, due to its high vapour pressure, has the cost advantage of not requiring heating apparatus as the high vapour flows can be obtained without heating the liquid line.

Kim et al. improved the efficiency of mono-crystalline silicon solar cells as a result of reducing the reflected light from the surface of the solar cell by coating the solar cells with silicon nitride and silicon oxide by PECVD method. They demonstrated an increase in the electrical conversion efficiency with an absolute enhancement of 0.31 by comparing a single anti-reflection coating with SiN_x with double anti-reflection coating with $\text{SiN}_x/\text{SiO}_2$ [78].

Carrilo-Lopez et al. showed that silicon solar cells coated with silicon oxide produced by low-temperature PECVD improve the performance of the cells due to the increase in the short circuit current in the UV range as results of the red luminescence of these films containing silicon nanoparticles. These films have excellent optical properties of absorption of UV radiation and then re-emitted as red light which arrives the active region of the p-n junction. Thus, increasing the generated photo-current of the cell [44]. There are two principal mechanisms for the generation of the photoluminescence of non-stoichiometric silica films due to quantum confinement due to

nano-crystals and defects presented in the material [44, 83]. Also, the excellent transmittance of those films of greater than 80% for the wavelength greater than 400 nm plays a role in the obtained enhanced performance of the cells as the material does not absorb the light within the visible and near infra-red light range [44, 84]. As results, the re-emitted red light will be absorbed by the solar cell. Therefore, these films can be an excellent passivation material because they absorb the high energetic photons and generates photo-luminescence where the solar cells have a greater response.

This chapter presents an investigation into the electrical and optical parameters of commercial mono-crystalline silicon solar cells before and after coating with single and double anti-reflection layers of silicon oxide using low-temperature PECVD and TMS as a silicon precursor and oxidised in situ with potassium permanganate without a significant increase in the fabrication cost.

4.3 Experimental Method

4.3.1 Silicon Precursor

In the experiments, TMS is used as a silicon precursor. TMS is an organosilicon compound with chemical formula ($C_4H_{12}Si$) and the molecular structure is shown in Figure 4.1 where a central silicon (Si) atom is bonded to four methyl (CH₃) groups. The most important physical and chemical characteristics of the TMS precursor are summarised in Table 4.1.

TMS precursor is a stable, slightly irritable, in-toxic, colourless liquid, volatile at room temperature. The volatility is due to its high vapour pressure which considered as an advantage because high vapour flows can be obtained without the need of heating apparatus [87]. In the lab, the precursor is stored in a glass container. It is also common to be stored in a stainless steel or plastic container. The precursor is

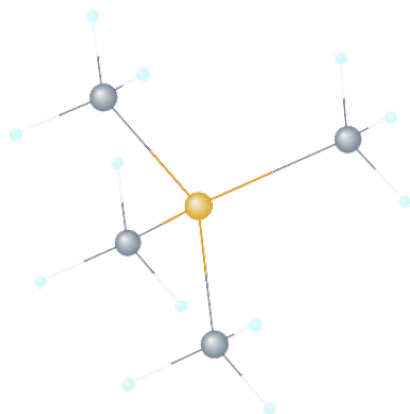


Figure 4.1: Tetramethylsilane molecular structure [85].

Table 4.1: Physical and chemical properties of TMS [86].

Molecular Formula	Si(CH ₃) ₄	Physical State _(at 20°C)	Liquid
Molecular Weight	88.2 g/mol	Vapor Pressure _(at 20°C)	589 Torr
Stability	Stable	Density _(at 20°C)	0.648 g/cm ³
Use of Standard MFC	Yes	Viscosity _(at 20°C)	2.42 N/s.m ²
Pyrophoricity	No	Melting Point	-99°C
Flammability	Yes	Boiling Point	26-28°C
Toxicity	No	Flash Point	-27°C

placed close to the reactor to avoid leakage and minimise the gas line cost. Tetramethylsilane is obtained from (FluroChem Ltd, UK) with a purity of ($\geq 99.99\%$). The tetramethylsilane stock is deposited in the refrigerator at 5 degrees in the lab. The initial experiments TMS was used as silicon precursor in different plasma condition to observe in which measure the atomic species can be integrated into stable and homogeneous films on textured silicon solar cells with reasonable deposition rate and optical properties. The coating conditions of the solar cells with the TMS precursor are summarised in Table 4.2.

Table 4.2: Summary of the coating conditions for solar cells using TMS precursor.

Coating Conditions	X ₁	X ₂	X ₃	X ₄	X ₅	X ₆	X ₇	X ₈	X ₉
DC Bias (volts)	300	300	300	200	200	200	100	100	100
TMS Flow Rate (cm ³ /min)	25	25	25	25	25	25	25	25	25
Time (minutes)	4	10	15	4	10	15	4	10	15

In all of the coatings the TMS flow rate is fixed at 25 cm³/min. This deposition rate is appropriate for maintaining the plasma environment in the coating chamber during the deposition process.

The initial experiments showed three different patterns according to the bias voltage of the coating conditions.

The first pattern is obtained at a bias voltage of 300V. Solar cells coated at different deposition times of 4, 8 and 10 minutes resulted in a rainbow-like coating with the a poor homogeneity of deposited layers. An example of the obtained coating is representing in (A) in Figure 4.2 which corresponds to the coating condition of X₁.

Decreasing the DC bias voltage to 200V improved the homogeneity of the deposited layers. However, solar cells coated at DC bias voltage of 200V showed a pink colour with huge green spots around the edges of the solar cell for different deposition times. A photograph showing an example of this pattern is shown in (B) in Figure 4.2 which represents the coating conditions of X₅.

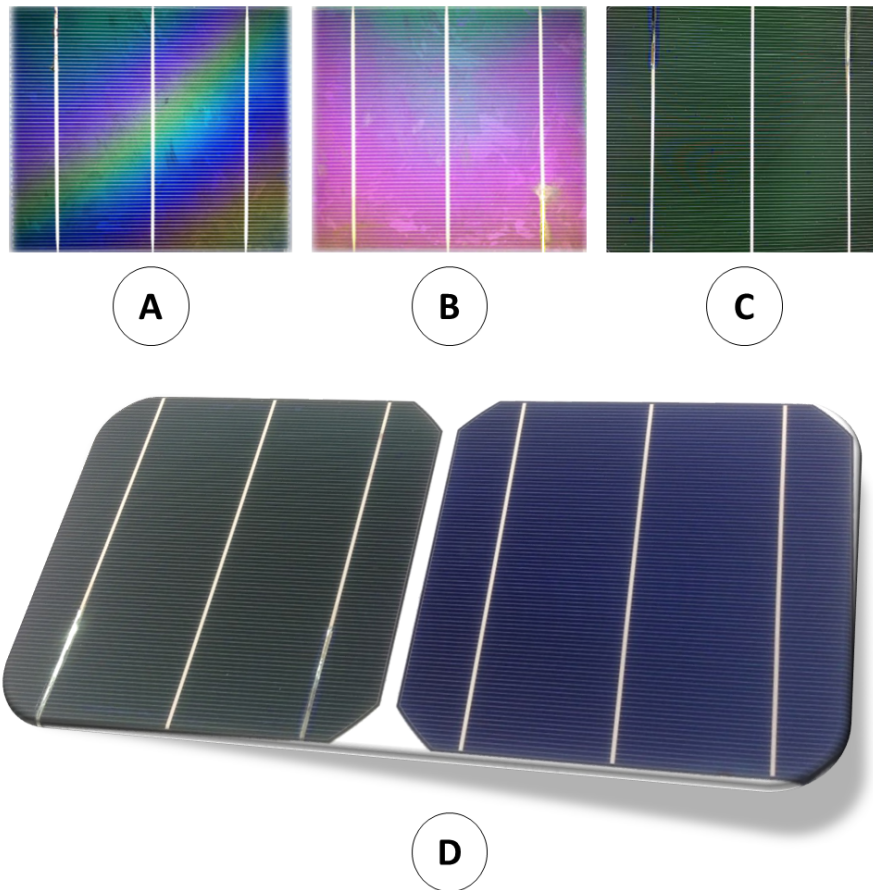


Figure 4.2: Photographs of the TMS-coated solar cells at different coating conditions.

(A) displays an example of the obtained coated solar cell which corresponds to the coating condition of X_1 , (B) shows the solar cell obtained using the coating conditions of X_5 , (C) presents the obtained coated solar cell using coating conditions of X_7 and (D) shows a solar cell before coating (blue) and a coated solar cell using coating conditions of X_9 .

At 100V DC bias, the deposited layer showed a good uniformity on the entire of the solar cells with a green colour as shown in (C) which represents the coating conditions of X₇. The uniformity was enhanced by increasing the deposition time from 5 minutes to 15 minutes.

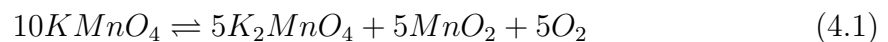
According to the results, it can be concluded that the most influencing parameter for obtaining a homogeneous layer using TMS is the bias voltage and then the deposition time for a deposition rate of 25 cm³/min. It was found that the PECVD conditions of DC bias voltage of 100V, TMS flow rate of 25 cm³/min and deposition time of 15 minutes yielded the best homogeneous layer for silicon solar cells as shown in (D) in Figure 4.2. Therefore, coating conditions of X₉ were used in the silicon oxide study.

4.3.2 Oxidation Agent

Silicon films were oxidised during the coating process, oxidation of the films was carried out by introduced potassium permanganate in the coating chamber.

Potassium permanganate is obtained from (Fisher Scientific, UK). It is an inorganic compound with chemical formula KMnO₄ with a purity of (≥99.0%). Potassium permanganate is a strong oxidising agent where the thermal decomposition of the material forms a mixture of potassium permanganate, manganese dioxide and release oxygen [88].

The temperature inside the vacuum chamber is about 200 °C allowing the thermal decomposition of potassium permanganate which could be represented in the following scheme:



4.3.3 PECVD Coating Process

Experiments were carried out on mono-crystalline silicon solar cells model XS156B3 (Motech Industries, Taiwan) with a dimension of $156 \times 156 \text{ mm}^2$. Silicon oxide films were deposited on top of commercial solar cells to form a single and double ARC layer as shown in the schematic in Figure 4.3.

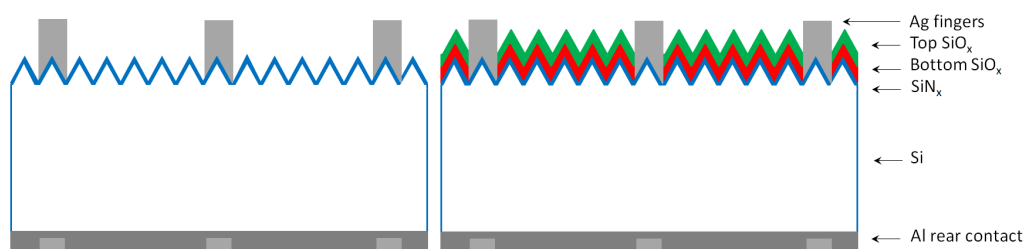


Figure 4.3: The schematic structures of commercial solar cell before and after coating with a single and double layer of silicon oxide.

Deposition of silicon oxide films on silicon solar cells was conducted using a 13.6 MHz rf powered, capacitively coupled, PECVD process (also referred to as Plasma Assisted Chemical Vapour Deposition, PACVD). More details on the system configurations can be found in [89]. A schematic of the used PECVD reactor is shown in Figure 4.4.

Prior to deposition, cells were cleaned using an Isopropyl alcohol solution. The cleaning continues inside the PECVD chamber by argon ion bombardment. The argon flow rate was $30 \text{ cm}^3/\text{min}$ for 5 minutes with a 100V DC bias for each experiment. The argon treatment displaces impurities on the substrates through energetic argon ion bombardment. The solar cells were placed on an electrode, whose configuration was designed to provide a uniform plasma environment and to ensure good film uniformity across the entire area of the cell. Solar cells were introduced into the process chamber of the PECVD reactor and reaction species are ionized at radio frequency of 13.56 MHz. The precursor used for the deposition of silicon is TMS. The TMS entering the chamber is ionized and strikes the substrate placed on a supporting cathode table.

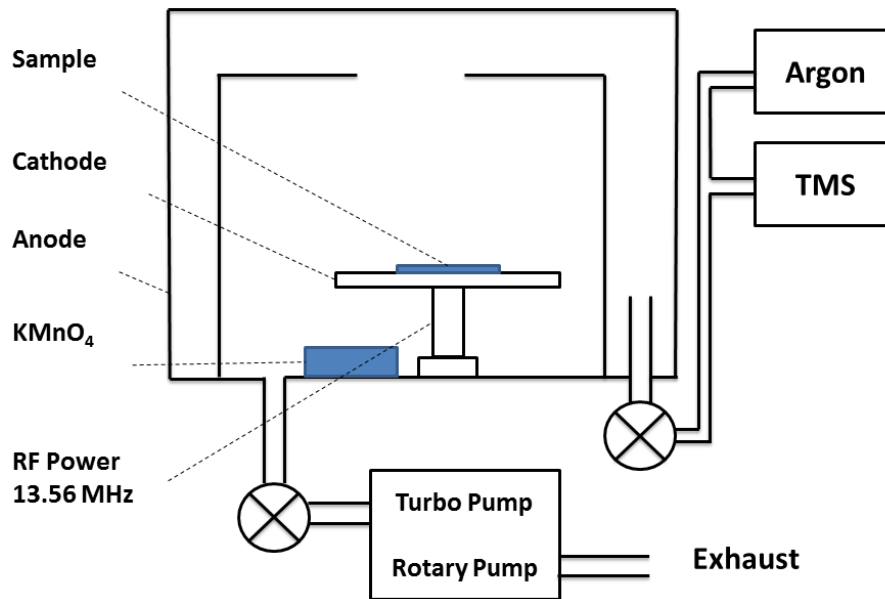


Figure 4.4: Schematic of the PECVD reactor and the substrate positioning.

The flow of the process gas is controlled and monitored using mass flow controllers;

Table 4.3: Summary of the coating conditions for solar cells with a single anti-reflection layer of silicon oxide.

Coating Conditions	S ₁	S ₂	S ₃	S ₄	S ₅	S ₆
DC Bias (volts)	100	100	100	100	100	100
TMS Flow Rate (cm ³ /min)	25	25	25	25	25	25
Time (minutes)	15	15	15	15	15	15
KMnO ₄ Mass (grams)	5	10	20	30	40	50

and the chamber pressure maintained at 10^{-4} bar is controlled and monitored using a capacitance manometer and pressure control unit.

One mono-crystalline cell was placed inside the chamber for each experiment. The coating parameters are voltage and the flow of TMS. Those parameters remained constant for each experiment while the mass of potassium permanganate was varied for each experiment. Potassium permanganate was placed in a 10 cm glass Petri dish and the crystalline powder was distributed evenly to ensure good exposure to the plasma field. The coating conditions for single layer deposition of silicon oxide are summarised in Table 4.3.

Table 4.4: Summary of the coating conditions for solar cells with a double anti-reflection layer of silicon oxide.

Coating Conditions	D ₁	D ₂	D ₃
DC Bias (volts)	100	100	100
TMS Flow Rate (cm ³ /min)	25	25	25
Time (minutes)	15	15	15
KMnO ₄ Mass (grams)	10	20	30

For double ARC with silicon oxide films, a quarter of the solar cell was covered with an aluminium mask and coated with same coating conditions as S₃ to form the first layer. The second layer is formed on top of S₃ layer with appropriate coverage with the aluminium mask. The coating conditions for the top layer of the solar cells coated with double ARC layers are summarised in Table 4.4.

4.4 Results and Discussion

For the purpose of proving the enhanced photon absorption effect via I-V curves, solar cells were illuminated with UV light, high energy excitation (UV-Blue) photons, I-V measurements were carried out under the UV light intensity of 46.1 W/m^2 where this value represents the amount of UV light in the standard AM 1.5 spectrum between 280 and 400 nm [8, 90].

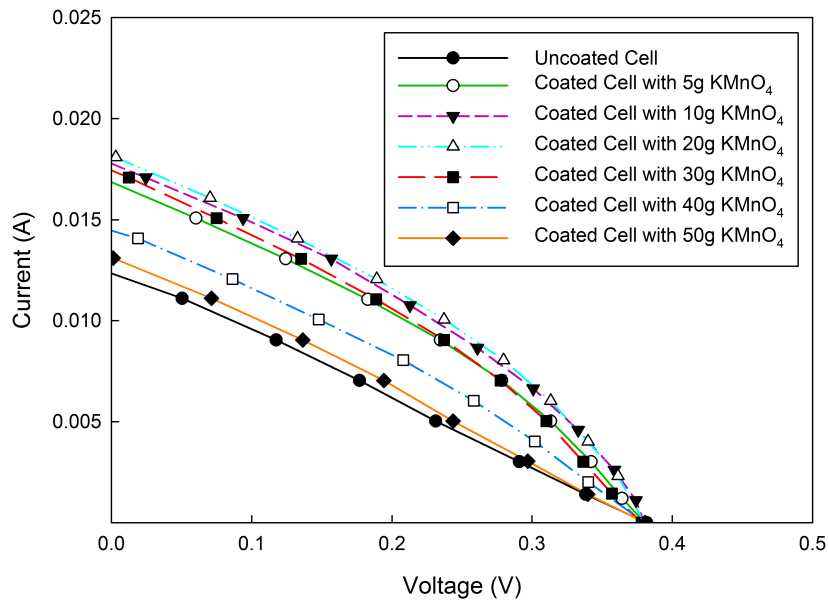


Figure 4.5: I-V curves of solar cells before and after coating with single layer of silicon oxide film under UV light illumination.

Figure 4.5 shows I-V curves of the uncoated and coated silicon solar cells oxidised with (5, 10, 20, 30, 40, 50) g KMnO_4 . It can be seen from Figure 4.5, the following best results were obtained in the case of the coated solar cell oxidised with 20 g KMnO_4 . It was found that $I_{sc}=19.1 \text{ mA}$ and $V_{oc}=381 \text{ mV}$ in comparison with uncoated cell with $I_{sc}=12.4 \text{ mA}$ and $V_{oc}=381 \text{ mV}$. According to these values of the short circuit current and open circuit voltage under UV light illumination, the coated cell shows higher I_{sc} than the uncoated cell. This improvement in the current can be ascribed to absorption within Si nanoparticles embedded in the oxide matrix [91].

Details of the electrical characteristics of the coated solar cells under UV light illumination are summarised in Table 4.5. It can be seen that the electrical conversion

Table 4.5: Electrical characteristics of the uncoated (S_0) and coated cells ($S_1, S_2, S_3, S_4, S_5, S_6$) under UV light illumination.

Sample	I_{sc} mA	V_{oc} mV	P_{max} W	FF –	η %	$R_{(200-400)nm}$ %
Uncoated S_0	0.0124	0.381	0.0012	0.26	3.36	21.386
S_1	0.0171	0.381	0.0021	0.33	5.80	8.212
Uncoated S_0	0.0120	0.381	0.0013	0.26	3.24	21.166
S_2	0.0181	0.382	0.0024	0.34	6.34	8.291
Uncoated S_0	0.0131	0.380	0.0013	0.26	3.53	21.011
S_3	0.0191	0.381	0.0024	0.33	6.48	8.017
Uncoated S_0	0.0129	0.381	0.0012	0.26	3.45	21.367
S_4	0.0188	0.380	0.0020	0.29	5.59	11.918
Uncoated S_0	0.0119	0.380	0.0013	0.26	3.27	21.717
S_5	0.0151	0.381	0.0017	0.29	4.50	13.647
Uncoated S_0	0.0117	0.381	0.0012	0.26	3.22	21.716
S_6	0.0141	0.381	0.0014	0.25	3.77	14.177

efficiency of the coated cells oxidised with (5, 10, 20, 30, 40, 50) g of the oxidizing agent have higher electrical conversion efficiency as a result of an increase in the short circuit current. The conversion efficiency of the coated cells increases with the increased mass of the potassium permanganate peaking at 20 g mass of the oxidizing agent then the efficiency starts to drop with increased mass of potassium permanganate. Also, the average reflectance of these cells in the UV range is shown in Table 4.5. Also, the reflection values of the cells in the UV band correspond to the conversion efficiency performance of the cells under UV illumination where the increasing values of the reflection in the UV range correspond to the decreasing values of the conversion efficiency. This increase in the conversion efficiency can be ascribed to the coatings generates enhanced overall photon absorption effects where the lower the reflectance values result in more photons being absorbed and converted into visible light wavelengths where the solar cells have a better response.

Figure 4.6 shows the reflection spectra of the uncoated and coated cells with

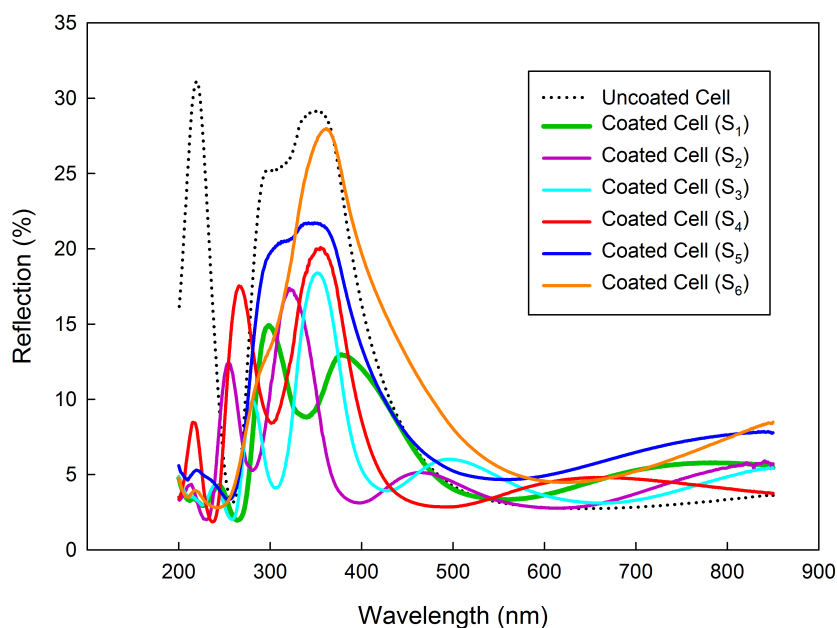


Figure 4.6: Reflection spectra of the coated and uncoated solar cells with single anti-reflection layer of silicon oxide.

silicon films oxidised with (10, 20, 30, 40, 50) g of potassium permanganate. It can be seen that solar cells coated with a single layer of silicon oxide have a lower reflectance in the range of (200-400) nm in comparison with the uncoated cell. Also, it can be seen from the figure that the reflectance in the UV range increases with the increased mass of the oxidising agent. Amorphous silicon oxide coating is transparent in the measured wavelength range, and the reflection of the silicon oxide film is dependent on the thickness. With the increase in the thickness of the coating layer, the reflection changes correspondingly. The effect of the thickness on the reflection spectra in the UV range is indicated by Aguilar et al. where the increase in the reflection corresponds to the increased thickness of the silicon oxide film [92].

Figure 4.7 shows the electrical conversion efficiency of the solar cells against the mass of the KMnO_4 under ultraviolet and visible light illumination. Under visible light illumination, it can be seen from the graph that the efficiency increases with the increasing value of the KMnO_4 until it reaches an optimum value then it starts to decrease. The change in the optical properties and electrical characteristics is

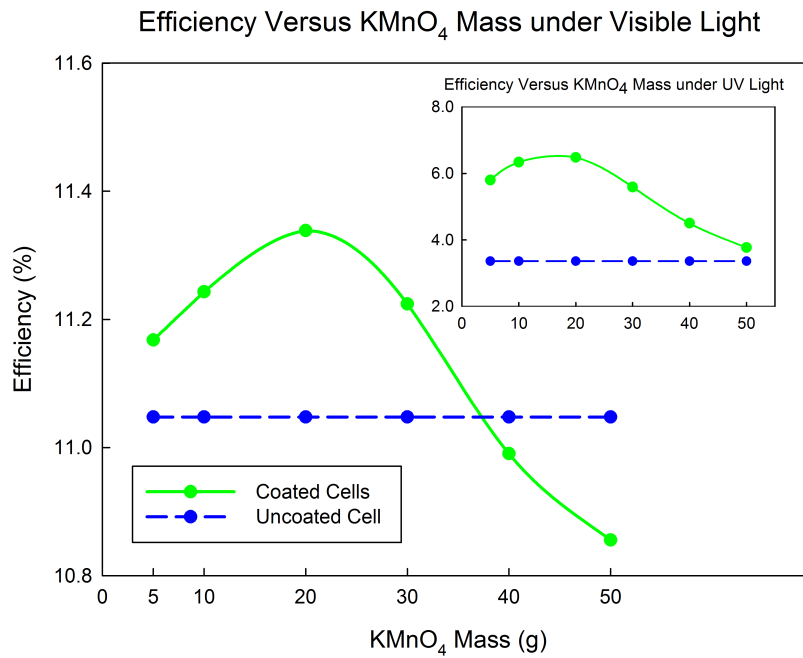


Figure 4.7: Efficiency versus KMnO_4 mass under visible and ultraviolet light illumination.

due to an increase in the mass of KMnO_4 introduced in the coating chamber which results in increasing the amount of oxygen released due to thermal decomposition of KMnO_4 . Since the coating parameters were similar for all the coated cells, it means that the depth of oxygen diffusion within the silicon layer affects the electrical conversion efficiency of the cell significantly. The electrical characteristics of the solar cells under visible light illumination are summarised in Table 4.6.

Under UV light illumination, the conversion efficiency curve of the coated cells against the change in mass of KMnO_4 shows a similar tendency compared to the conversion efficiency curve under visible light illumination. However, all the coated solar cells show higher conversion efficiency in comparison with the uncoated solar cell as a result of having a better response to the UV after the coating process.

Figure 4.8 shows reflection spectra of the uncoated (D_0) and coated solar cells with double layers of silicon oxide (D_1 , D_2 , D_3) where double layers in this thesis refers to solar cell coated twice with the mentioned parameters as a possible way to

Table 4.6: Electrical characteristics of the uncoated (S_0) and coated cells ($S_1, S_2, S_3, S_4, S_5, S_6$) under visible light illumination.

Sample label	I_{sc} A	V_{oc} V	P_{mp} W	FF –	η %
Uncoated S_0	0.277	0.547	0.0888	0.59	11.05
S_1	0.279	0.547	0.0898	0.59	11.17
Uncoated S_0	0.277	0.547	0.0896	0.59	11.07
S_2	0.285	0.547	0.0904	0.58	11.24
Uncoated S_0	0.277	0.547	0.0895	0.59	11.06
S_3	0.287	0.547	0.0911	0.58	11.34
Uncoated S_0	0.278	0.547	0.0896	0.59	11.08
S_4	0.285	0.547	0.0902	0.58	11.22
Uncoated S_0	0.278	0.547	0.0893	0.59	11.04
S_5	0.275	0.547	0.0883	0.59	10.99
Uncoated S_0	0.278	0.547	0.0892	0.59	11.03
S_6	0.270	0.547	0.0873	0.59	10.86

increase the thickness of the layer. It can be seen that only the solar cell coated with double anti-reflection layer (D_1) presents a lower reflection in comparison with single anti-reflection (S_1). Solar cell coated with D_1 showed a light green and D_2 yellow and D_3 magenta colour for the naked eye as shown in Figure 4.9.

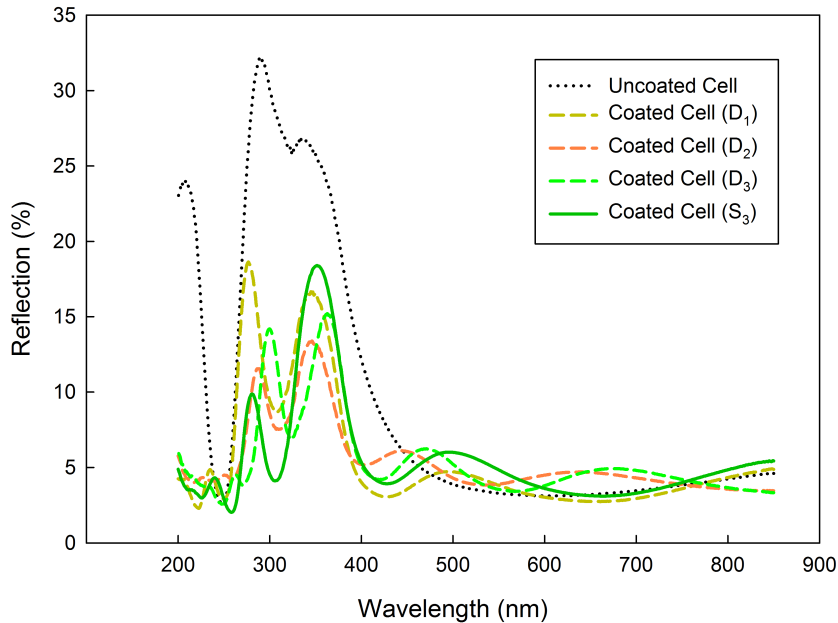


Figure 4.8: Reflection spectra of coated cells with double anti-reflection coating.

The electrical characteristics of the solar cells coated with double anti-reflection

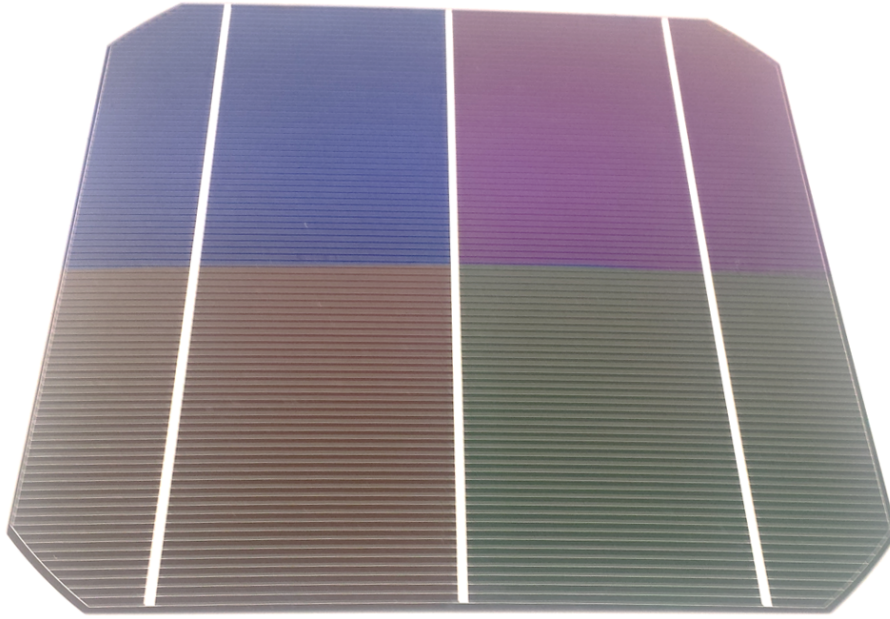


Figure 4.9: Photographs of mono-crystalline silicon solar cell coated with double layers of silicon oxide.

layers are summarised in Table 4.7. It can be seen from the Table 4.7 that the reflection spectra corresponds to the electrical characteristics of the solar cells where D_1 shows an improved electrical characteristic to S_1 while the other solar cells coated with double ARC layers showed a lower conversion efficiency in comparison with the solar cell at maximum enhancement obtained with single ARC layer S_1 .

Table 4.7: Electrical characteristics of the uncoated (D_0) and coated solar cells (D_1 , D_2 , D_3) under visible light illumination at the illuminated surface area of 8.544 cm^2 , 1000 W/m^2 and $25 \text{ }^\circ\text{C}$.

Sample label	I_{sc} mA	V_{oc} V	P_{mp} W	FF –	η %	Colour –
D_0	277	0.547	0.0888	0.59	11.05	Blue
D_1	287.7	0.547	0.0913	0.58	11.36	Magenta
D_2	284.6	0.547	0.0902	0.58	11.23	Green
D_3	283.6	0.547	0.0898	0.58	11.18	Yellow

Figure 4.10 shows I-V and P-V curves of the uncoated and coated cell with a double anti-reflection layer. It can be seen from the curve that the improvement in the electrical performance of the solar cell after the coating is due to a better exploit of the light which can be seen as an increase in the short circuit current. However, the

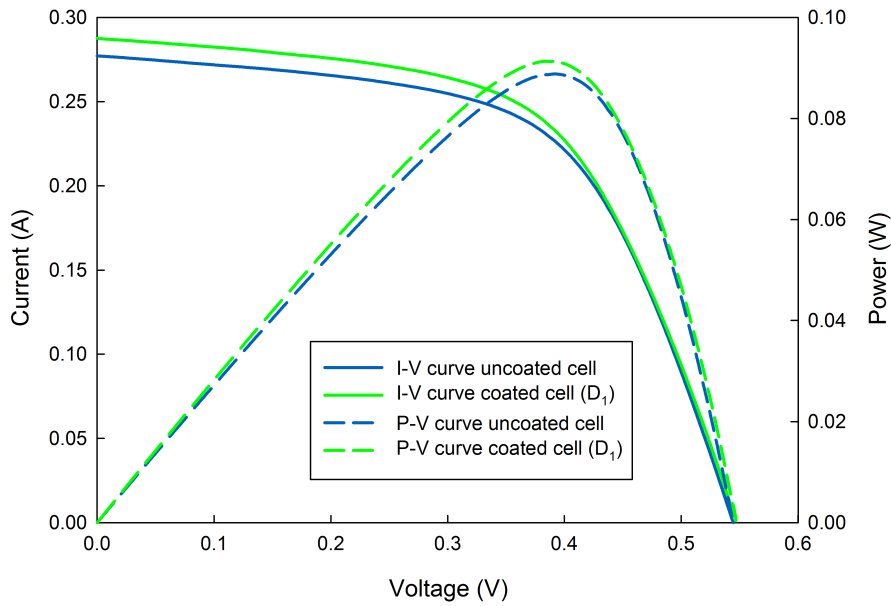


Figure 4.10: I-V and P-V curves of the coated cell at the maximum enhancement obtained under visible light illumination at the illuminated surface area of 8.544 cm^2 , 1000 W/m^2 and $25 \text{ }^\circ\text{C}$.

open circuit voltage remained constant before and after the process. No increase was observed in the open circuit voltage. This corresponds to the concept of the additional converter layer which does not influence the energy gap of the silicon-based solar cell [91]. Moreover, no reduction in the open circuit voltage means that low-temperature PECVD process did not cause damage to the solar cell surface in which can happen in high-temperature deposition techniques [93].

Figure 4.11 shows the transmission and absorption spectra of the anti-reflection coatings for the silicon solar cell with optimum electrical characteristics obtained for single (S_3) and double (D_2) layers of silicon oxide. It can be seen from the absorption spectra, that double anti-reflection layer of silicon oxide has higher absorption from the single anti-reflection layer over the UV light band of the spectrum. This tendency can be ascribed to the increased thickness of the silicon oxide layer where thicker layers of silicon oxide absorb more light [92]. However, in the visible light range, a decrease in the absorption of the double anti-reflection layer in comparison to the single one can be observed.

From the transmission spectra, it can be seen that the obtained results correspond to the absorption ones. The increase in the transmission in the visible part of the spectrum for a double anti-reflection layer of the silicon oxide in comparison to the single anti-reflection layer can be ascribed to the light interference occurring in the double layer coating. Light interference can be referred to the graded index in the design of the double anti-reflection layer where the layer with the greater refractive index is placed on the bottom of double anti-reflective design and layer with the lower refractive index is built on top of the first layer. The double anti-reflection design of (D₂) consists of the bottom layer of S₃ which is oxidised with 20 g of KMnO₄ during the deposition process, and the top layer of silicon is oxidised with 10 g of KMnO₄.

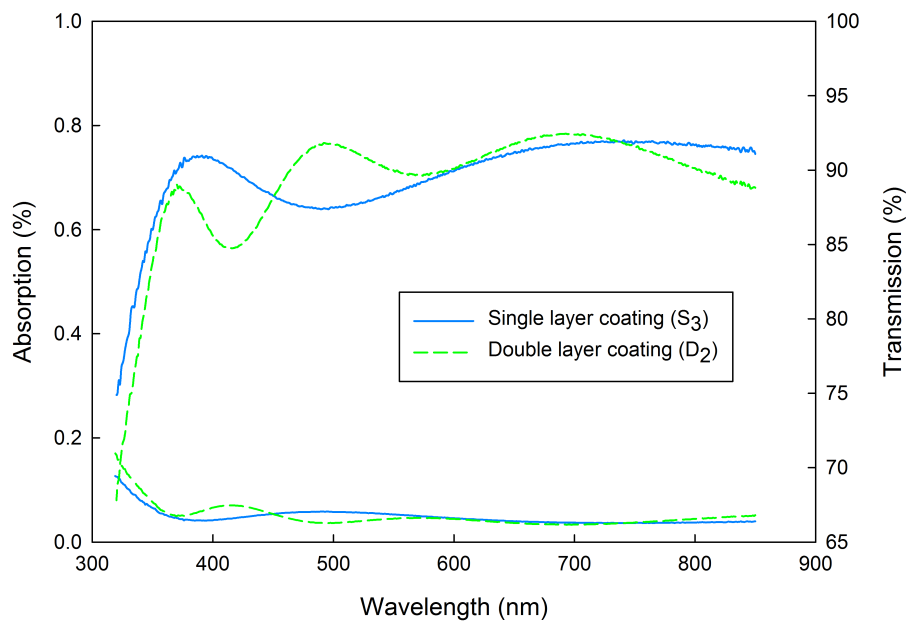


Figure 4.11: Absorption and reflection spectra of the single and double anti-reflection layers for solar cells with optimum enhancement obtained.

Figure 4.12 shows the chemical composition of the surface of the uncoated and coated cells. It can be seen for the uncoated solar cell, the presence of the elements N and Si because the commercial solar cells are coated with an anti-reflection layer of silicon nitride. However, the coated cell shows the presence of additional elements of C and O where carbon is deposited on the surface due to the TMS precursor during

PECVD process due in which the decomposition of TMS is viewed as breakage of methyl groups [82] and the presence of oxygen is because of the use of the oxidizing agent, potassium permanganate. The electrical conversion efficiency could be further enhanced by optimising the PECVD deposition process to lower the impurity content of silicon oxide film that is incorporated in the compound such as carbon during the PECVD processes. It is important to mention that since the potassium permanganate used in as an oxidation agent, other impurities could be incorporated in the Silicon oxide such as K and Mn. These impurities may fall off the range of EDAX analysis.

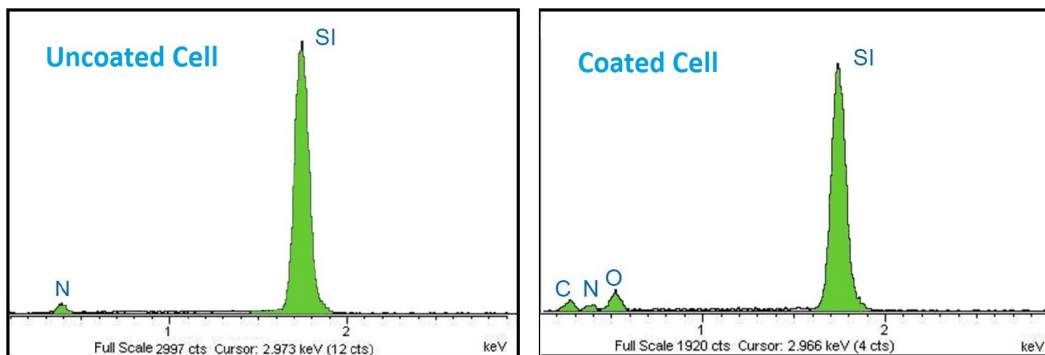


Figure 4.12: EDX spectrum of the coated and uncoated solar cell.

Results of EDX spectra of three silicon solar cells coated with single anti-reflection coating layer oxidized with (10, 20, 30) g of the oxidising agent are shown in Table 4.8. Three different areas (x_1 , x_2 , x_3) of interests were examined on each sample and the mean for these samples is presented. It can be seen from the table that the increase in the average values of the oxygen on cell surface corresponds to the increase in the amount of potassium permanganate in the coating chamber. Also, the decreasing values of Nitride in the samples with increased mass of potassium permanganate can be ascribed to an increase in the thickness of the anti-reflection layer.

Table 4.8: Values of the EDX spectra of the coated silicon solar cells (S_2 , S_3 , S_4).

Sample	C	N	O	Si	Total	
10 mg	x_1	24	8.47	7.52	60.01	100
	x_2	24.13	8.38	7.31	60.18	100
	x_3	24.10	8.24	7.44	60.22	100
Mean	24.08	8.36	7.42	60.14		
Standard deviation	0.07	0.12	0.11	0.11		
20 mg	x_1	23.64	7.43	8.49	60.44	100
	x_2	23.69	7.64	8.04	60.63	100
	x_3	23.43	7.33	8.42	60.82	100
Mean	23.59	7.47	8.32	60.63	100	
Standard deviation	0.14	0.16	0.24	0.19		
30 mg	x_1	23.56	6.89	8.57	60.98	100
	x_2	23.32	6.66	8.90	61.12	100
	x_3	23.15	6.91	8.63	61.31	100
Mean	23.34	6.82	8.70	61.14	100	
Standard deviation	0.21	0.14	0.18	0.17		

All results shown in the table are in weight %

4.5 Summary

Silicon solar cells coated with silicon oxide films can reduce reflection from the silicon surface and contribute to the increase of the conversion energy of the solar cells in one hand while the variety of colours obtained in this study can be of great importance for building integrated photovoltaic application in another hand.

This study demonstrates the potential for using silicon oxide films produced by low-temperature PECVD using TMS as a silicon precursor and $KMnO_4$ oxidising agent for efficiency enhancement of solar cells at low manufacturing cost.

With optimised oxygen diffusion in the silicon films for solar cells coated with a single layer of silicon oxide can yield a competitive electrical conversion efficiency in comparison to a double layer of silicon oxide coating. Also, double ARC is more flexible to modulate colours while maintaining good passivation quality. Various coloured mono-crystalline silicon solar cells were obtained by depositing an additional layer of silicon oxide with better performance can be achieved in comparison to uncoated cells

where the solar cells showed a relative enhancement of about 3% in the conversion efficiency. The conversion efficiency of coloured solar cells shows a little variation (+0.1% to 0.7%) compared to the reference cells with standard single anti-reflection layer of silicon nitride. A variety of obtained colours can find an application in the industry such as BIPV despite the trade-off between efficiency and the colour of the solar cell when the aesthetic visibility for BIPV is preferable to the conversion efficiency of the solar cells.

Chapter 5

Titanium Oxide for PV Solar Cell

In this chapter, silicon-based photovoltaic solar cells were coated with oxide layers for a single layer of titanium oxide and double layers of silicon oxide and titanium oxide anti-reflective coatings. This research presents an experimental study of titanium thin films deposited by either RF or DC magnetron sputtering system at room temperature and oxidised by means of thermal or plasma annealing process.

The optical properties of titanium films and their application as an ARC for mono-crystalline silicon solar cells are also studied. Optical energy bandgap of the deposited films was investigated and compared to a known structure of titanium oxide produced in the lab. Optical and electrical analysis showed that RF sputtering is more appropriate over DC sputtering for the solar cell. Moreover, thermal annealing showed a better suitability for solar cell coating over the plasma annealing.

A study of titanium oxide/silicon oxide stack as an anti-reflection coating is also presented in this chapter. Solar cells coated with a silicon oxide and titanium stack showed a relative enhancement of 1.6% (from 12.057% to 12.26%) in the conversion efficiency of the crystalline silicon solar cells.

5.1 Introduction

Titanium dioxide thin films is one of the transition-metal oxides which has been studied extensively in the last two decades due to its unique optical and dielectric properties which make TiO_2 thin films an attractive option for anti-reflection coating in the photovoltaic industry. The use of TiO_2 thin films provides many advantages such as exhibiting excellent chemical resistance to the majority of the chemicals used in PV industry [94], ease of deposition and low fabrication cost [95], and their optimal refractive index is for solar encapsulated silicon solar cells [96].

In this chapter, the effects of thin films of silicon oxide and titanium oxide as single and double anti-reflection coating are studied. Titanium and silicon oxide stack allow a design of low-high refractive index design for solar cells. Silicon oxide possesses a lower refractive index than titanium oxide, good passivation and scratch resistance properties and shows chemical stability at elevated temperatures of (350-800) $^\circ\text{C}$ [97].

A variety of techniques are being used to deposit titanium oxide films, including sputtering [98], sol-gel [99], screen printing [100], Atomic Layer Deposition (ALD) [101], Chemical Spray Pyrolysis (CSP) [102], Chemical Vapour Deposition (CVD) [103] and Pulsed Laser Deposition (PLD)[96].

The sol-gel method is an efficient cost effective option for titanium coating for solar cells, but the thickness is not precisely controlled using this technique [104, 105]. The need for high vacuum in CVD process makes this technique more challenging for mass production of PV silicon solar cells [106].

Most of the titanium deposition techniques require heating the substrate during or after deposition of the material where the samples could be annealed to a high temperature for an extended period. Heat treatment at high temperatures in silicon solar cells processes could introduce defects which in turns could act as recombination centres for charge carrier in the solar cell. Moreover, this heat treatment could change

the intended compositional distribution of solar cells [107, 108].

Titanium dioxide can exist in three different crystalline polymorphs forms: rutile (tetragonal), anatase (tetragonal) and brookite (orthorhombic). Each phase of the titanium possesses different unique properties. Rutile, the most thermodynamically stable phase of titania, is denser than anatase and brookite). Each form of titania is characterised with different optical energy bandgap; anatase has the highest value of 3.2 eV and rutile has the value of 3 eV. Therefore, thin films with different ratios of the titania phases can be characterised by various optical and electrical properties. Both anatase and rutile are stable crystalline phases of titania, anatase phase can be of keen interest for photovoltaics where titanium thin film containing anatase phase has a better transmittance than titanium thin film which is pure rutile phase, even if the rutile film is much thinner than the anatase film [109].

In addition to the excellent optical properties exhibited by the anatase crystal structure of titania, anatase phase is preferred in PV applications as this phase occurs at a relatively low temperature that is suitable for PV cell manufacturing processes [110]. Typically, anatase phase is achieved at deposition temperatures above 350 °C and rutile at temperatures above 800 °C while films deposited at temperatures below 300 °C are primarily amorphous [94].

Plasma-assisted oxidation of metal films shows considerable potential, especially taking into consideration the temperature requirement, in comparison to other conventional annealing techniques. Oxidation performed in the presence of an electric field, and low temperatures not only enhances the directionality of oxidation but also reduces interdiffusion of thin films and defect generation compared with high-temperature thermally driven processes [111].

5.2 Related work

Researchers demonstrated the potential of titania thin films to improve the conversion efficiency and reduce the production costs of commercially produced silicon solar cells using a variety of deposition techniques. The obtained improvement is due to reducing reflection and improving the light generated current by TiO_2 anti-reflection coating [96, 106, 112].

The conversion efficiency of titanium coated crystalline silicon solar cells can be further improved by depositing an additional layer of silicon oxide to form a silicon oxide/titanium oxide stack. This design could allow the design of low-high refractive index for solar cell and consequently a broader improvement in the optical performance of the anti-reflection layer. Lien et al. showed the effect of a single layer of titanium and a stack of silicon oxide/titanium oxide on non-textured monocrystalline silicon solar gel using sol-gel deposition technique. The author obtained an absolute enhancement of 3% for solar cells coated with titanium and a further improvement of 0.5% for solar cells coated with a stack of silicon oxide/titanium oxide.[113]

Reports on the optical studies of titanium oxide films deposited by DC or RF sputtering demonstrated the potential of using the techniques for solar cell application [114, 115, 116]. However, the reported literature lacks the application of these films into PV solar cells. Khuram et al. studied the effects of a single layer of titanium oxide fabricated by RF sputtering and the effects of a double layer of silicon oxide and titanium oxide for the non-textured surface of the mono-crystalline silicon solar cell. The author obtained an absolute enhancement in the conversion efficiency by 1.7% and 3.4% for single and double layer coating respectively in comparison to the as-grown silicon solar cell. The obtained improvement was as a result of an increase in the short-circuit current due to decreased reflection losses through the addition of anti-reflection coating films [112, 117].

5.3 Experimental Method

5.3.1 Deposition of Thin Films

The first step of the experiment is to coat the solar cells with thin films of titanium using Qbox sputtering system. A schematic of the Obox sputtering system is shown in Figure 5.1. The coating process starts with loading the solar cell and quartz slide into the chamber. Substrates are mounted on the substrate holder facing down then the stage is rotated by slowly turning the speed adjust knob on the rotation controller to the desired level in order to check the substrates are correctly placed on the substrate holder. It is important to check visually that the sample rotation is smooth and level before proceeding to the next step.

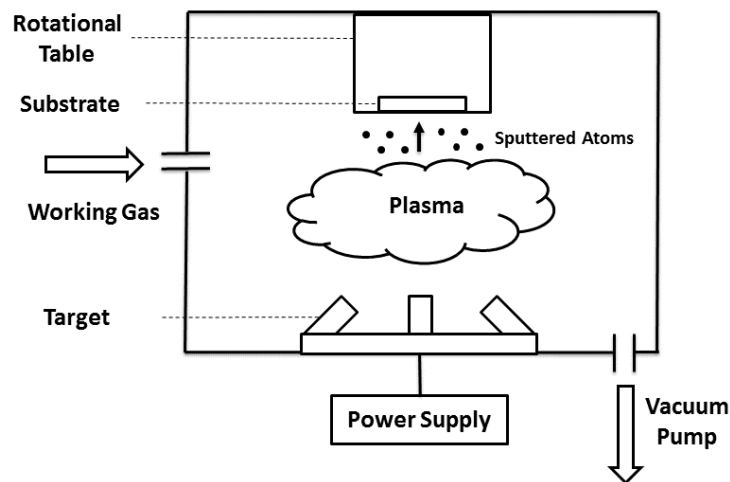


Figure 5.1: Schematic of the Qbox sputtering system.

After loading the samples, the coating chamber is pumped down to a high vacuum using a rotary pump. Base pressure is set to 2×10^{-3} mbar for DC sputtering and 1×10^{-3} mbar for RF sputtering during the course of the experiments. These pressures can be reached within 25-30 minutes for a clean system. If the system is left open to the atmosphere even for short period of time i.e. 10 min, the pumping time will increase significantly.

The deposition of titanium films may be performed once the required vacuum level is reached. The deposition of the titanium on the substrate was carried out at room temperature without heating the substrate. A titanium disc of 99.99% purity with 50 mm diameter and 5 mm thickness was used as the target. Argon was used as the default working gas with flow rates of 30 sccm and 15 sccm for RF and DC sputtering respectively. These conditions were considered as an optimal condition for deposition as in the case of using lower flow rates; the plasma will not be sustained. The working pressure in the chamber can be controlled by setting the flow level of Argon. After setting the working pressure, the deposition can be started. The deposition can be controlled by the pressure and the applied power.

Table 5.1: The deposition conditions of titanium films.

No.	Cathode Power (W)	Sputtering Pressure Set (mbar)	Sputtering Pressure Actual (mbar)	Thickness Set (nm)	Thickness Actual (nm)	Deposition Rate (Å°/sec)	Argon Flow (sccm)	Room Temperature (°C)	Table Speed (rpm)
DC Power Supply									
T _{DC1}	100	2x10 ⁻³	2.42x10 ⁻³	4	4.058	0.31	15	21	10
T _{DC2}	100	2x10 ⁻³	2.24x10 ⁻³	6	5.993	0.27	15	21	10
T _{DC3}	100	2x10 ⁻³	2.24x10 ⁻³	8	8.180	0.36	15	21.3	10
T _{DC4}	100	2x10 ⁻³	2.09x10 ⁻³	4	4.403	0.37	15	19.7	10
T _{DC5}	100	2x10 ⁻³	2.44x10 ⁻³	4	4.170	0.41	15	19.8	10
RF Power Supply									
T _{RF1}	300	1x10 ⁻³	1.90x10 ⁻³	4	4.354	0.48	30	21.7	10
T _{RF2}	300	1x10 ⁻³	1.90x10 ⁻³	8	8.366	0.47	30	18.5	10
T _{RF3}	300	1x10 ⁻³	1.92x10 ⁻³	6	5.920	0.48	30	19.7	10
T _{RF4}	300	1x10 ⁻³	1.94x10 ⁻³	4	4.258	0.48	30	19.9	10
T _{RF5}	300	1x10 ⁻³	1.97x10 ⁻³	4	4.170	0.46	30	19.2	10
RF Power Supply									
TS ₁	300	1x10 ⁻³	2.03x10 ⁻³	4	4.14	0.45	30	20.1	10
TS ₂	300	1x10 ⁻³	2.05x10 ⁻³	4	4.08	0.45	30	20.3	10
TS ₃	300	1x10 ⁻³	2.09x10 ⁻³	4	4.11	0.46	30	20.9	10

Plasma is created in the chamber by applying the power. The glowing plasma can be used to clean the substrate which is immersed in plasma at this stage. The deposition of the films is monitored using a Quartz Crystal deposition Monitor (QCM) is often integrated into the system for calibration purposes. The QCM can be placed directly below the substrate for calibration. Visual inspection of the plasma can give

a good indication regarding argon ionisation level in which a pink appearing colour of plasma means that the ionisation level of plasma is low whereas the blue appearing colour occurs at high ionised plasma.

The deposition does not start before the bias is applied to the target. The system is left to run for few minutes to precondition the target before the growth on the substrate start. The growth of titanium film is initialised by opening the shutter and leaving it for the time needed to grow the desired thickness of the material. A list of the details of the coating conditions is summarised in Table 5.1.

Once the deposition is finished, almost reaching the desired thickness, the shutter is closed, and the power supply is switched off, and Mass Flow Controllers MFCs are set to zero. Then, the chamber can be vented, and the solar cell and quartz slide can be removed.

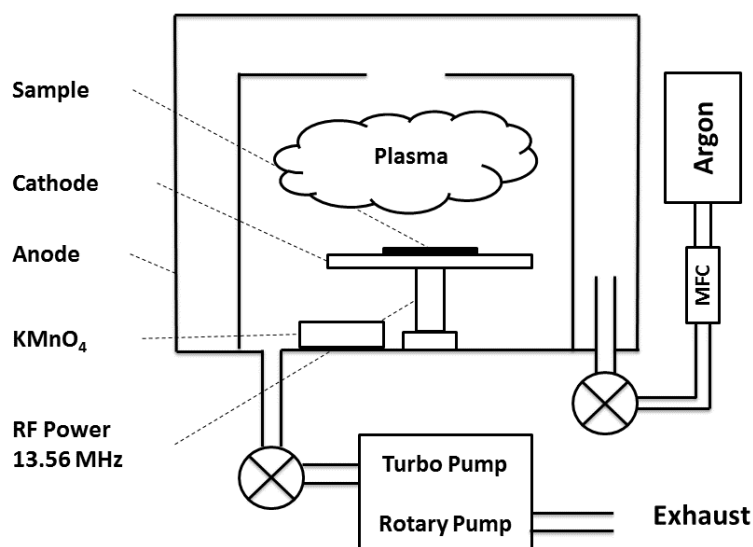


Figure 5.2: Schematic shows PECVD configuration for oxidation process.

After depositing titanium films on the solar cells, an oxidation process is started using plasma or thermal annealing.

Plasma annealing of the films is carried out using PECVD coating machine with the configuration shown in the schematic in Figure 5.2. The oxidation process of the films was carried out in the chamber of PECVD machine using the following conditions:

(processing time: 1 hour, amount of oxidising agent KMnO_4 : 30g, Argon gas flow rate: $25 \text{ cm}^3/\text{min}$, total pressure: 3×10^{-3} torr, power: 15 W, bias voltage: 100 V).

The samples were thermally annealed in the furnace at $300 \text{ }^\circ\text{C}$ for 1 hour at a controlled heat-up rate of $10 \text{ }^\circ\text{C}/\text{sec}$ to eliminate thermal shock to the material. Figure 5.3 shows the thickness-versus-time diagram of Ti oxidised to TiO_2 film. Once the thermal annealing process is completed, samples were left in the furnace to cool down to room temperature.

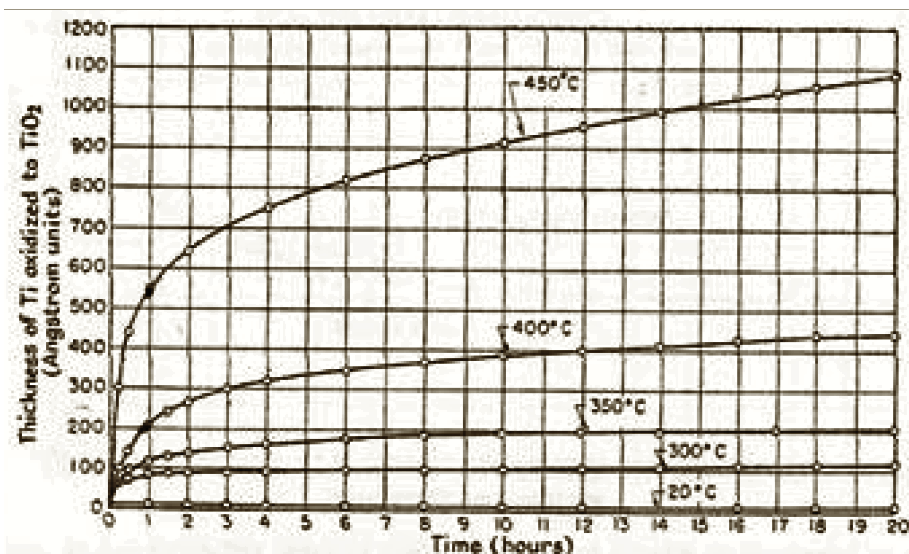


Figure 5.3: Thickness of Ti oxidised to TiO_2 versus the required time[118].

For solar cells with double layers, titanium films were produced using RF sputtering and a layer of silicon oxide deposited with conditions summarised in Table 5.2. Figure 5.4 shows a flow chart summarises step of the of coating process presented in this chapter.

Table 5.2: Summary of the coating conditions of silicon oxide layer for solar cells with a double anti-reflection layer of silicon oxide/titanium oxide.

Coating Conditions	TS ₁	TS ₂	TS ₃
DC Bias (volts)	100	100	100
TMS Flow Rate (cm^3/min)	25	25	25
Time (minutes)	15	15	15
KMnO_4 Mass (grams)	10	20	30

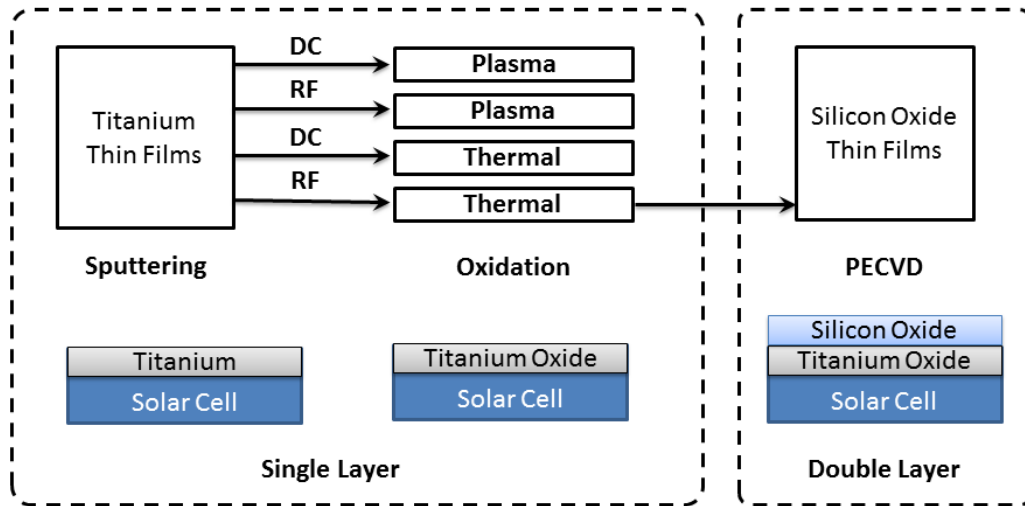


Figure 5.4: Flow chart illustrates the coating steps.

5.4 Results and Discussion

5.4.1 Single Layer Titanium Oxide

This section describes the results for silicon solar cells coated with a single layer of titanium thin film sputtered using DC or RF configuration and oxidised by means of plasma or thermal annealing.

Figure 5.5 shows the efficiency drop of the silicon solar cell coated with titanium thin films for the thickness of 4, 6 and 8 nm sputtered using DC or RF configurations and oxidised by plasma annealing. The bar chart shows the differences in the conversion efficiency by subtracting the conversion efficiency of the coated cells from uncoated ones. It can be seen from the bar chart that all the solar cells suffer a drop in efficiency after coating with titanium thin films oxidised by plasma annealing. This drop in efficiency increases with the increased thickness of titanium oxide layer for both types of the sputtered films. However, the decrease in the efficiency of the solar cells coated with titanium films with DC sputtering is higher than coated cells with RF sputtering.

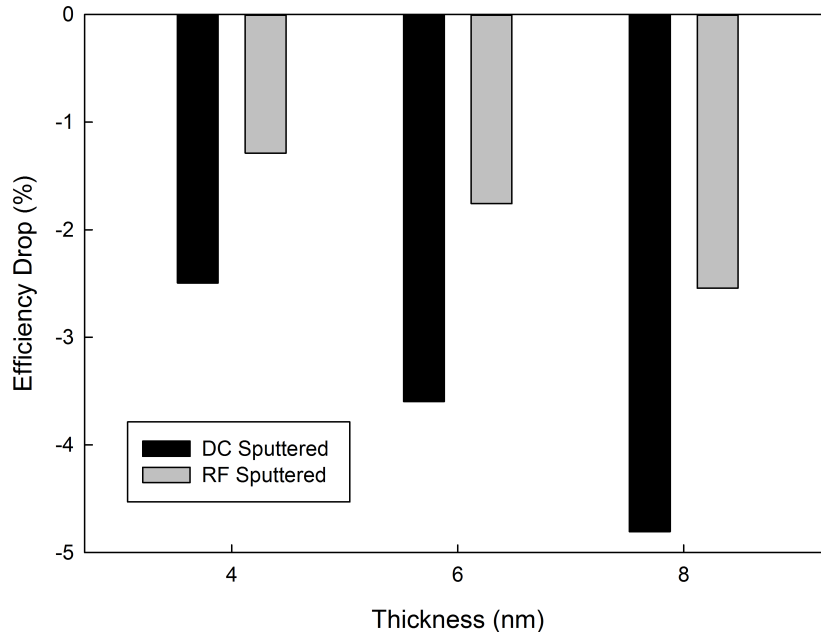


Figure 5.5: Efficiency drop of solar cells coated with plasma oxidised titanium films.

Figure 5.6 shows I-V curve of silicon solar cell coated with 4 nm RF sputtered titanium film before and after oxidation. It can be seen that titanium film before oxidation has a shadowing effect on the electrical parameters of the solar cell. Oxidation of the film increased from the efficiency of the solar cell in comparison to the efficiency of the cells before oxidation but it remains lower than the uncoated cell. The differences in the efficiency of the silicon solar cells coated with RF and DC sputtered can be seen as a result of the differences in the optical properties of the deposited films.

Figure 5.7 shows absorption spectra of titanium thin films after plasma oxidation process. It can be seen that the absorption of the deposited layer by RF sputtering increases with the increased thickness of titanium films. Moreover, the absorption of the DC sputtered film is greater than RF sputtered film for the same film thickness.

In order to understand the effects of RF and DC sputtering configurations as well as plasma and thermal annealing processes on the electrical characteristics of the solar cells, four solar cells were coated with a thickness of 4 nm of titanium where two of them were DC sputtered and the other two were RF sputtered. After that,

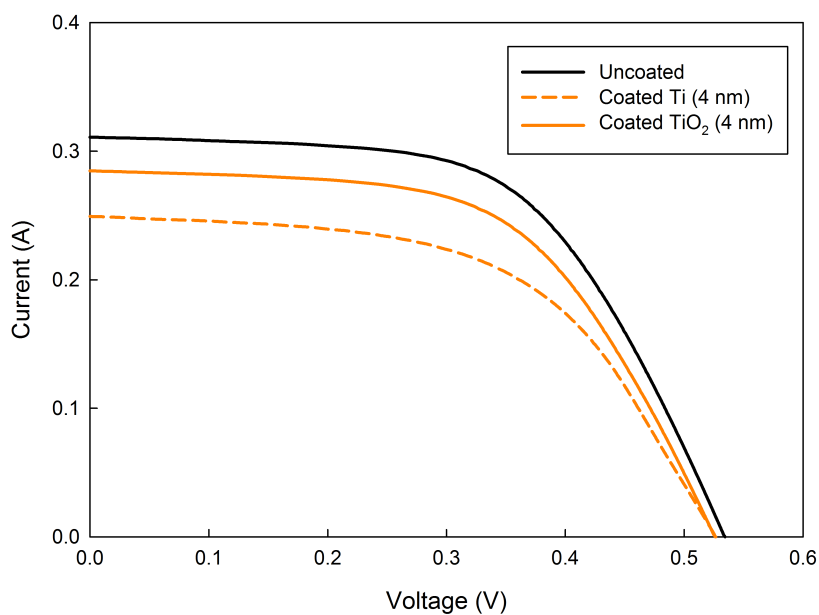


Figure 5.6: I-V curve of the solar cell coated 4 nm titanium before and after plasma oxidation.

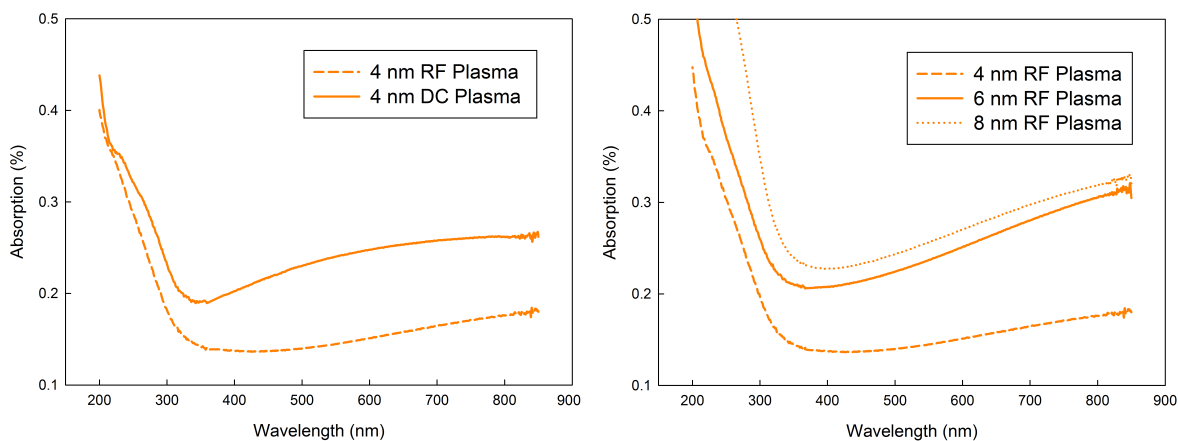


Figure 5.7: Absorption spectra of titanium films processed by plasma oxidation. (left), comparison RF/DC and (right), RF-influence of the titanium oxide film thickness.

solar cells were thermally or plasma annealed. It was found earlier that RF sputtering is more appropriate in comparison with DC sputtered titanium films oxidised with plasma annealing. Figure 5.8 also shows that RF sputtering is more appropriate than DC sputtered titanium films produced by thermal annealing. Annealed films also reduce the efficiency of the silicon solar cell but it can be seen that thermal annealing process produces better films in comparison with plasma annealing technique in terms of conversion efficiency.

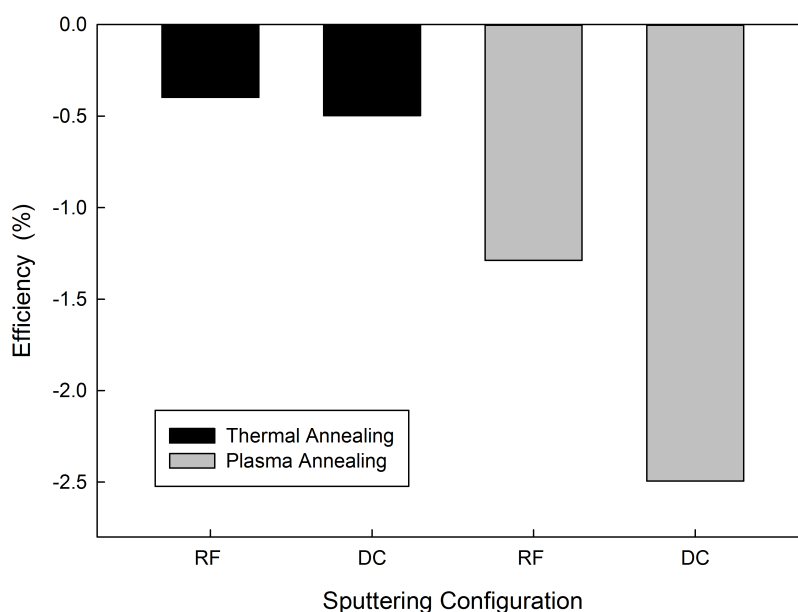


Figure 5.8: Efficiency drop using different techniques.

Figure 5.9 shows an insignificant difference in the absorption spectra of the RF or DC sputtered titanium films under thermal annealing process. However, DC sputtered film shows a greater absorption over RF sputtered film for the wavelengths below 500 nm. Moreover, it can be seen that thermally annealed films have lower absorption in comparison to plasma annealed cells. The electrical characteristics of the solar cells showed a significant decrease in the conversion efficiency for the solar cells oxidised by plasma annealing over thermal annealing. This increase in efficiency can be attributed to the significant increase in the absorption of the films oxidised by plasma annealing over the visible and near infra-red light in comparison to thermally annealed ones.

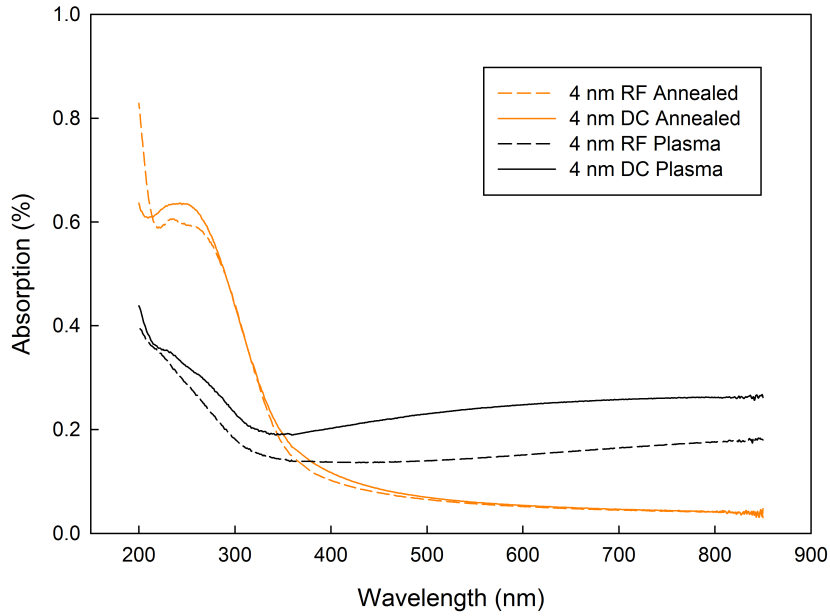


Figure 5.9: Absorption spectra of 4 nm TiO_2 coated with various conditions.

Figure 5.10 shows transmission spectra of titanium films deposited by RF sputtering with a thickness of 4, 6 and 8 nm before and after plasma annealing. It also shows the difference between the films with 4 nm thickness deposited by RF and DC sputtering and oxidised by thermal annealing.

For plasma annealed samples, it can be seen the effects of plasma annealing of titanium films where oxidation process is associated with an increase in the transmission of the layers. Also, the increase in the thickness of the deposited films corresponds to the reduction in the transmission of the films. The obtained results are in good agreement with the absorption spectra shown in Figure 5.7 where the reduction in transmission is due to the increase in the absorption of the films with increased thickness.

For thermally annealed films, it can be seen that thermally annealed films have a higher transmission (from 400 nm) in comparison to those produced by plasma annealed for the same thickness. For thermally annealed films, it can be seen that RF sputtered films have higher transmission than DC sputtered films.

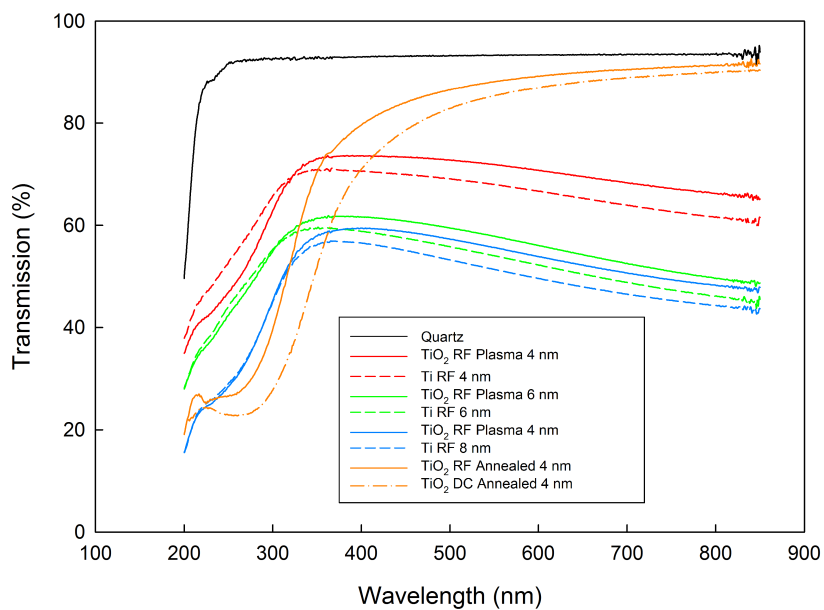


Figure 5.10: Transmission spectra of 4 nm TiO_2 coated with various conditions.

The conversion efficiency and the optical properties of titanium oxide layers produced using different methods were analysed. The next section compares the energy band gap and colour of these layers. The next section also shows the band gap energy of titania nanoparticles using High-Temperature Supercritical Drying (HTSD) method.

5.4.2 Energy Band Gap

The phase of titanium dioxide produced by plasma oxidation using potassium permanganate and thermal annealing was determined using UV-Vis spectroscopy and compared to titanium dioxide nanoparticles fabricated in the lab.

Parayil et al.[119] produced titanium dioxide nanoparticles with the Anatase structure by HTSD method of titanium isopropoxide mixed with methanol in nitrogen medium gas. Using similar approach titanium dioxide was produced in the lab by using the following materials as received:

Methanol (99+%, Alfa Aesar, UK), Propanol (99+%, Alfa Aesar, UK), and Titanium tetrachloride (99.9% trace metals basis, Sigma-Aldrich, UK).

In order to produce 1.5 gram of titanium, 3.5 mL of titanium tetrachloride was poured into 40 mL of methanol in a 500 mL capacity beaker. Then, the contents are stirred for 5 minutes using a magnet stirrer where titanium tetrachloride is fully dissolved in methanol. After that, the contents were poured into a glass liner and placed in an autoclave. The used autoclave in the experiment is Parr Model 5500

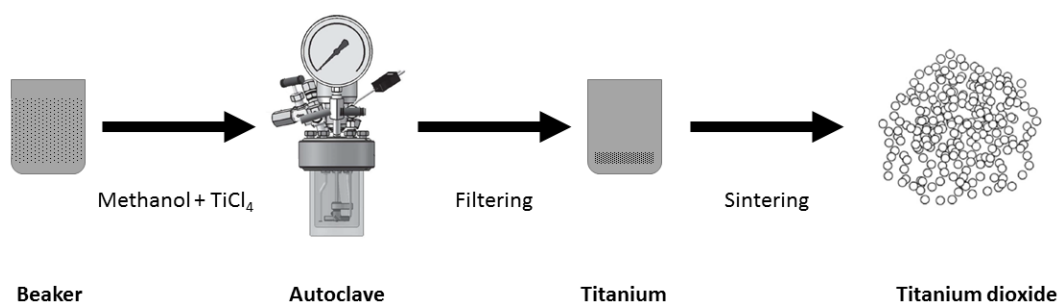


Figure 5.11: Illustration of the steps for preparation of titanium dioxide nanoparticles.

high-pressure compact stirred reactor with temperature controller Parr-4836. Hydrogen gas was introduced into the autoclave at a pressure of 10 bar. After that, the autoclave is heated at a rate of 1 °C/min to a final temperature of 200 °C. Once the temperature is achieved, the pressure of the autoclave is found to be around 52 bar.

Then the autoclave is maintained at 200 °C for two hours. The required temperature for obtaining titanium precipitates is found by repeating the experiments at temperatures of 150, 175 and 200 °C. After running the experiment for two hours, the autoclave is left to cool down to room temperature. Then, the autoclave is disassembled and the obtained powder is washed three times in a 500 mL conical flask.

The produced powder is thermally annealed in a furnace for 10 hours at 400 °C at a heating rate of 10 °C/min. An illustration of the steps for preparation of titanium dioxide nanoparticles is presented in the schematic in Figure 5.11.

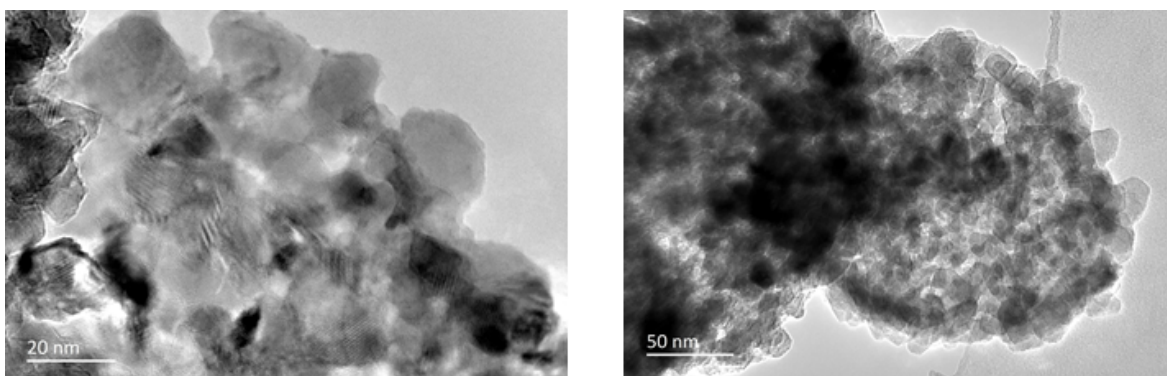


Figure 5.12: TEM images of Anatase (aerogel) titanium dioxide nanoparticles.

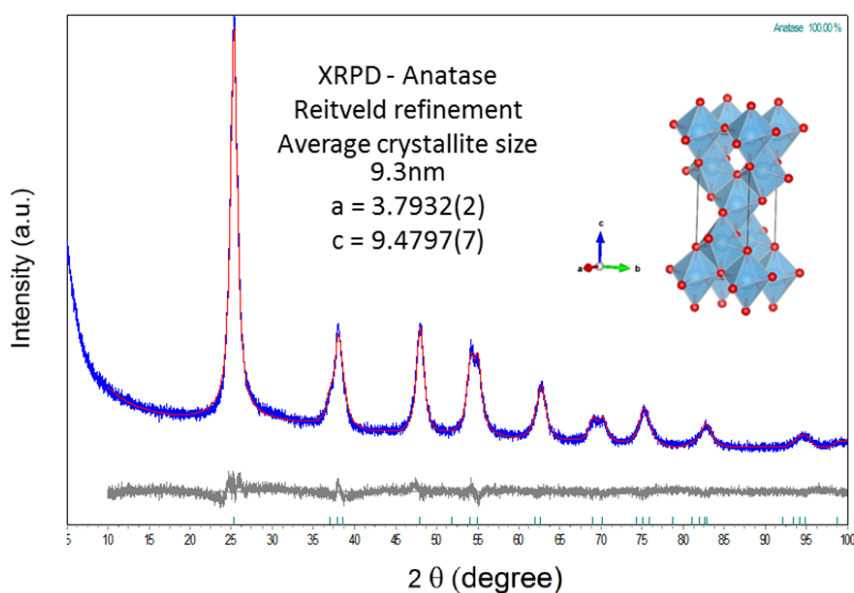


Figure 5.13: XRD patterns of Anatase (aerogel) titanium dioxide nanoparticles.

Figure 5.12 shows TEM images of the produced nanostructured aerogel titanium oxide material. XRD patterns of the titania aerogel produced in the lab is shown in Figure 5.13. The obtained powder is pure titania with Anatase phase [120]. The

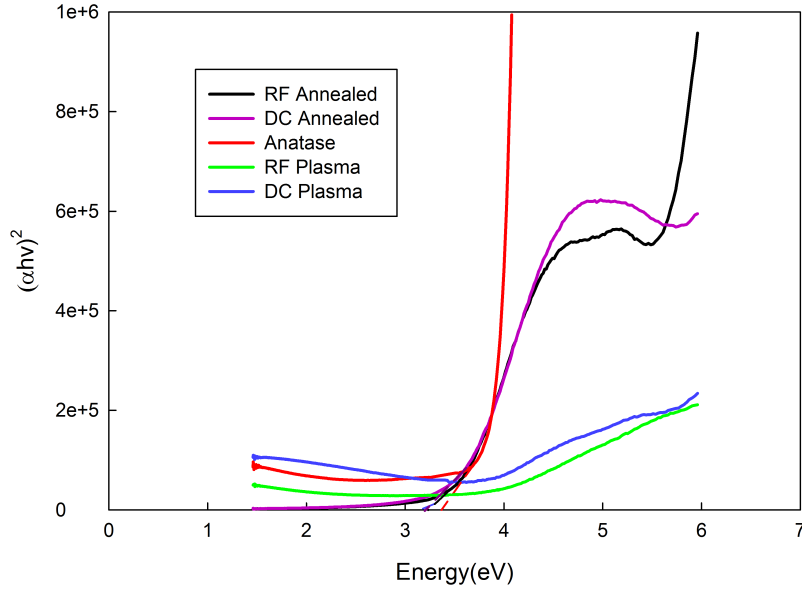


Figure 5.14: Energy bandgap obtained by extrapolating the linear portion of the versus $h\nu$ curve.

optical energy bandgap of the oxidised titanium films by either furnace or plasma annealing is estimated using the classical relation for optical absorption [121, 122]:

$$\alpha h\nu = B(h\nu - E_g)^m \quad (5.1)$$

Where B , E_g and $h\nu$ denote the band tailing parameter, the optical bandgap and the photon energy respectively. The energy band gap can be determined by extrapolation to the zero coefficients, which is calculated from the above equation. The intercept of the tangent to the plot $(\alpha h\nu)^2$ versus $h\nu$ shown in Figure 5.14 gives a good approximation of the band gap energy for this direct band gap material. The obtained band gap energies (E_g) of the TiO_2 nanoparticles, TiO_2 RF thermally annealed and TiO_2 DC thermally annealed were 3.54, 3.46 and 3.43 eV respectively. Energy band gap of the plasma oxidised films showed energy band gap of 3.03 and 3.1 RF and

DC sputtered films respectively. The obtained energy band gaps are larger than the value of 3.2 eV for the bulk TiO_2 . This can be explained because the band gap of the semiconductors has been found to be particle size dependent [123]. The band gap increases with decreasing particle size and the absorption edge is shifted to a higher energy (blue shift) with decreasing particle size. Considering the blue shift of the absorption position from the bulk TiO_2 , the absorption onset of the present samples can be assigned to the direct transition of electrons.

Figure 5.15 shows the colour of the RF sputtered films on quartz slides. It can be seen with the naked eye the difference in colour of the thin films before and after oxidation processes. For oxidised plasma films, the produced films have a grey colour while thermally annealed films provided a golden colour.

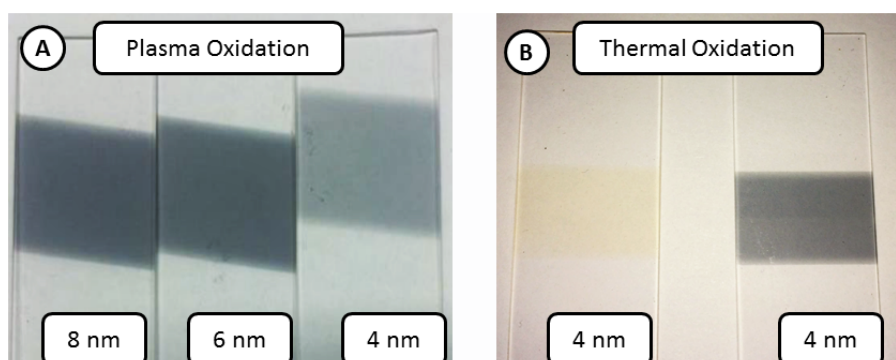


Figure 5.15: Titanium coated slides using plasma and thermal annealing.

Colour characterisation was conducted to supplement the data of the optical properties of titanium oxide films. The colour of the deposited titanium oxide layers on the slides and the Energy bandgap results correspond to the colour of thin films of titanium oxide. The golden colour is reported in literature for Anatase films [124, 125]. However, the grey colour is reported for non-stoichiometric films where titanium dioxide thin films exhibit greyish hue once they are reduced (Oxygen deficiency) to TiO_{2-x} or Ti_yO_x [126, 127, 128].

5.4.3 Double Layers Titanium/Silicon Oxide

In this section, the second layer of silicon film oxidised in situ with a different mass of the oxidising agent is deposited on the titanium oxide layer with a thickness of 4 nm produced by RF sputtering and oxidised by thermal annealing method.

Figure 5.16 shows the reflection spectra of the uncoated and coated solar cells with a double layer of titanium and silicon oxide. It can be seen from the spectra that coatings reduced the reflection of the solar cell surface. An increase in the reflection is observed in the region of 350-500 nm where the rise in the intensity of the peaks corresponds to the increase in the mass of potassium permanganate introduced to the coating chamber during the deposition of silicon oxide films.

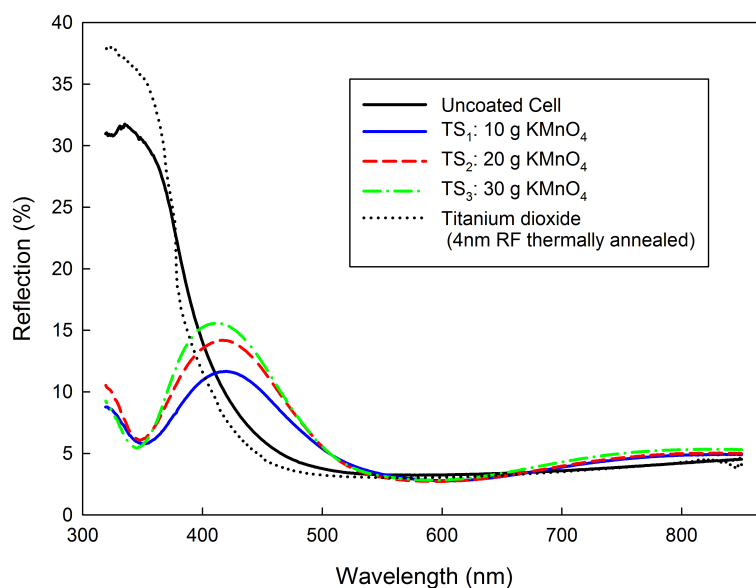


Figure 5.16: Reflection spectra of double layer coating.

Figures 5.17 and 5.18 show transmission and absorption spectra of silicon oxide and titanium oxide films respectively. Transmission spectra of the double layers produced with different coating conditions show slight differences where the reduction in transmission is associated with the increased mass of the oxidising agent introduced into the coating chamber. It can be seen from Figure 5.17 that depositing a second

layer of silicon oxide increased the transmission of the titanium oxide silicon oxide film compared to the titanium oxide film. The increase in the transmission of the wavy-shaped spectra can play a part in improving the electrical output of the solar cells in comparison to the single layer coated cells with titanium oxide.

Absorption spectra shown in Figure 5.18 are in good agreement with the transmission ones where the reduction in the transmission of these spectra corresponds to the increase in absorption of these films. The optical results demonstrates clearly the advantage of using low-high refractive index through the addition of silicon oxide and this can be reflected in an improvement in the conversion efficiency silicon solar cell.

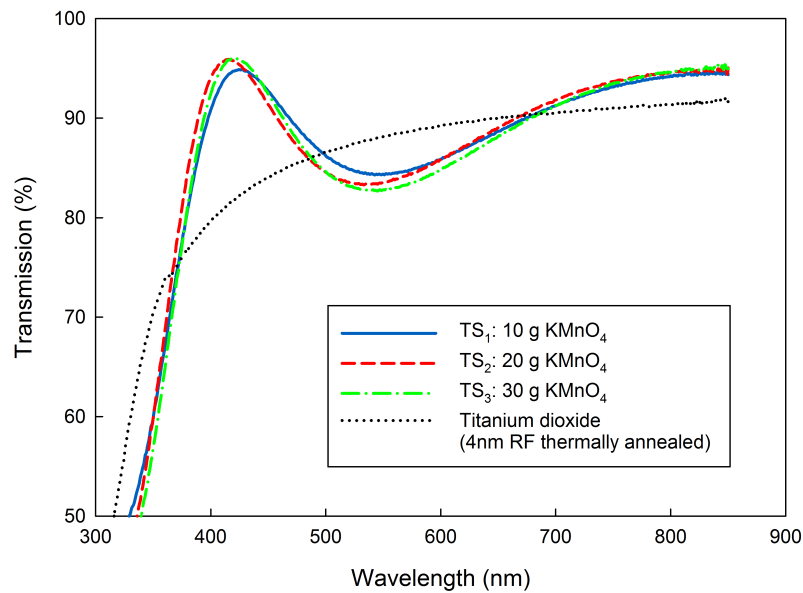


Figure 5.17: Transmission spectra of double layer coating.

Table 5.3 summarises the electrical characteristics of the solar cells before and after coating with double anti-reflection layers. It can be seen from the table that the solar cells before coating (C_1 , C_2 , C_3) do not share identical values of the parameters of electrical characteristics of the solar cells. This variation represented in different values of the short-circuit current and fill factor. This difference is due to the induced effects of the laser cutting process on the solar cell where solar cells were cut into smaller sizes to fit in the coating chamber of the sputtering deposition system.

A photograph of the solar cell is shown in Figure 5.19. It can be seen from the table an increase in the conversion efficiency of the solar cells with multi-layers of anti-reflection coatings. An increase in the conversion efficiency from 12.057% to 12.265%, from 11.864% to 12.028% and from 11.960% to 12.161% for the solar cells coated using the coating conditions in TS_1 , TS_2 and TS_3 respectively.

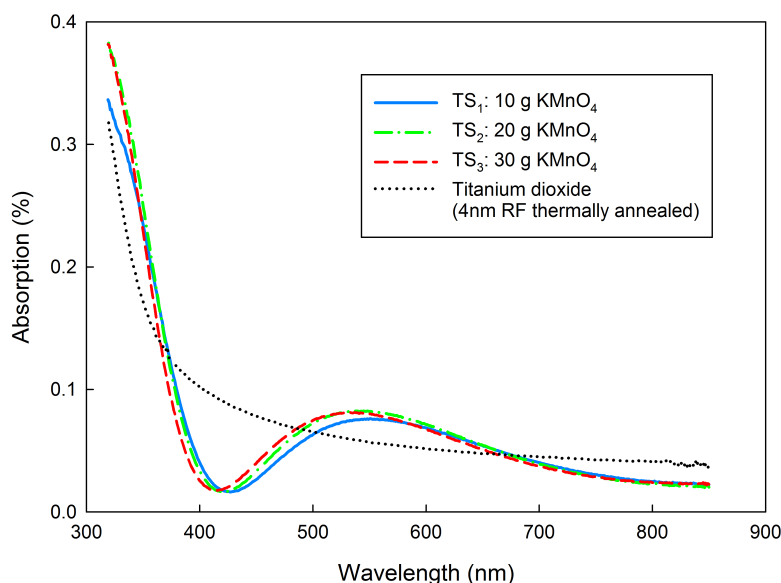


Figure 5.18: Absorption spectra of double layer coating.

The produced coatings are associated with an absolute enhancement between 0.16 and 0.20 in the electrical conversion efficiency of the solar cells. Since the obtained optical properties of the double layers of silicon oxide and titanium oxide showed insignificant differences and the variance in the initial conditions of the parameters of the electrical characteristics of the solar cells, it can be concluded that double anti-reflection coating improved the electrical performance of the solar cell. However, the differences in the electrical parameters are too small for a precise quantification of the conversion efficiency enhancement with the different coating conditions.

The measured P-V and I-V curves of the silicon solar cell coated with a double layer of silicon oxide and titanium oxide with optimum enhancement obtained are shown in Figure 5.19. Under the test conditions, the solar cell before coating shows

an open circuit voltage of 0.549 V, short-circuit current of 285 mA, fill factor of 62%, and conversion efficiency of 12.057% are presented. After the coating process, the

Table 5.3: Electrical characteristics of the uncoated and coated cells with a double ARC layers at the illuminated surface area of 8.544 cm², 1000 W/m² and 25 °C.

Sample	I_{sc} A	V_{oc} V	P_{mp} W	FF –	η %
Uncoated (C ₁)	0.285	0.549	0.0969	0.62	12.057
TS ₁	0.291	0.550	0.0986	0.62	12.265
Uncoated (C ₂)	0.280	0.549	0.0954	0.61	11.864
TS ₂	0.286	0.550	0.0967	0.61	12.028
Uncoated (C ₃)	0.283	0.549	0.0961	0.62	11.960
TS ₃	0.289	0.550	0.0978	0.62	12.161

parameters of the electrical characteristics of the solar cell show an open circuit voltage of 0.550 V, short-circuit current of 291 mA, fill factor of 62%, and conversion efficiency of 12.265%. The obtained increase in the conversion efficiency of the solar cell is a result of the improved optical properties of the deposited layers which are reflected in an increase in the short circuit current.

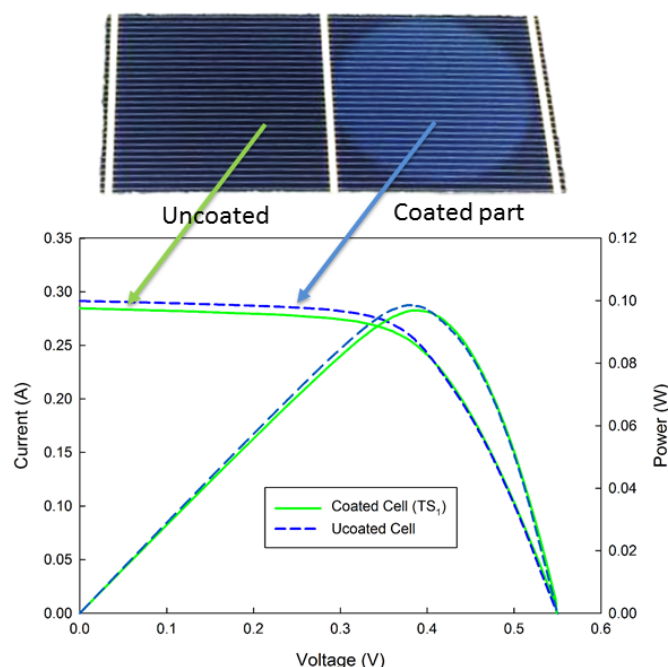


Figure 5.19: I-V and P-V curve of solar cells with double layer coating at the illuminated surface area of 8.544 cm², 1000 W/m² and 25 °C.

5.5 Summary

In this chapter, thin films of titanium were deposited on silicon solar cells using sputtering technique at room temperature. Titanium films were oxidised using plasma or thermal annealing. Oxidised titanium thin films were studied as single layer coating for silicon solar cells.

The effects of the optical properties and electrical characteristics of these layers on the conversion efficiency of the cells were presented. Optical energy bandgap of the deposited films was studied and compared to a known structure of titanium oxide produced in the lab. Optical and electrical analysis showed that RF sputtering is more appropriate over DC sputtering for the solar cell. Moreover, thermal annealing showed a better suitability for solar cell coating.

The effects of an additional layer of silicon oxide on titanium oxide with optimum characteristics obtained for solar cells were studied. Double layers of silicon oxide and titanium oxide showed an enhanced electrical conversion efficiency in comparison to the uncoated solar cell.

Chapter 6

Phosphor for PV Solar Cell

This chapter presents the experimental work on using ultraviolet-spectral down conversion material for enhancing the spectral response and electrical characteristics of commercial mono-crystalline silicon solar cells. The down-converting material employed in the experiment is gadolinium oxysulfide doped with erbium and terbium where the phosphor material is synthesised by the urea homo-precipitation method.

Silicon cells were coated with a luminescent layer consisting of the phosphor material encapsulated in Ethyl Vinyl-Acetate (EVA) binder using doctor-blade screen printing technique. With an optimum concentration of phosphor in the composite resulted in the largest light conversion, and improved electrical output and energy transfer efficiency. The obtained results showed that the composition of dispersed phosphors has a strong influence on the amount of ultraviolet light converted and transition electron capacity of PV cells. The experimental results showed in an optimised silicon solar cell, a relative enhancement of 4.45% (from 12.11% to 12.65%) in the energy conversion efficiency of PV solar cell was achieved.

Finally, the effects of combining silicon oxide layers described in chapter 4 together with the luminescent composite are also presented in this chapter.

6.1 Introduction

Currently, photovoltaic modules that dominate the market are based on crystalline silicon because of its abundance, stability, non-toxicity and relatively low processing costs [76]. These commercially produced PV silicon cells show a poorer spectral response to the UV and blue wavelengths compared with the visible light of the solar spectrum.

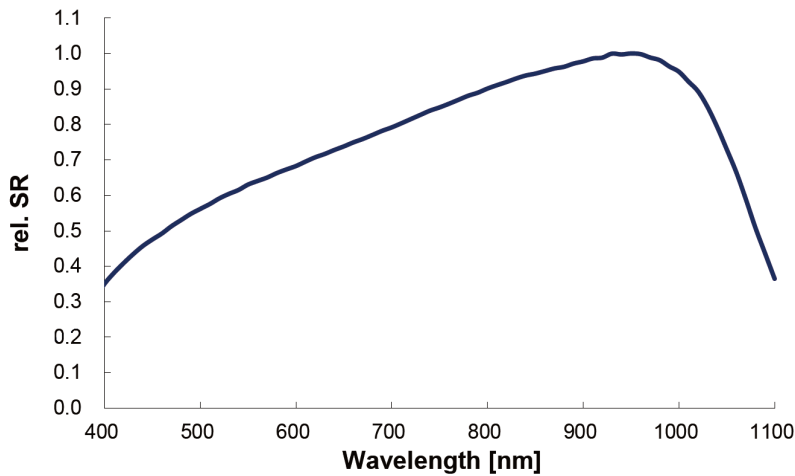


Figure 6.1: Typical spectral response (SR) vs wavelength of Motech silicon photovoltaic solar cell [68].

Figure 6.1 shows the spectral response of the solar cell used in the experiments. It can be seen that the spectral response increases for wavelengths shorter than the bandgap of silicon at 1100 nm (1.1 eV), peaking at 960 nm and then decreases toward the short wavelengths. The fundamental reason is short wavelength photons have high energy content whose energy is difficult to harness efficiently due to interaction with the front layers of the PV device [129]. Therefore, the short wavelength response is reduced due to some distinctive mechanisms:

- Fast recombination rate in the heavily doped emitter.
- Parasitic absorption and reflection due to the silicon nitride ARC [130].

Spectral conversion principle based on nanostructured materials technology can

be used through down conversion technique to improve the performance of the PV solar cell. Down conversion approach is based on absorbing high energy photons (short wavelengths band) of the light and re-emits it at lower energy photons (long wavelengths band). Therefore, it can overcome the poor response of the silicon solar cells in the short wavelengths and consequently improve the energy conversion efficiency of the solar cell.

Spectral conversion applied in the experiment consists of a luminescent layer composed of erbium and terbium-doped gadolinium oxysulfide phosphors embedded in a transparent layer of EVA. A fraction of the UV light incident on the luminescent composite is absorbed by $Gd_2O_2S(Er,Tb)$ and re-emitted into the solar cell as a green light. The rest of the photons are absorbed by the solar cell directly as shown in Figure 6.2. A pyramidally textured structure of Si_3N_4 coated on the surface of the c-Si solar cell is widely used to increase the absorption of the solar light [131].

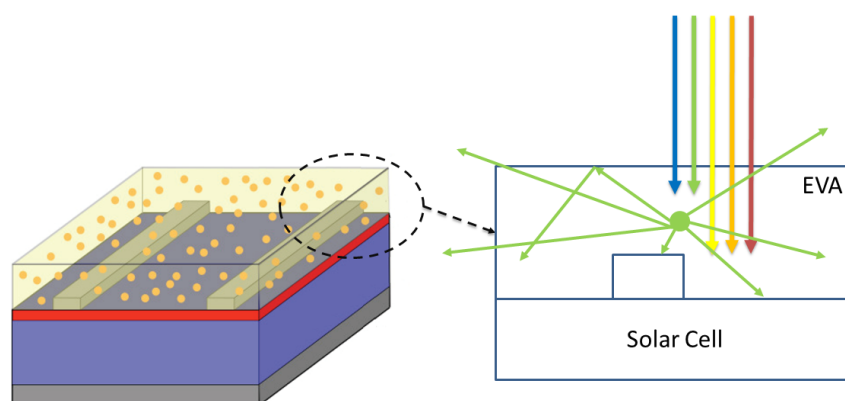


Figure 6.2: Operating principle of the luminescent material. Re-drawn from [132].

The emission of the phosphor is multi-directional, and it can be emitted in all directions. Subsequently, when the DC material is placed on top of silicon solar cell, it is only expected that half of the luminescence emitted by down converter contributes to photo-current emitted into the direction of the solar cell [133]. Therefore, a fraction of the re-emitted photons escape to the top, and the edge of the cell and some are re-absorbed and go through these processes again. All other photons reach the solar

cells directly or through reflection from the top surface. However, the pyramidally textured surface can reduce this loss and thus more exploited photons can contribute to the generation of charge carriers and consequently increasing the conversion efficiency. The optical properties of the luminescent composite should be controlled to maximise the fraction of photons reaching the solar cell and converting into electricity.

6.2 Aim and Objectives

The aim of the experimental work is to improve the energy conversion efficiency using down-converting material which absorbs the UV light where the solar cell is inefficient and emits in the visible range where the solar cell has a better response to the light. The objectives of the experiments are summarised as follow:

- Evaluate and examine the potential applications of down-converting Tb^{3+} and Er^{3+} co-doped $\text{Gd}_2\text{O}_2\text{S}$ in an attempt to improve the efficiency of silicon-based PV cells through comparative study of the performance of the solar cells before and after coating.
- To understand the separate and combined effects of the EVA binder and the phosphor on the solar cells performance.
- Utilising doctor blading screen printing technique as low-cost implementation method to form a luminescent layer directly on top of commercially available mono-crystalline PV solar cell to convert the UV photons into photons with longer wavelengths where the Si solar cell shows a better response.

6.3 Related Work

The potential of DC materials to improve the conversion efficiency of the single junction crystalline silicon solar cells using spectral conversion technique has attracted many researchers. They demonstrated an enhancement in the performance of the solar cells by incorporating a downconverting luminescent film into solar cells.

6.3.1 Energy Enhancement Using Luminescence Species

Chung et al. reported an energy improvement of the PV solar cell by utilising a down-converting phosphor of $\text{Y}_2\text{O}_2\text{S}:\text{Eu}^{+3}$ dispersed in PVA on top of EVA encapsulated mc-Si solar cell. An increase in power conversion efficiency by up to a factor of 14 under UV illumination [134]. Also, Marchionna et al. who demonstrated 1% absolute increase of the delivered power of commercial mono-crystalline solar cell for the case of Air Mass 0 lighting conditions with an active coating of poly-vinyl acetate film doped with Phenanthroline- Eu^{+3} complex [135].

Wang et al. achieved 0.42% absolute enhancement in the conversion efficiency of multi-crystalline silicon cell by applying a luminescent layer of Eu^{+3} complexes incorporated in EVA [136] on top of the solar cell.

Yen-Chi et al. have demonstrated an absolute increase of 0.64% in the power conversion efficiency of multi-crystalline silicon solar cell coated with down-converting $\text{KCaGd}(\text{PO}_4)_2:\text{Eu}^{+3}$ phosphor dispersed in PMMA matrix [137]. Moreover, the authors demonstrated the effect of placing of an up-converting layer on top and the bottom of the silicon solar cell. The authors showed an enhancement in the conversion efficiency of the mc-Si solar cell by applying up-converting $\text{La}_2\text{Mo}_2\text{O}_9:\text{Yb,Er}$ phosphor dispersed in PMMA matrix. An absolute enhancement of 0.27% is obtained when the phosphor is applied on the top of the solar cell, and 0.44% is obtained when applied to the backside of the solar cell [138].

6.3.2 Encapsulation of the Luminescence Species

DC materials can be incorporated in various ways in the PV modules such as:

- Incorporating Luminescence species in a commercial encapsulation binder. Researchers showed the possibility of mixing the phosphor material with the binder and then spin coated into the solar cell [134, 135]. Also, the phosphor could incorporate into the binder by soaking pre-existed EVA sheets in luminescent solution of Eu^{+3} complexes [136].
- Doping the top float glass of module [139].
- Depositing the phosphor directly on top of the silicon solar cell [140].

6.4 Experimental Method

6.4.1 Materials

Terbium, Erbium-doped gadolinium oxysulfide $\text{Gd}_2\text{O}_2\text{S}(\text{Er}_x, \text{Tb})_x$ is selected for the study as a material of interest due to its UV photons absorption and visible emission as the response to these stimuli. The selected $\text{Gd}_2\text{O}_2\text{S}(\text{Er}_{0.2}, \text{Tb})_{0.01}$ phosphor has a lower refractive index than Si or Si_3N_4 that may be capable of converting more UV photons into longer wavelength where Si-based solar cell shows a greater response. This section shows the properties of the used materials in the fabrication of the luminescent layer for the solar cell.

6.4.1.1 Luminescent Material

Rare earth oxysulfide phosphors are one of the promising materials due to their good luminescent properties in comparison with other optical materials. They are used

for X-ray intensifying screen for medical diagnosis or cathode-ray screens. These materials could be synthesised as powders with characteristics depending on the particle size and morphology that are regulated during the synthesis stage [141].

Nanometre-sized rare earth doped phosphor powder, $\text{Gd}_2\text{O}_2\text{S}(\text{Er}_{0.2},\text{Tb})_{0.01}$, is prepared by Xiao et al. at Centre for Phosphors and Display Materials at Brunel University [142]. The author reported controlled phosphor emission intensity through cross-relaxation processes by changing the ion concentration where the optimum concentration obtained by the author is used for the experiments.

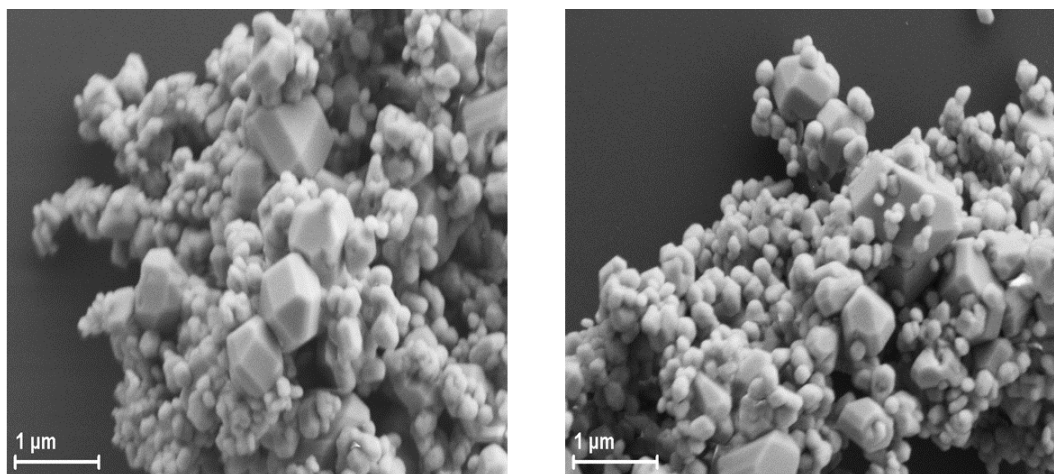


Figure 6.3: SEM images of $\text{Gd}_2\text{O}_2\text{S}(\text{Er}_{0.2},\text{Tb})_{0.01}$ particles.

Rare earth ions (RE^{3+}) activated phosphor lattices is produced via two-step process:

The first step is obtaining sub-micron spherical precursor powders using the urea homogeneous precipitation which resulted in a non-crystalline material with spherical particle morphology.

The second step is converting the non-crystalline precipitates into oxysulfide phosphors via appropriate firing treatment. A detailed description of the fabrication procedures can be obtained from [142]. Figure 6.3 shows SEM images of the morphologies of Tb^{3+} and Er^{3+} co-doped $\text{Gd}_2\text{O}_2\text{S}$ sample.

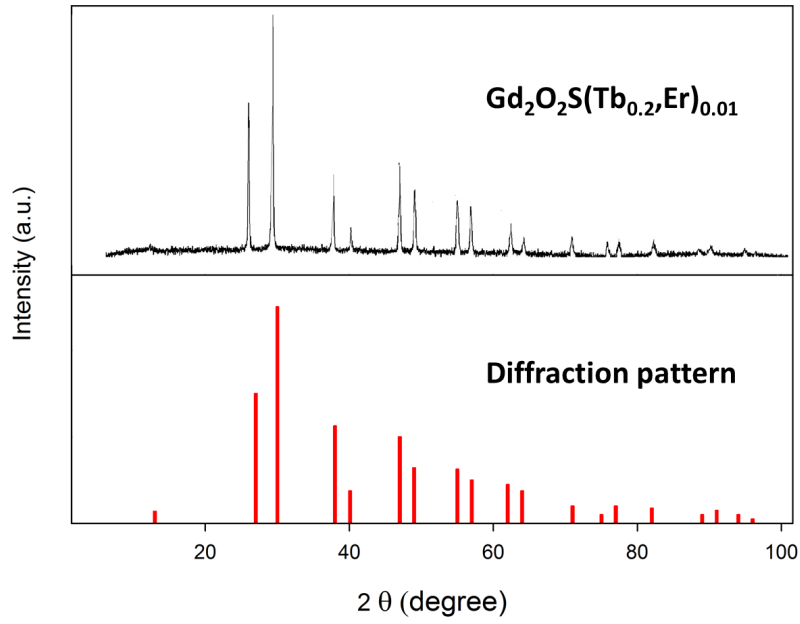


Figure 6.4: XRPD patterns of Tb^{3+} and Er^{3+} co-doped $\text{Gd}_2\text{O}_2\text{S}$.

Figure 6.4 presents simple bars which correspond to the crystallographic reference (PDF 03-065-3449 $\text{Gd}_2\text{O}_2\text{S}$ Gadolinium Oxide Sulfide) where the $\text{Gd}_2\text{O}_2\text{S}$ diffractogram is obtained experimentally using XRPD. It can be seen from the matched diffraction patterns that the used material is free from impurities where all the peaks are related with the pure hexagonal phase of ($\text{Gd}_2\text{O}_2\text{S}$) where the metal ion is surrounded by four oxygen and three sulfur ions without impurities. The diffraction pattern of the phosphor shows a good agreement with the hexagonal phase of the Gadolinium Oxysulfide structure reported in [143]. Table 6.1 shows the calculated crystallites size data obtained from TOPAS software associated with the XRD machine.

Table 6.1: Crystal size and lattice parameters of the phosphor particles.

Material	Crystal Size (nm)	a(Å)	c(Å)
$\text{Gd}_2\text{O}_2\text{S}(\text{Er}_{0.2},\text{Tb})_{0.01}$	155.7	3.7265	6.2651

Composite STEM and Cathodo-luminescence (CL) image taken in TEM that shows the high uniformity of visible light emission from the nano-phosphor synthesised using a homogeneous precipitation method. Figure 6.5 CL and High Angle Annular

Dark Field (HAADF) STEM composite image of the phosphor.

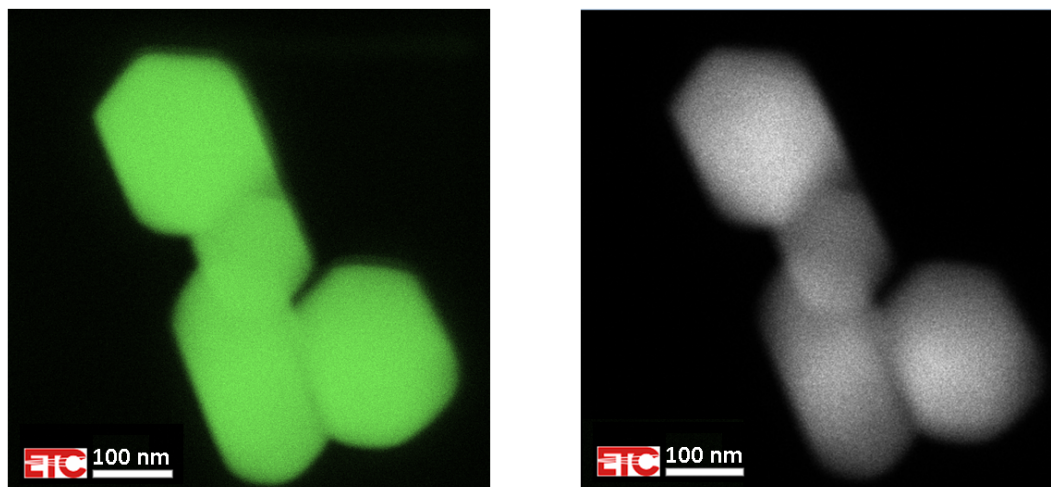


Figure 6.5: Luminescent material used in the experiment.

$\text{Gd}_2\text{O}_2\text{S}(\text{Er}_{0.2},\text{Tb})_{0.01}$ phosphor can be excited with 292 nm UV light and produces green emission peaking at 545 nm. Figure 6.6 shows the PLE absorption spectrum of $\text{Gd}_2\text{O}_2\text{S}(\text{Er}_{0.2},\text{Tb})_{0.01}$ phosphor in the wavelength domain of 250 to 334 nm and a maximal emission in the wavelength in the domain of 535 to 560 nm. Since the silicon solar cell shows poor absorption in the UV spectral range, applying $\text{Gd}_2\text{O}_2\text{S}(\text{Er}_{0.2},\text{Tb})_{0.01}$ phosphor on top of solar cell surface would be expected to enhance the spectral response of the cell and thus the conversion efficiency.

Figure 6.21 presents the temperature coefficient of the uncoated, EVA coated, and EVA+phosphor coated solar cell. It can be seen for all solar cells a decrease in the open circuit voltage and consequently the conversion efficiency of the PV cell performance decreases with increasing temperature. The output power of a PV cell depends linearly on the operating temperature, and it decreases with the increasing temperature due to the intrinsic properties of the solar cell [144].

Utilising the down-converting material could improve the performance of the solar cell as a result of reducing the phenomenon of thermally excited phonons. Excitation of phonons occurs when photons with energy greater than the bandgap energy in

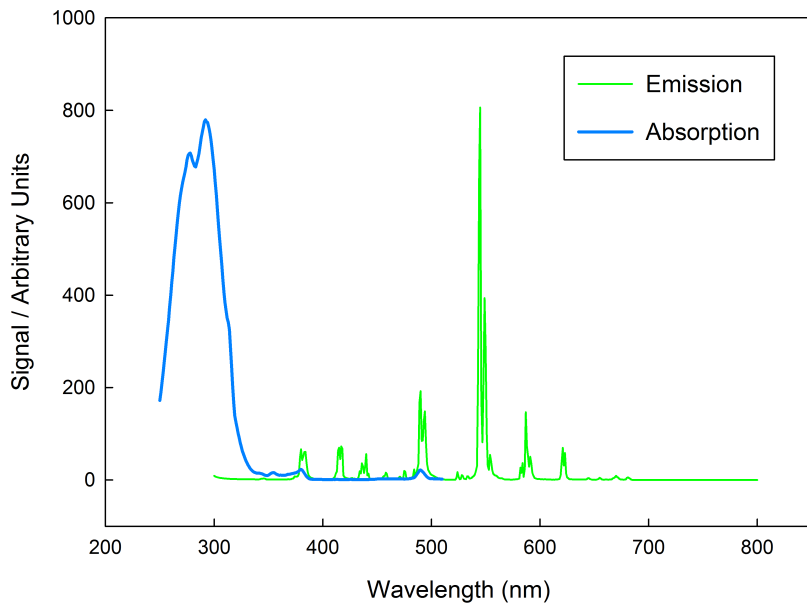


Figure 6.6: PLE and PL of the phosphor at room temperature.

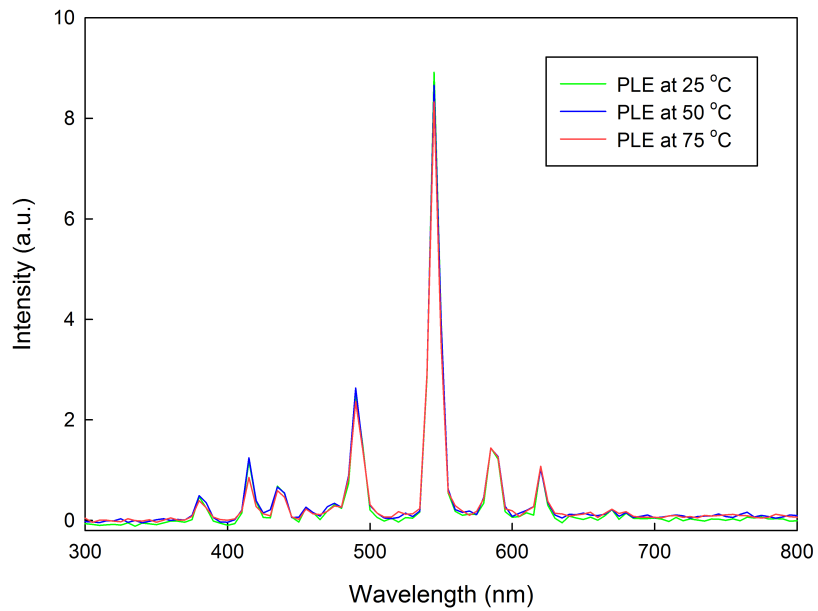


Figure 6.7: Emission of the phosphor at different temperatures.

which are absorbed by silicon solar cells. The excess energy leads to thermalisation of charge carriers and hence limit the theoretical efficiency. However, a decrease in the PL emission of the phosphor with increasing temperature would result in a lower electrical efficiency due to less emission obtained.

Since the operating temperature plays a principal role in the photovoltaic conversion process, it is necessary to examine the stability of the emission of the phosphor material at elevated temperatures. According to earlier reports [145, 146], the highest intensity of photoluminescence of the material occurs at low temperature and decreases with elevated temperature which is a typical feature of the phosphor material. Figure 6.7 shows the emission spectra of the $\text{Gd}_2\text{O}_2\text{S}(\text{Er}_{0.2},\text{Tb})_{0.01}$ phosphor at temperatures of 25, 50 and 75 °C. It can be seen that the emission of the phosphor material has a very marginal reduction in the emission of the elevated temperature with the range of study.

From the results, it can be concluded that the effect of the phosphor emission intensity at elevated temperature is insignificant on the reduction of the solar cell performance at elevated temperature. Therefore, the reduction of the PV cell performance at higher temperature comes from the intrinsic properties of semiconductor operation with increased temperatures as shown in Figure 6.21.

6.4.2 Binder

Various materials can be used for encapsulation of solar cells, but the used binder in the experiments is Ethylene-Vinyl Acetate (EVA), also known as poly(ethylene-vinyl acetate) (PEVA), is the copolymer of ethylene and vinyl acetate with chemical formula $(\text{C}_2\text{H}_4)_m(\text{C}_4\text{H}_6\text{O}_2)_n$. The chemical structures of ethylene and vinyl acetate monomers and poly (ethylene vinyl acetate) is illustrated in Figure 6.8.

In the commercial production of EVA encapsulate, the binder is typically for-

mulated with additives such as curing agent, UV stabiliser, antioxidant and adhesion promoter [147, 148].

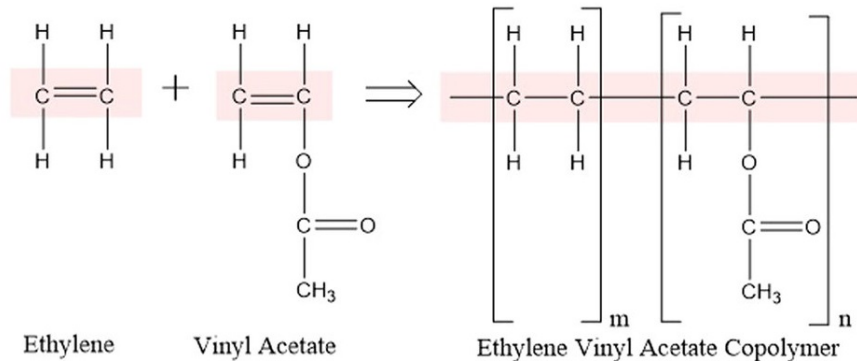


Figure 6.8: Chemical structures of ethylene and vinyl acetate monomers and poly (ethylene vinyl acetate) [149].

EVA is widely used in the photovoltaic industry. It has many desirable properties which make it the material of choice for this study:

- EVA is suitable encapsulating material for crystalline modules designed for a 25-year operational lifetime.
- EVA is easy to handle material as it is not adhesive at room temperature.
- EVA cross-linking allows a permanent and adhesive tight seal in the solar-cell system as well as enhanced bonding when the EVA layer is heated [150].
- Cross-linked EVA has high optical transmittance, good adhesion to various PV module materials, excellent dielectric properties, and significant moisture barrier properties.

6.4.3 Solvent

Various organic solvents were screened to select an appropriate one for dissolving EVA. The most favourable solvents for dissolving EVA are the aromatic-type ones [151, 152]. Chlorinated aromatic solvents such as o-dichlorobenzene and chlorobenzene

are suitable solvents for EVA dissolution [152]. However, they were excluded in the study for health, safety and environmental reasons. The technology development requires the search for alternative lower toxicity solvents that could provide with appropriate morphology for enhanced solar cells.

The final morphology of the layer depends on many factors where the choice of the solvent, annealing temperature and time are the most critical ones. Properties of the solvent including the vapour pressure, boiling point and surface tension of the solvent have great influence on the morphology of the deposited layer [153]. Table 6.2 summarises the properties of the screened solvents for this study.

Table 6.2: Physical properties of the solvents.

Solvent	P-xylene [154]	Chlorobenzene [155]	Toluene [156]
Molecular Formula	C ₈ H ₁₀	C ₆ H ₅ Cl	C ₇ H ₈
Colour	clear	clear	clear
Vapour Pressure (mbar at 20 °C)	8	12	29
Boiling Point (°C)	138	131	111
Surface Tension (dyn/cm at 20 °C)	28.27	32.99	28.52
Viscosity (mPa/s at 20 °C)	0.648	0.8	0.6

6.4.4 Coating Process

Mono-Crystalline silicon solar cells XS156B3 from Motech were used. The c-Si solar cells with an area of 15.6×15.6 cm² were cut into three equal sizes by CTR TMX90 laser machine. The EVA or Phosphor/EVA mixture is then blade screen printed on top of random pyramids structure of Si₃N₄ reflective layer of the solar cells. Only an area of 3×3 cm² of each cell was coated. Then, the coated cells were heated in the furnace to 190 °C at 10 °C/min. After the heating step, leads were welded on them. Preparation of the EVA and EVA+Phosphor layers and their deposition are described in the following subsections.

6.4.4.1 EVA Layer

EVA was used in the experiment for encapsulation. EVA was supplied from STR Solar company as a foil with a thickness of 0.40 mm. EVA foils were dissolved in P-Xylene solvent in different ratios of 6, 10, 14 and 18 wt% where 300 mg of EVA is used for each concentration. EVA sheet for the respective concentration is cut into small pieces to facilitate the dissolving process. Then, EVA and P-Xylene were mixed in a beaker using a magnetic stirrer for 15 minutes. After that, glass substrates were coated with different ratio of EVA-solvent mixtures using doctor blade printing technique to study the optical properties of the layer. Also, solar cells were coated to examine the effects of the EVA layer on the electrical performance of the silicon solar cell. The ratio of 18 wt% has resulted in a homogeneous layer of EVA applied on top of the cell as well as presenting good optical properties of reflection and transmission. Thus, this ratio was chosen for mixing with the luminescence phosphor.

6.4.4.2 EVA+Phosphor Preparation

Phosphor nano-powder $\text{Gd}_2\text{O}_2\text{S}(\text{Er}_{0.2},\text{Tb})_{0.01}$ produced at Centre for Phosphors and Display Materials was used in the experiment. Different mass weights of the phosphor powder of (1, 3, 5, 7) mg were dispersed in P-Xylene using the ultrasonic bath for 15 minutes then the photo-luminescent solution is well mixed with EVA in ratios of 18 wt%. Different concentrations of the phosphor powder were used in an attempt to find the best concentration of the phosphor powder to the EVA that results in an optimum energy conversion enhancement in the PV cell.

6.4.4.3 Layer Application

EVA and Phosphor+ EVA layers were deposited by doctor blade screen printing technique. Figure 6.9 shows examples of the films produced these approach under

UV light illumination where the top cell, shows a green emission, is coated with Phosphor+EVA and the bottom cell is coated with EVA layer only.

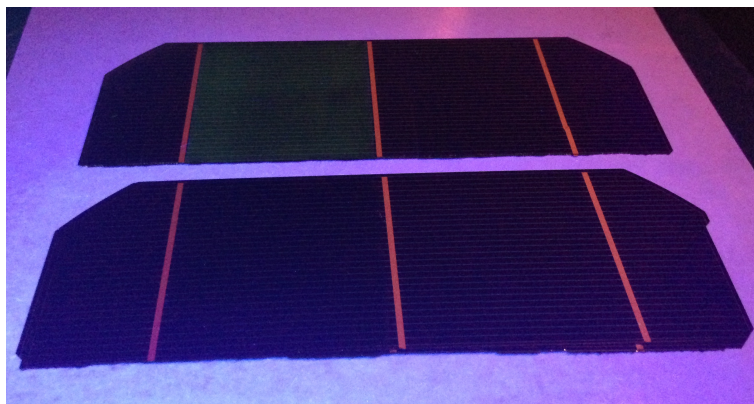


Figure 6.9: EVA+Phosphor coated (top) and EVA coated (bottom) solar cell under UV light excitation.

Doctor blade screen printing technique is a quick method for films deposition. The coating process is illustrated in Figure 6.10. It starts with placing the guides on the solar cell where the used guides in the experiments are low tack 0.1 mm thick from (3M, UK). Then, a solution of EVA or EVA+Phosphor mixture is dropped through pipette onto the solar cell between two guides near the edge. After that; the solution drops are spread by pulling the blade across the guides forming a luminescent layer on the cell. Many factors affect the thickness of the film including the height of the guides, the concentration of the mixture, the surface energy of the substrate and the surface tension of the solution. However, the height of guides has the greatest impact for controlling the thickness of the formulated layer [69]. Using this method, the variation in thickness of the produced layer over the applied surface is $\pm 3 \mu\text{m}$, but it is subject to the thickness of the guides. The variation in the thickness of the layer was measured using roughness measurements by Talysurf instrument with a resolution of $0.1 \mu\text{m}$.

The applied mixture of Phosphor and EVA formed a layer with a thickness of about $9 \mu\text{m}$ on the surface of the solar cell. A schematic of the luminescent layer applied on top of solar cell is illustrated in Figure 6.11.

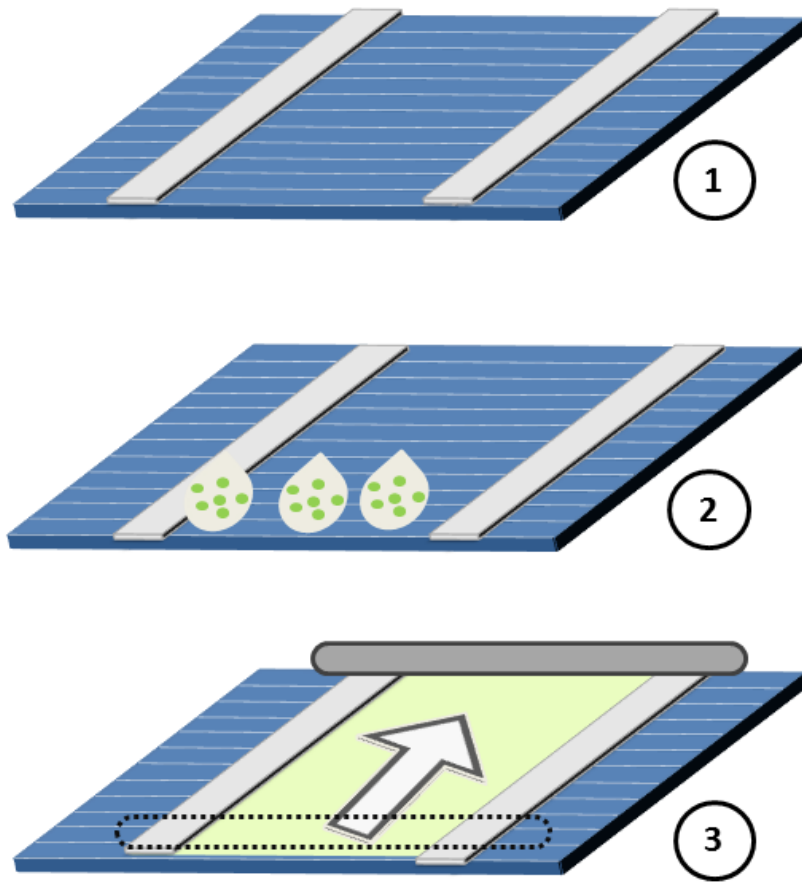


Figure 6.10: Doctor blade screen printing technique.

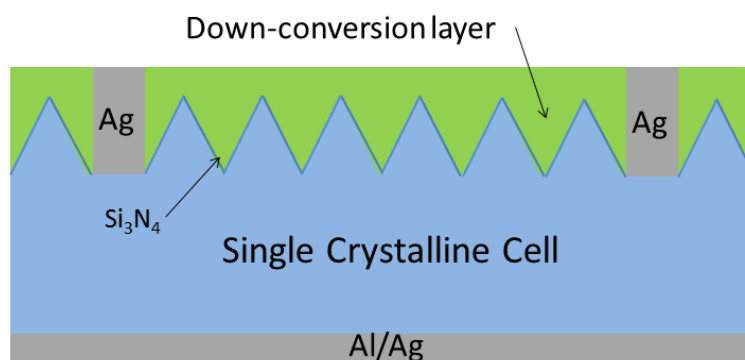


Figure 6.11: A schematic of the textured mono-crystalline solar cell with DC layer.

6.5 Results and Discussion

6.5.1 EVA Layer

DSC measurement was used to find the required temperature and time for curing the EVA sheet. Figure 6.12 shows DSC measurements of the raw EVA material.

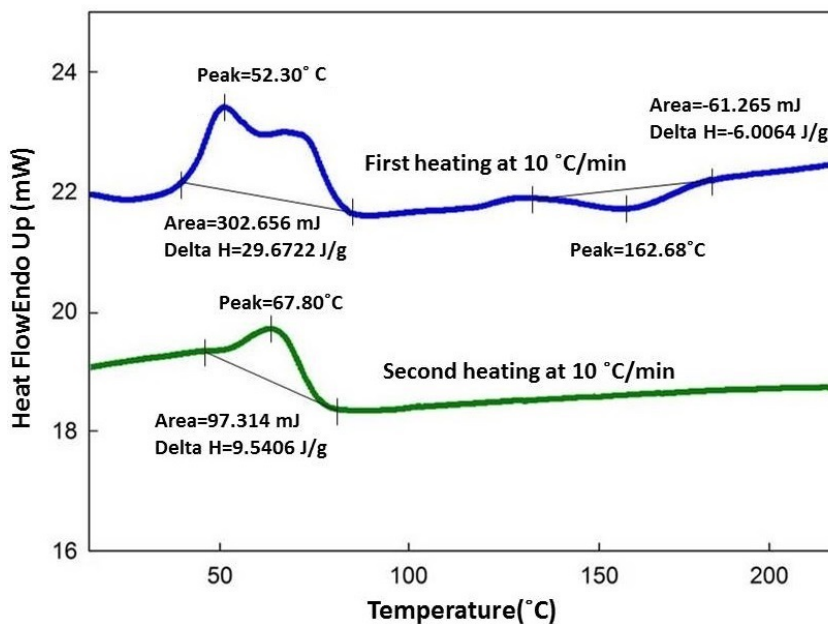


Figure 6.12: The first (blue) and second (green) heating curve of raw EVA material.

The first heating curve, highlighted in blue, shows an endothermic melting peak 29.67 J/g preceded by the exothermic curing peak with the curing enthalpy of 6 J/g. The second heating curve, highlighted in green, shows a smaller melting peak (9.54 J/g vs. 29.67 J/g), and there is no noticeable curing exothermal peak. Therefore, by comparing the first heating curve with the second heating curve, it can be seen clearly that EVA raw material is cured completely after first heating to 220 °C.

Figure 6.13 shows transmission spectra of the EVA layers dissolved in P-Xylene after the heating process. It can be seen that EVA layers were dissolved in the solvent with the concentrations 6, 10, 14, 18 wt% have excellent transmission properties in comparison to the glass substrate. The weight percentage (wt%) is calculated using

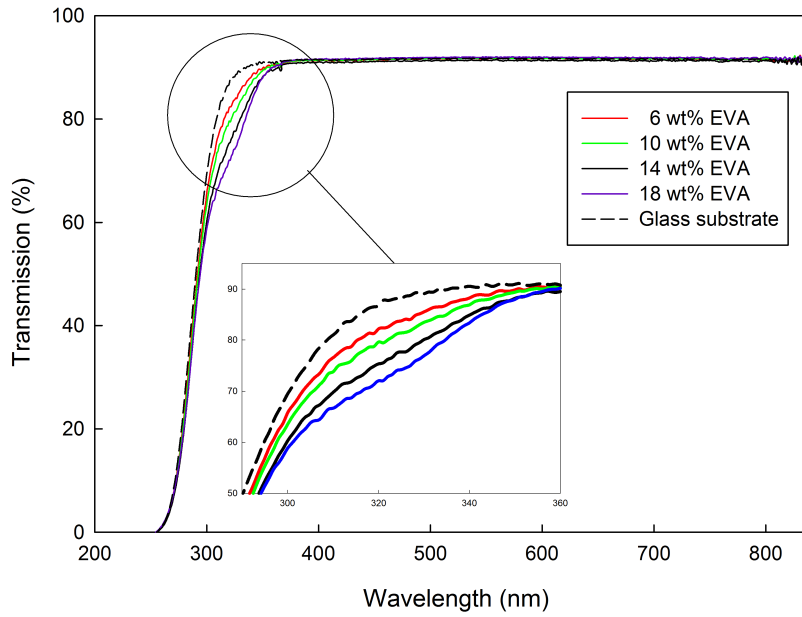


Figure 6.13: Transmission spectra for EVA layers dissolved in different concentrations of the solvent.

the Equation 6.1 where the mass of the polymer (EVA) is fixed, and the values 6, 10, 14, 18 wt% are obtained by varying the mass of the solvent. Since the height of the guides and the coating procedures are similar for the produced layers, it means the higher the values of the weight percentages, the more EVA content in the produced layer is obtained. Therefore, the layer contains more additives such as curing agent, UV stabiliser, antioxidant and adhesion promoter which result in a decrease in the transmission as shown in the zoom in the wavelength band of (300-360) nm at the knee of the transmission curves in Figure 6.13. The curve shows the transmission spectrum of the glass substrate which has the highest transmission value. The coated substrates with different wt% of the binder exhibit an excellent transmission with properties similar to the glass substrate except the range from 300 to 360 nm where the decrease of the transmission spectra of the layer corresponds to the increased contents of the additives.

$$\frac{\text{Mass of polymer}}{\text{Mass of polymer}(g) + \text{Mass of Solvent}(g)} = \%wt \text{ of the polymer} \quad (6.1)$$

Figure 6.14 shows the reflection spectra of the uncoated cell and coated cells with EVA layers. Solar cells coated with EVA layers shows a significant reduction in the reflection spectra in comparison to reflection spectrum of the uncoated solar cell over the measured range. The decrease in the reflection is due to enhancing the trapping properties of the light on the solar cells due to the addition of EVA layer.

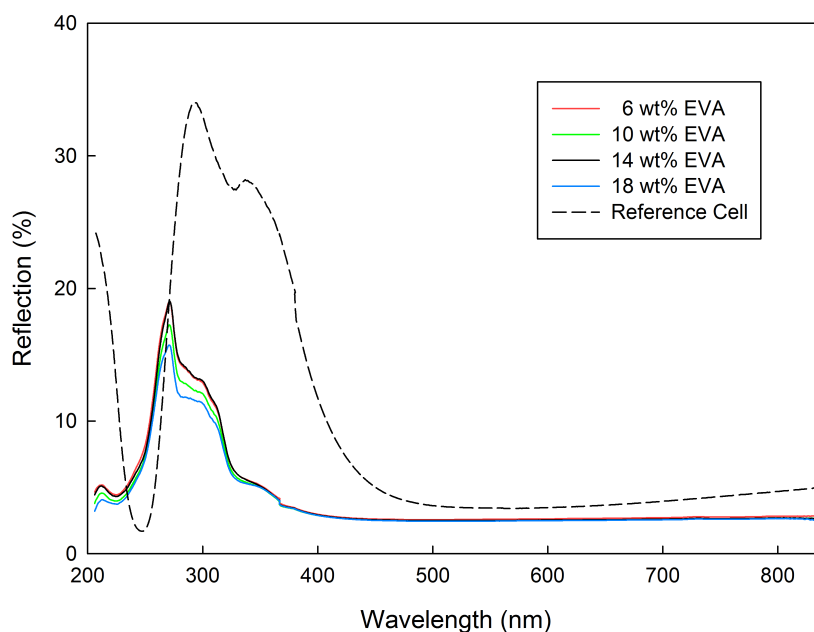


Figure 6.14: Reflection spectra for EVA layers dissolved in different concentrations of the solvent.

Figure 6.15 shows a photograph of the crystalline solar cell with an uncoated and coated part with EVA. Also, the influence of EVA coating on the electrical characteristics of the solar cell before and after heating is shown in the I-V curve. Before heating, it can be seen that the electrical performance of the coated cell is lower after the coating process. The effect of adding an uncured EVA layer is similar to the shading effects on the I-V curve of the solar cell due to reduced transparency. However, it can be seen that cured EVA layer through the heating process enhanced the electrical performance of the solar cell due the improved optical properties of the layer as shown earlier in Figures 6.14 and 6.13.

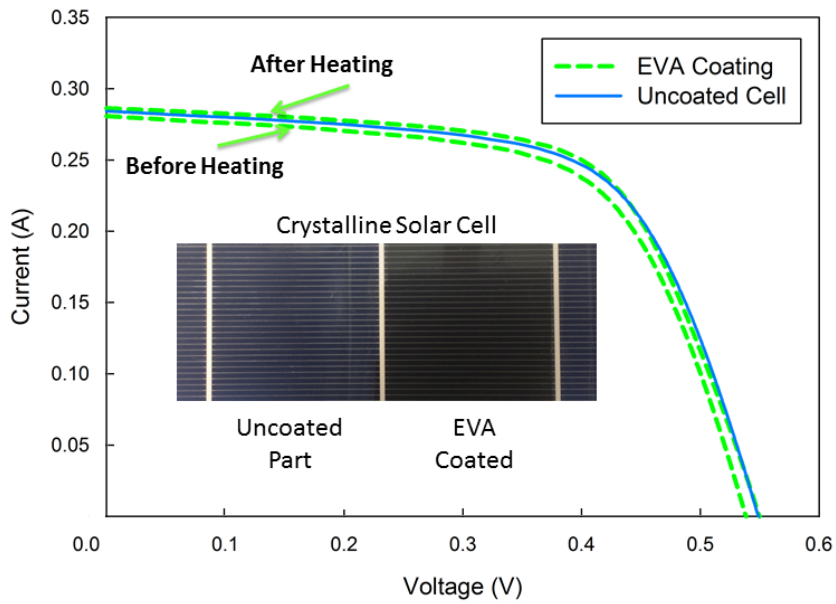


Figure 6.15: I-V curve of EVA coating before and after heat treatment at the illuminated surface area of 8.544 cm^2 , 1000 W/m^2 and $25 \text{ }^\circ\text{C}$.

6.5.2 EVA/Phosphor Layer

6.5.2.1 Optical Properties

Figure 6.16 shows and compares the reflectance spectra of the uncoated, EVA coated and EVA+phosphor coated solar cells. Comparison between these cells indicates that phosphor coating on the surface of the Si wafer can effectively reduce reflection and increase light absorption in the entire range from 200 to 800 nm. The coated cells show a significant reduction in the reflectance in the UV range.

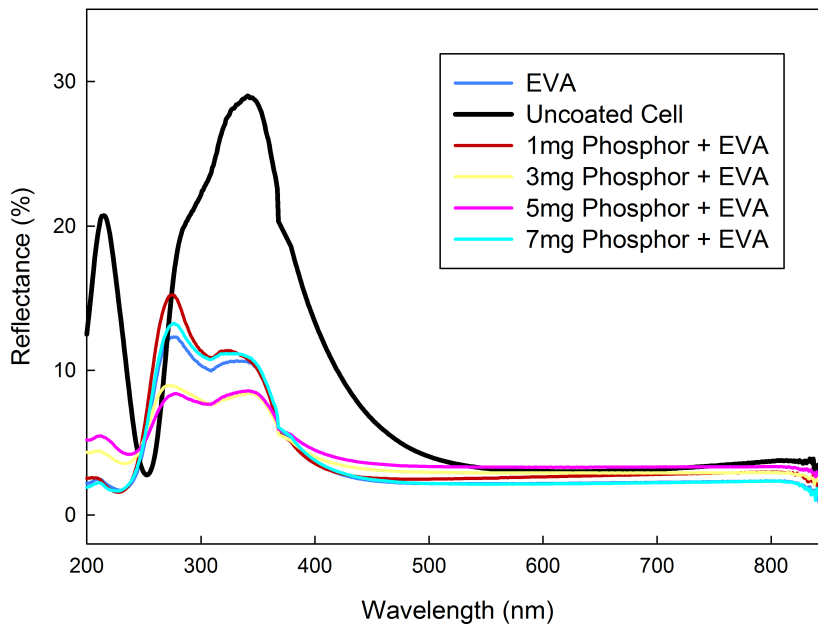


Figure 6.16: Comparison of reflectance spectra for uncoated and coated cells.

6.5.2.2 Electrical Characteristics

Figure 6.17 shows the current versus voltage I-V curves and the power versus voltage P-V curves for the solar cell before and after coating at the maximum enhanced conversion efficiency obtained. It can be seen that the I_{sc} has been increased from 280 to 289 mA due to light spectral conversion without any significant change in the open circuit voltage value. The enhancement in I_{sc} resulted in increasing the conversion efficiency from 12.11% to 12.65%. Detailed I-V characteristics of the coated solar cells are summarised in Table 6.3. It can be seen that the coating contributed to enhancing the efficiency of the cells. By comparing the performances of the uncoated, EVA and phosphor coating with different percentages, the enhancement brought by EVA through reducing anti-reflection loss could be obtained.

Also, the results show that enhancement brought by phosphor coating with different percentages in a polymeric matrix can be also achieved. These enhancements are shown in Figure 6.18 in which the efficiency enhancement brought by EVA, 1 mg, 3 mg, 5 mg, 7 mg is 0.23%, 0.41%, 0.54%, 0.28% and 0.18% respectively. As mentioned

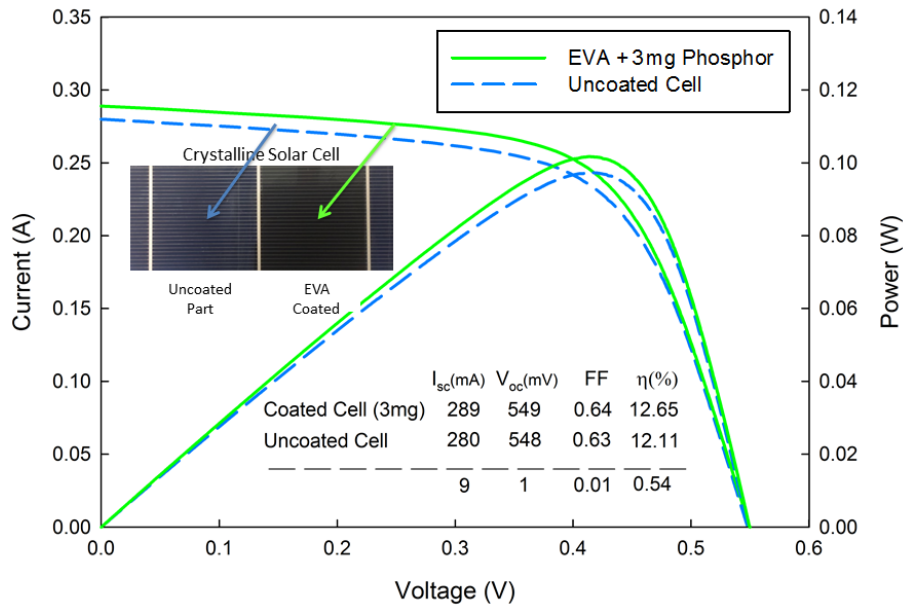


Figure 6.17: I-V and P-V curves of the solar cells at the maximum enhancement at the illuminated surface area of 8.544 cm^2 , 1000 W/m^2 and $25 \text{ }^\circ\text{C}$.

Table 6.3: Electrical characteristics of the uncoated and coated cells at the illuminated surface area of 8.544 cm^2 , 1000 W/m^2 and $25 \text{ }^\circ\text{C}$.

Cell Type	I_{sc} mA	V_{oc} mV	P_{max} mW	FF –	η %
Uncoated	0.280	0.548	0.0973	0.63	12.11
EVA	0.284	0.549	0.0992	0.64	12.34
Uncoated	0.280	0.548	0.0968	0.63	12.08
1 mg phosphor + EVA	0.286	0.549	0.1006	0.64	12.52
Uncoated	0.280	0.548	0.0969	0.63	12.07
3 mg Phosphor + EVA	0.289	0.549	0.1017	0.64	12.65
Uncoated	0.280	0.548	0.0968	0.63	12.07
5 mg Phosphor + EVA	0.286	0.548	0.0968	0.64	12.39
Uncoated	0.280	0.548	0.0969	0.63	12.06
7 mg Phosphor + EVA	0.281	0.548	0.0988	0.64	12.29

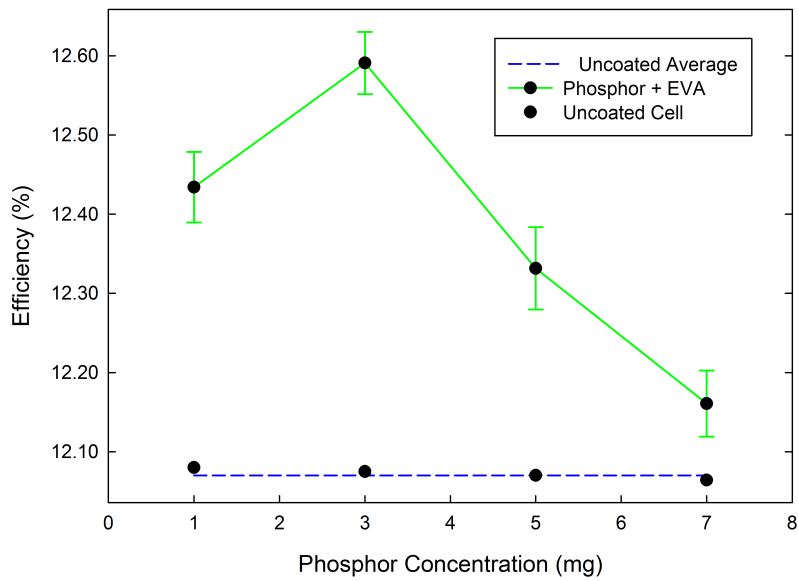


Figure 6.18: Efficiency enhancement of the coated solar cells.

before the enhancement achieved by luminescent layer consists of two parts. One part is enhancement brought by anti-reflection effects of the EVA layer and the other part is the enhancement brought by the photo-luminescent effects of the phosphor powder. Therefore, by comparing improvement brought by EVA and EVA with the phosphor coating, the increase produced by down conversion effect of the luminescent layers can be obtained. For phosphor coating with 3 mg, this absolute efficiency enhancement is +0.54% which corresponds to 4.45% relative efficiency increase.

To further verify the experimental results, transmission analysis of the coated layers was investigated by coating a quartz and glass substrates using the same condition used for coating the solar cells.

Figure 6.19 shows the transmission of the EVA and EVA with different phosphor concentration layers. It can be seen that the EVA coating has the highest transmittance. Transmission spectra of the coated substrates show a decrease in the transmission with increased concentration of the phosphor powder. The later explains the reduction in the I_{sc} and thus lower conversion efficiency. The Figure shows the effects of using different substrates for the transmission of the layer. Quartz substrates

have a better transmission in comparison to the glass substrates as well as the optical cut-off wavelength goes down to 220 nm where the optical cut-off wavelength of the glass substrate goes down to 270 nm. Thus, coated quartz substrates show better optical properties in comparison to the coated glass ones. It should be noted that the electrical characteristics were carried out without a glass or quartz cover. However, in real life operation of photovoltaic solar panels, solar cells are encapsulated in a glass cover. Therefore, the optical characteristics of the solar panel will be influenced by the optical properties of the glass cover.

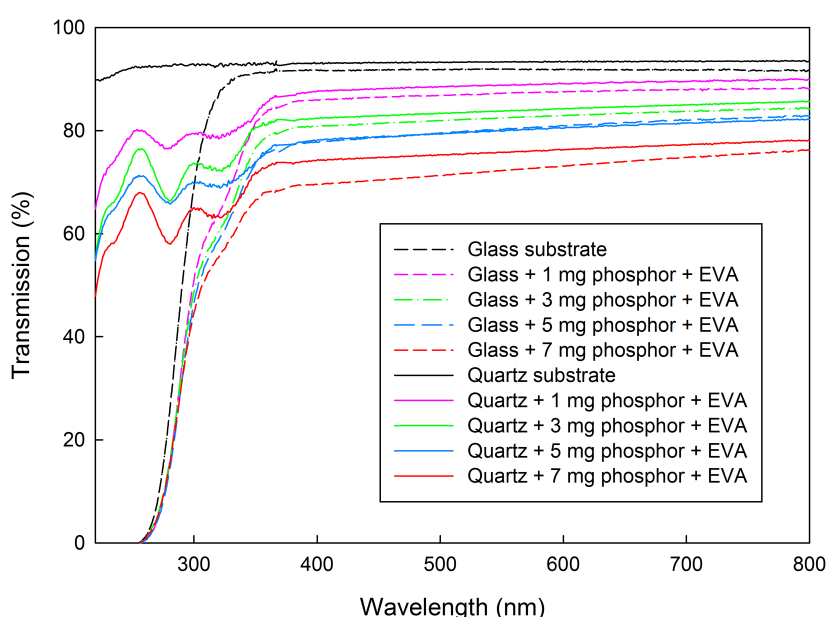


Figure 6.19: Transmission spectra of the Phosphor+EVA layers.

Figure 6.20 shows the absorption spectra of the quartz substrate and quartz substrates coated with different percentages of the phosphor material. It can be seen from the graph that the absorption of the layers increases with the increased concentration of the phosphor powder in the layer. Absorption spectra correspond to the layers are in good agreements with the transmission spectra reported in Figure 6.19.

Figure 6.21 shows the temperature coefficient of the uncoated cell, EVA coated and Phosphor+EVA coated solar cell. It can be seen from the figure the drop of the

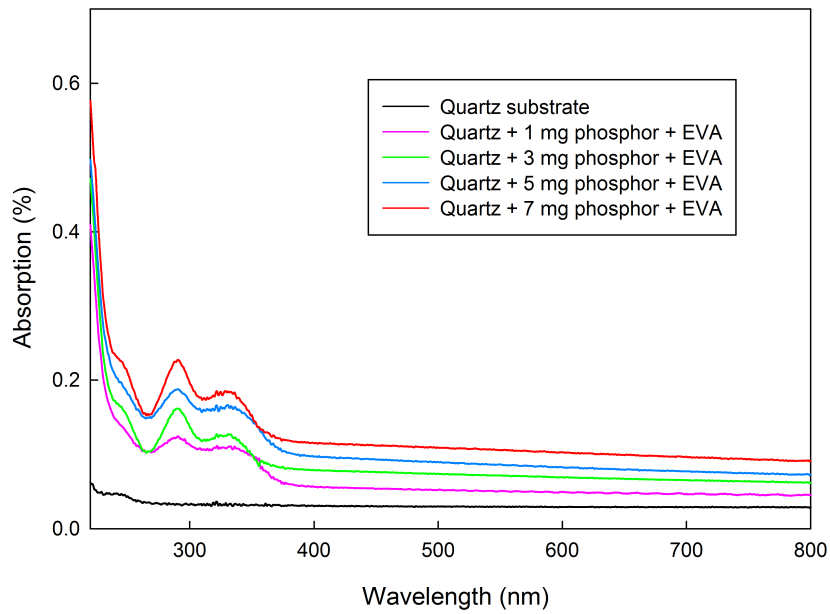


Figure 6.20: Absorption spectra of the Phosphor+EVA layers.

open circuit voltage of the solar cells with increasing temperature of the solar cell.

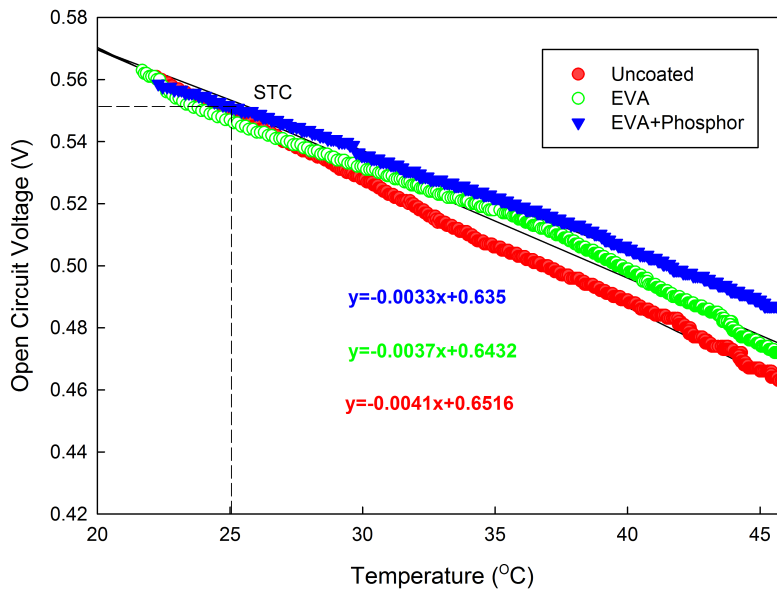


Figure 6.21: Temperature coefficient of solar cells.

The internal quantum efficiency of the uncoated cell, EVA coated, and EVA doped with different concentrations of the phosphor were measured and shown in Figure 6.22 in order to obtain the optimum concentration of the phosphor in EVA

layer.

By comparing the spectra of the EVA coated cell and the phosphor incorporated into the EVA with different concentrations, an enhancement of the conversion efficiency can be detected in the spectral region corresponding to the absorption of the phosphor material incorporated in the EVA film. The increase in the concentration of the phosphor corresponds to the increase in the magnitude of IQE spectra in the UV region.

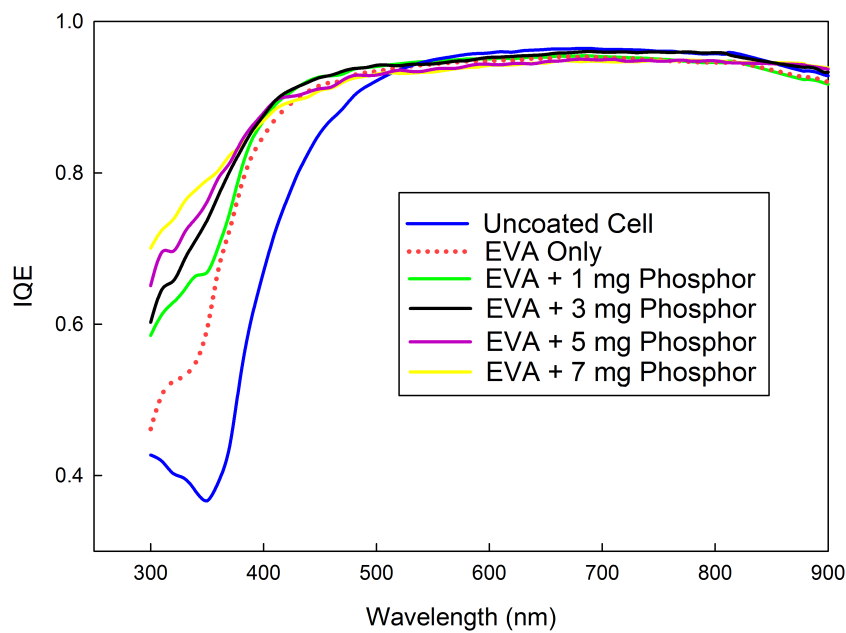


Figure 6.22: IQE spectra of the solar cells.

From IQE spectra, it can be seen that 1 and 3 mg concentrations provide with a good response in the visible region. However, it can be concluded that 3mg is the best concentration where it shows to absorb more photons in the UV region. These results also confirm the improvement in the solar cell performance by the conversion from the short wavelengths where the reduction in reflection was found to correspond to an increase in the short circuit current of the solar cells. However, by comparing 5 and 7 mg concentration of the phosphor and EVA coated solar cells with the uncoated solar cell, it can be seen an insignificant decrease in the visible light response of the solar

cell. This decrease in visible light response could be expected to be greater with that a higher concentration of the phosphor in the powder because the phosphor aggregate at high concentration leads poor film quality due to low transparency because of light scattering.

6.5.3 Microstructure of the Phosphor-Coated Solar Cell

Figure 6.23 shows cross-section SEM image of the solar cell coated using doctor blade screen printing technique. The image shows the good uniformity of the deposited luminescent layer with a thickness of $9.3 \mu\text{m}$ on top of a pyramidally textured surface of the silicon solar cell.

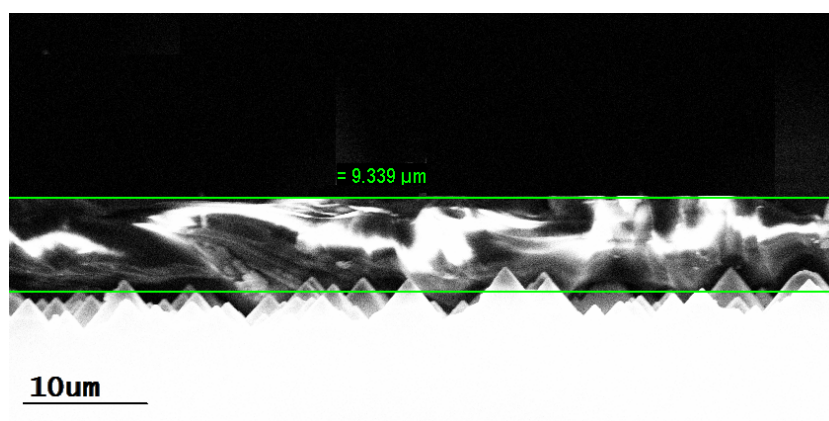


Figure 6.23: Cross section SEM image of the coated cell with EVA+phosphor.

Figure 6.24 shows low magnification SEM image in backscattered mode of the top surface of the photo-luminescent layer with 3 mg of the phosphor. The top image of coating layer exhibits a granular feature due to phosphor particles. EDX results confirmed the presence and composition of the phosphor nano-powder.

The granular feature of the top image is in good agreement with the results obtained by Chen et al. [137]. However, the obtained results look very similar to the tops of the random pyramids. To confirm that the obtained structure is due to the phosphor and not because of the pyramidal structure of the top surface of the silicon

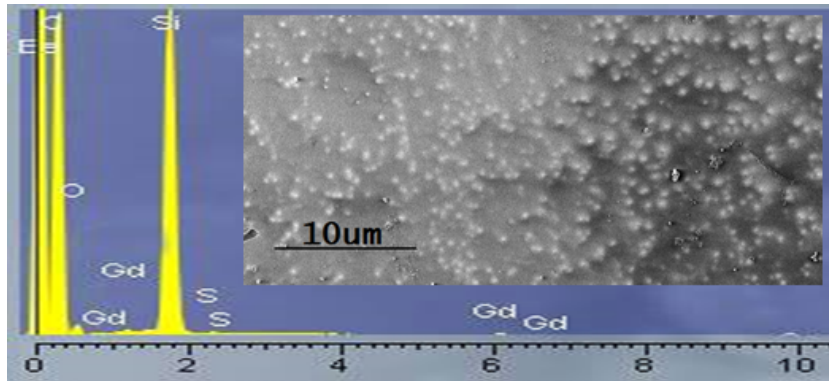


Figure 6.24: EDX spectrum and top SEM image of the coated solar cell with EVA and phosphor.

cell, surface analysis using EDX of two silicon solar cells were tested. One cell is coated with EVA only while the other is coated with EVA and phosphor with a concentration of 3 mg. The coating was carried out with the similar coating conditions to obtain the same thickness for both coated cells. The granular feature was not detected in the

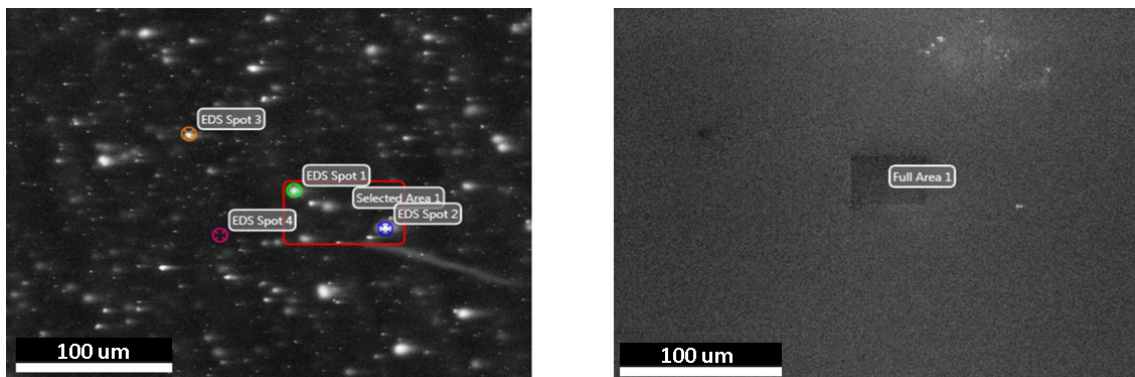


Figure 6.25: EDX images of the EVA + Phosphor (left) and EVA (right) coated cell.

solar cell coated with EVA only even at high magnification whereas it is noticeable in the other sample coated with phosphor and EVA. This was confirmed by the results of the selected areas on both cells shown in Table 6.4 where the selected area shows the presence of Gadolinium only in the sample coated with phosphor and EVA and it not detected in the other sample. Furthermore, when selecting the granular feature (S_1 , S_2 , S_3) of the coated cell gadolinium feature was presented while when selecting a black spot as in S_4 gadolinium was not detected.

Table 6.4: Values of the EDX spectra of the coated silicon solar cells with EVA+phosphor and EVA only.

Sample		C	Gd	O	Si	Total
EVA+Phosphor	S ₁	86.31	10.11	2.50	1.08	100
	S ₂	86.77	9.41	3.19	0.63	100
	S ₃	87.04	9.57	2.67	0.72	100
	S ₄	85.96	–	10.38	3.66	100
	A	82.52	1.07	13.13	3.11	100
EVA	A	85.88	–	11.41	2.71	100

All results shown in the table are in weight %, S refer to selected Spot and A to Area.

In general, it can be seen from EDX analysis a presence of Si due to the silicon substrate of the solar cell, Carbon presence is due to EVA binder, Oxygen due to heat treatment of the binder and gadolinium due to the phosphor. It can be seen in the analysis that Terbium and Erbium are not detected as their concentration in the phosphor encapsulated in EVA binder is below the detection limit for EDAX which is between 0.2-0.5 %(w/w).

6.5.4 Combined EVA/Phosphor/Silicon Oxide layer

This section presents the results of combining silicon oxide film together with the phosphor layer. Solar cells were coated with two layers consist of a layer of silicon oxide and a layer of a composite of EVA and Gadolinium Oxysulfide doped with erbium and terbium as shown in the schematic in Figure 6.26. Solar cells were coated with silicon oxide film with the condition in which the optimum enhancement was obtained for solar cells with a single layer of silicon oxide with coating conditions of (Bias voltage 100V, 15 minutes deposition time, TMS flow rate of 25 (cm³/min) and 20 g of the KMnO₄ oxidising agent). The second layer of the luminescent composite layer is produced under the same conditions as outlined in this chapter.

This design allows the use of silicon oxide which has excellent anti-reflection properties and a layer of the luminescent phosphor for solar cell enhancement. The

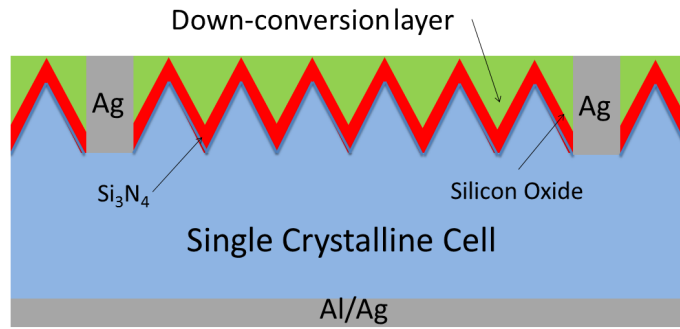


Figure 6.26: A schematic of the textured mono-crystalline solar cell with SiO_2 and DC layers.

luminescent layer plays a part in modifying the solar spectrum in which UV and visible light photons are converted into less energetic photons that can be utilised into a useful energy by the solar cell while the silicon oxide layer could play a part in further reducing the reflection of silicon solar cells.

This design is shown potential for efficiency improvement of crystalline silicon solar by a recent study by Yang et al. who used the combination of europium doped silicate phosphors downshifting and SiO_2 anti-reflective coating. The authors demonstrated an absolute enhancement of two percent in the conversion efficiency of the solar cell [157].

Figure 6.27 shows transmission and absorption spectra of the layer of EVA and phosphor (3 mg) and layer of EVA, phosphor (3 mg) and SiO_2 . The results showed a similar tendency to the results obtained for solar cells coated with a composite of EVA and phosphor. It can be seen from the figure a reduction in the transmission of the layer of EVA+phosphor+ SiO_2 in comparison to the EVA+phosphor layer due to an increase in the absorption in the coating containing SiO_2 as shown in the absorption spectra.

Figure 6.28 shows the conversion efficiency of the solar coated with EVA+phosphor on a monocrystalline solar cell coated with a layer of SiO_2 at different concentrations of the phosphor. The parameters of the solar cells are presented in Table 6.5. It

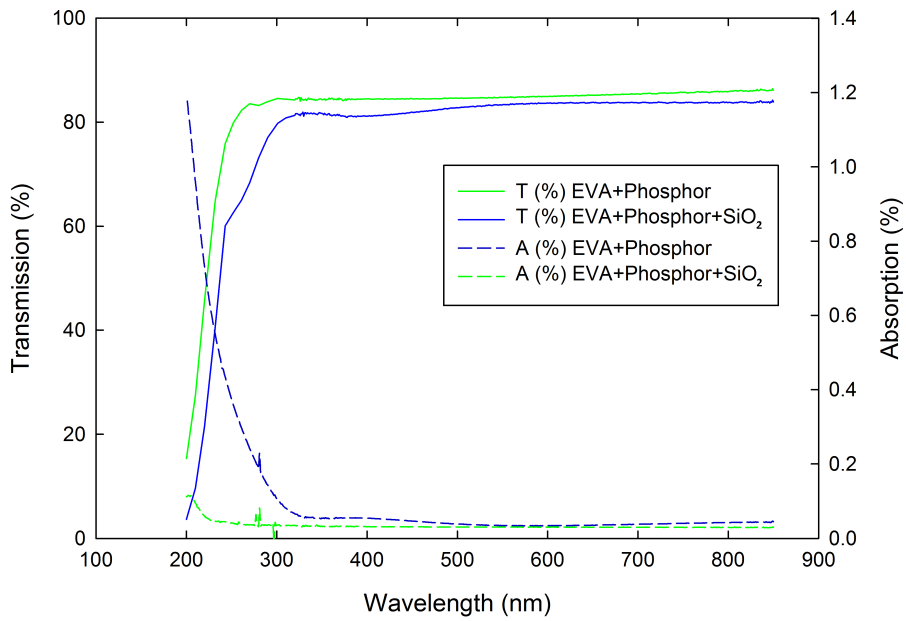


Figure 6.27: Transmission and absorption spectra of the layers.

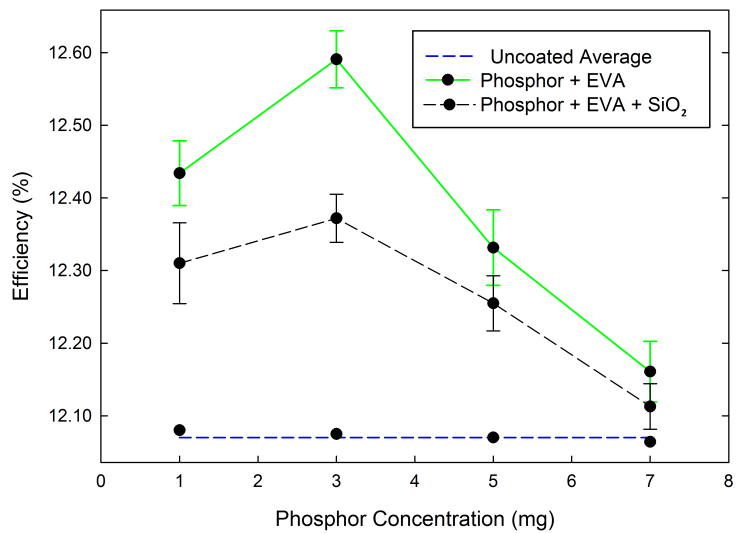


Figure 6.28: Conversion efficiency of the solar cells.

Table 6.5: Electrical characteristics of the uncoated and coated cells at the illuminated surface area of 8.544 cm², 1000 W/m² and 25 °C.

Cell Type	Isc A	Voc V	Pmax W	FF –	η %
Uncoated	0.2991	0.548	0.10328	0.63	12.080
1 mg phosphor + EVA + SiO ₂	0.3079	0.548	0.10631	0.63	12.434
Uncoated	0.2990	0.548	0.10324	0.63	12.075
3 mg Phosphor + EVA + SiO ₂	0.3117	0.548	0.10764	0.63	12.590
Uncoated	0.2989	0.548	0.10319	0.63	12.070
5 mg Phosphor + EVA + SiO ₂	0.3054	0.548	0.10543	0.63	12.332
Uncoated	0.2987	0.548	0.10314	0.63	12.064
7 mg Phosphor + EVA + SiO ₂	0.3011	0.548	0.10397	0.63	12.161

can be seen an increase in the conversion efficiency of the coated solar cells with an EVA+phosphor+SiO₂ layers in comparison to the uncoated ones. The optimum concentration was found with a concentration of 3 mg of the phosphor. The efficiency curve shows a similar tendency to the earlier reported curve for the solar cells coated with a composite of EVA+phosphor. However, a reduction in the conversion efficiency of the solar cells was obtained by adding a layer of silicon oxide in comparison to the obtained efficiency using the luminescent layer of the phosphor and EVA.

6.6 Conclusion

This chapter demonstrated the possibility of enhancing the performance of commercial PV cell by using spectral conversion by applying a phosphor material dispersed in a polymeric matrix on top of mono-crystalline solar cells.

Blade screen printing technique formed a layer with a good uniformity, and this method can apply to other powder phosphors. The results demonstrated that the coating can effectively increase the values of the short circuit current and consequently the conversion efficiency.

A relative enhancement of 4.45% has been demonstrated in this study. The photo-luminescent layer did not serve only as a spectral conversion layer for one part of the solar spectrum but also as a low reflective layer for a different part of the solar spectrum. Thus, it can be concluded that the enhancement in the conversion efficiency is due to the effects of the properties of EVA binder and the phosphor and the top surface structure of the silicon solar cell.

The design of double layers of the luminescent composite and silicon oxide showed a deterioration in the improvement in the energy conversion efficiency of solar cells in comparison to the luminescent composite coating.

The same method can be optimised and extended to a spectral range more suitable for PV application by tuning the absorption and emission of the phosphor into more desirable wavelengths.

Chapter 7

Conclusions and Future Work

The primary goal of this research is to investigate the application of oxide coatings on the performance of crystalline silicon solar cells. The investigated oxide layers were silicon oxide, titanium oxide and gadolinium oxysulfide doped with terbium and erbium. A considerable motivation in this study is to avoid the use of a silane, as it is toxic and pyrophoric and thus provides a safer alternative way of delivering the passivation coating that can be employed in the preparation of silicon solar cells.

Oxide coatings for solar cells were applied successfully using various techniques in this study. PECVD technique is used for deposition of silicon oxide layers. Sputtering which is part of PVD technique is used for the deposition of titanium films. Doctor-blade-screen-printing method is used for applying the luminescent layer. Furthermore, the oxide layers are deposited without substrate heating as heat treatment at high temperatures in silicon solar cells processes could introduce defects into the silicon solar cell, which offers a significant advantage for solar cells manufacturing; and would be a key driver for successful implementation in the c-Si solar cell manufacturing industry.

Silicon solar cells coated with silicon oxide films can reduce reflection from the silicon surface and contribute to the increase of the conversion energy of the solar

cells on one hand while the variety of colours obtained in this study can be of great importance for building integrated photovoltaic application on the other hand.

With optimised oxygen diffusion in the silicon films for solar cells coated with a single layer of silicon oxide can yield a competitive electrical conversion efficiency in comparison to a double layer of silicon oxide coating. Also, double ARC is more flexible to modulate colours while maintaining good passivation quality. Various coloured mono-crystalline silicon solar cells were obtained by depositing an additional layer of silicon oxide with better performance can be achieved in comparison to uncoated cells where the solar cells showed a relative enhancement of about 3% in the conversion efficiency.

The majority of commercially available monocrystalline solar cells in the market are of either dark-blue or black colour, and this can be an aesthetical disadvantage of PV products. When solar cells are colourful, more aesthetically pleasing PV devices are an option, and can play a significant part in boosting its integration in the market or any other application such as PV for electrical vehicles. Therefore, the work on the silicon oxide can be extended to produce more colourful solar cells.

Titanium layers were deposited using two different configurations of the sputtering techniques, namely DC and RF sputtering. Deposited titanium films oxidised in the plasma using the KMnO_4 oxidising agent did not yield competitive results in comparison to the thermal oxidation method. In this chapter, the effects of a single layer of titanium oxide and double layers of titanium oxide and silicon oxide on the performance of silicon solar cells were studied. Titania nanoparticles produced by HTSD method for energy band-gap comparison study in Chapter 5 could find application for dye-sensitised solar cells (DSSCs). Since titania nanoparticles are stable, nontoxic and have a relatively high transmittance in the visible spectrum. The anatase phase is favoured due to its excellent photocatalytic properties and wide direct band gap. Therefore, it becomes a promising nanoparticle material for applications in DSSCs.

The best results of the application of oxide layers in this thesis were obtained by applying phosphor coating of the solar cells. A relative enhancement of 4.45% has been demonstrated in this study. The design of double layers of the luminescent composite and silicon oxide showed a deterioration in the improvement in the energy conversion efficiency of solar cells in comparison to the luminescent composite coating.

The overall benefit in short circuit current and conversion efficiency that has been achieved in this thesis is rather small for mono-crystalline silicon PV cells. The efficiency of the commercial PV modules is progressively boosted by improving the optoelectronic properties of solar cells at production scale. Adopting the used techniques thesis at commercial production scale would add a little to the current conversion efficiency. However, such an action could be based on environmental considerations rather than efficiency enhancement due to safety consideration of using silane gas as silicon precursor or toxicity of cadmium used in luminescent materials in the which are highly in use in the production process.

Blade screen printing technique formed a good photo-luminescent layer which did not serve only as a spectral conversion layer for one part of the solar spectrum but also as a low reflective layer for a different part of the solar spectrum. Films produced by doctor blade screen printing technique in the experimental work used a single type of the guides for comparison purposes for the effects of phosphor concentration on the performance of the solar cell. A variety of thicknesses of the luminescent layer can be obtained by using guides with different heights. Also, this deposition techniques could be improved to produce different shapes and sizes of the luminescent layer to meet the requirements of BIPV.

An interesting avenue for future work is to explore new photo-luminescent materials for up-conversion. Since the up-conversion layer is placed at the bottom of the solar cells, it has the advantages of avoiding forming a barrier to the incident light on the top surface of the solar cell. Spectral conversion is a promising option

to overcome the existing weaknesses of commercial silicon PV solar cells. Therefore, it attracts scientists and engineers continuously to improve the solar cells efficiency beyond the theoretical limit. Suitability, availability and prices of the luminescent material can be the most challenging factor in the application of luminescent layers to the PV solar cells. It is expected that a significant breakthrough of implementation luminescent materials for solar cells may come through the development of rare-earth ion complexes. This could be acquired by developing materials with an expanded absorption band of un-utilised part of the solar spectrum by the solar cell and an emission to desirable wavelengths were the solar cells show a better response. Spectral conversion is associated with modifying the solar spectrum and not the structure of the solar cells. Thus, the effects of the luminescent layer can not be limited to mono-crystalline solar cells and it can find applications in other PV technology.

Since phosphor serves as spectral conversion layer in which converts parts of UV light to visible light, it is expected that phosphor coating would reduce the EVA degradation due to UV light exposure. Therefore, this could be investigated and add a significant value of doping EVA with luminescent species.

Commercial solar panels come with a 25 year as standard. Therefore, it is important to conduct environmental testing by an outdoor installation of silicon solar cells with the deposited materials to observe their durability for the implementation in the photovoltaic market.

References

- [1] Institution of Mechanical Engineers. When will oil run out?, 2015. [Accessed Online on 27 August 2015 from; <http://www.imeche.org/knowledge/themes/energy/energy-supply/fossil-energy/when-will-oil-run-out>].
- [2] Chetan Singh Solanki. *Solar photovoltaics: fundamentals, technologies and applications*. PHI Learning Pvt. Ltd., 2011.
- [3] Les Coleman. Explaining crude oil prices using fundamental measures. *Energy Policy*, 40:318–324, 2012.
- [4] Henrik Lund and Brian Vad Mathiesen. Energy system analysis of 100% renewable energy systemsthe case of denmark in years 2030 and 2050. *Energy*, 34(5):524–531, 2009.
- [5] M van der Hoeven. *Solar energy perspectives*, 2011.
- [6] Furkan Dincer. The analysis on photovoltaic electricity generation status, potential and policies of the leading countries in solar energy. *Renewable and Sustainable Energy Reviews*, 15(1):713–720, 2011.
- [7] B Burger, K Kiefer, C Kost, S Nold, S Philipps, R Preu, R Schindler, T Schlegl, G Stryl-Hipp, G Willeke, et al. Photovoltaics report. *Fraunhofer Institute for Solar Energy Systems ISE, Freiburg (Germany)*, pages 1–42, 2014.
- [8] ASTM Standard. G173, standard tables for reference solar spectral irradiances: Direct normal and hemispherical on 37 tilted surface. *Annual book of ASTM standards*, 12, 2008.
- [9] Greg P Smestad. *Optoelectronics of solar cells*. SPIE press, 2002.
- [10] Martin A Green. *Solar cells: operating principles, technology, and system applications*. 1982.
- [11] Jean-Claude G Bünzli and Anne-Sophie Chauvin. *Lanthanides in solar energy conversion*. Technical report, Elsevier, 2014.
- [12] Energyplus. Weather data. [Accessed Online on 23 December 2015 from; http://apps1.eere.energy.gov/buildings/energyplus/weatherdata_about.cfm].

- [13] PVGIS. Photovoltaic geographical information system-solar irradiation data. [Accessed Online on 11 February 2015 from; <http://re.jrc.ec.europa.eu/pvgis/solres/solreurope.htm>].
- [14] John A. Duffie and William A. Beckman. *Solar engineering of thermal processes*. Wiley, fourth edition, 2013.
- [15] Ali Mohammad Noorian, Isaac Moradi, and Gholam Ali Kamali. Evaluation of 12 models to estimate hourly diffuse irradiation on inclined surfaces. *Renewable energy*, 33(6):1406–1412, 2008.
- [16] James Allan. *The Development and Characterisation of Enhanced Hybrid Solar Photovoltaic Thermal Systems*. PhD thesis, Department of Mechanical, Aerospace and Civil Engineering, College of Engineering, Design and Physical Sciences, Brunel University, 2016.
- [17] Bjørn Petter Jelle, Christer Breivik, and Hilde Drolsum Røkenes. Building integrated photovoltaic products: A state-of-the-art review and future research opportunities. *Solar Energy Materials and Solar Cells*, 100:69–96, 2012.
- [18] AF Sherwani, JA Usmani, et al. Life cycle assessment of solar pv based electricity generation systems: A review. *Renewable and Sustainable Energy Reviews*, 14(1):540–544, 2010.
- [19] Martin A Green, Keith Emery, Yoshihiro Hishikawa, Wilhelm Warta, and Ewan D Dunlop. Solar cell efficiency tables (version 45). *Progress in photovoltaics: research and applications*, 23(1):1–9, 2015.
- [20] NREL. Research Cell Efficiency Records. http://www.nrel.gov/ncpv/images/efficiency_chart.jpg, 2016. [Online; accessed 19-July-2008].
- [21] AL Fahrenbruch and RH Bube. Fundamentals of solar cells (academic, new york, 1983). *Chap*, 6:234–236.
- [22] Martin A Green. Photovoltaic principles. *Physica E: Low-dimensional Systems and Nanostructures*, 14(1):11–17, 2002.
- [23] Nadja Rebecca Brun, Bernhard Wehrli, and Karl Fent. Ecotoxicological assessment of solar cell leachates: Copper indium gallium selenide (cigs) cells show higher activity than organic photovoltaic (opv) cells. *Science of the Total Environment*, 543:703–714, 2016.
- [24] Varun Sivaram, Samuel D Stranks, and Henry J Snaith. Outshining silicon. *Scientific American*, 313(1):54–59, 2015.
- [25] Charles H Henry. Limiting efficiencies of ideal single and multiple energy gap terrestrial solar cells. *Journal of applied physics*, 51(8):4494–4500, 1980.
- [26] F Dimroth, C Baur, AW Bett, M Meusel, and G Strobl. 3-6 junction photovoltaic cells for space and terrestrial concentrator applications. In *Conference Record of the Thirty-first IEEE Photovoltaic Specialists Conference, 2005.*, pages 525–529. IEEE, 2005.

- [27] Ingrid Repins, Miguel A Contreras, Brian Egaas, Clay DeHart, John Scharf, Craig L Perkins, Bobby To, and Rommel Noufi. 19· 9%-efficient zno/cds/cuingase2 solar cell with 81· 2% fill factor. *Progress in Photovoltaics: Research and applications*, 16(3):235–239, 2008.
- [28] Tom Markvart and Luis Castaner. *Solar cells: materials, manufacture and operation*. Elsevier, 2004.
- [29] Tetsuo Soga. *Nanostructured materials for solar energy conversion*. Elsevier, 2006.
- [30] Marco Ficcadenti and Roberto Murri. Basics of thin film solar cells. 2013.
- [31] Sameer Chhajed, Martin F Schubert, Jong Kyu Kim, and E Fred Schubert. Nanostructured multilayer graded-index antireflection coating for si solar cells with broadband and omnidirectional characteristics. *Applied Physics Letters*, 93(25):251108, 2008.
- [32] Jenny Nelson. *The physics of solar cells*, volume 1. World Scientific, 2003.
- [33] Afshin Izadian, Arash Pourtaherian, and Sarasadat Motahari. Basic model and governing equation of solar cells used in power and control applications. In *Proc. IEEE Energy Convers. Expo. Conf*, pages 1483–1488, 2012.
- [34] Cristina Cornaro and Angelo Andreotti. Influence of average photon energy index on solar irradiance characteristics and outdoor performance of photovoltaic modules. *Progress in Photovoltaics: Research and Applications*, 21(5):996–1003, 2013.
- [35] Claudia Strümpel, Michelle McCann, Guy Beaucarne, Vladimir Arkhipov, Abdelilah Slaoui, V Švrček, C Del Cañizo, and I Tobias. Modifying the solar spectrum to enhance silicon solar cell efficiency: an overview of available materials. *Solar Energy Materials and Solar Cells*, 91(4):238–249, 2007.
- [36] Thomas Huld, Gabi Friesen, Artur Skoczek, Robert P Kenny, Tony Sample, Michael Field, and Ewan D Dunlop. A power-rating model for crystalline silicon pv modules. *Solar Energy Materials and Solar Cells*, 95(12):3359–3369, 2011.
- [37] Michael Koehl, Markus Heck, Stefan Wiesmeier, and Jochen Wirth. Modeling of the nominal operating cell temperature based on outdoor weathering. *Solar Energy Materials and Solar Cells*, 95(7):1638–1646, 2011.
- [38] N Martin and JM Ruiz. Calculation of the pv modules angular losses under field conditions by means of an analytical model. *Solar Energy Materials and Solar Cells*, 70(1):25–38, 2001.
- [39] Thomas Huld, Marcel Šúri, and Ewan D Dunlop. Comparison of potential solar electricity output from fixed-inclined and two-axis tracking photovoltaic modules in europe. *Progress in photovoltaics: Research and Applications*, 16(1):47–59, 2008.

- [40] Steven Magee. *Solar Irradiance and Insolation for Power Systems*. Steven Magee, 2010.
- [41] SM Sze. *Physics of semiconductors devices* 258, 1981.
- [42] Martin A Green. *Silicon solar cells: advanced principles & practice*. Centre for photovoltaic devices and systems, University of New South Wales, 1995.
- [43] HA Macleod. *Optical thin-film filters*, 1986.
- [44] J Carrillo-López, JA Luna-López, I Vivaldo-De la Cruz, M Aceves-Mijares, A Morales-Sanchez, and G García-Salgado. Uv enhancement of silicon solar cells using thin sro films. *Solar Energy Materials and Solar Cells*, 100:39–42, 2012.
- [45] William Shockley and Hans J Queisser. Detailed balance limit of efficiency of p-n junction solar cells. *Journal of applied physics*, 32(3):510–519, 1961.
- [46] Martin Wolf. A new look at silicon solar cell performance. *Energy Conversion*, 11(2):63–73, 1971.
- [47] Martin A Green. *Third generation photovoltaics*. Springer, 2006.
- [48] A Luque, A Martí, A Bett, VM Andreev, C Jaussaud, JAM Van Roosmalen, J Alonso, A Räuber, G Strobl, W Stolz, et al. Fullspectrum: a new pv wave making more efficient use of the solar spectrum. *Solar energy materials and solar cells*, 87(1):467–479, 2005.
- [49] Antonio Martí and Antonio Luque. *Next generation photovoltaics: high efficiency through full spectrum utilization*. CRC Press, 2003.
- [50] Y Okada, NJ Ekins-Daukes, T Kita, R Tamaki, M Yoshida, A Pusch, O Hess, CC Phillips, DJ Farrell, K Yoshida, et al. Intermediate band solar cells: Recent progress and future directions. *Applied Physics Reviews*, 2(2):021302, 2015.
- [51] Antonio Luque and Antonio Martí. Increasing the efficiency of ideal solar cells by photon induced transitions at intermediate levels. *Physical Review Letters*, 78(26):5014, 1997.
- [52] Matthew C Beard, Joseph M Luther, Octavi E Semonin, and Arthur J Nozik. Third generation photovoltaics based on multiple exciton generation in quantum confined semiconductors. *Accounts of chemical research*, 46(6):1252–1260, 2012.
- [53] Victor I Klimov, Sergei A Ivanov, Jagjit Nanda, Marc Achermann, Ilya Bezel, John A McGuire, and Andrei Piryatinski. Single-exciton optical gain in semiconductor nanocrystals. *Nature*, 447(7143):441–446, 2007.
- [54] Daniel C Law, RR King, H Yoon, MJ Archer, A Boca, CM Fetzer, S Mesropian, T Isshiki, M Haddad, KM Edmondson, et al. Future technology pathways of terrestrial iii–v multijunction solar cells for concentrator photovoltaic systems. *Solar Energy Materials and Solar Cells*, 94(8):1314–1318, 2010.

- [55] Lukas Kranz, Antonio Abate, Thomas Feurer, Fan Fu, Enrico Avancini, Johannes Lockinger, Patrick Reinhard, Shaik M Zakeeruddin, Michael Gratzel, Stephan Buecheler, et al. High-efficiency polycrystalline thin film tandem solar cells. *The journal of physical chemistry letters*, 6(14):2676–2681, 2015.
- [56] WGJHM Van Sark. Enhancement of solar cell performance by employing planar spectral converters. *Applied Physics Letters*, 87(15):151117, 2005.
- [57] T Trupke, MA Green, and P Würfel. Improving solar cell efficiencies by down-conversion of high-energy photons. *Journal of Applied Physics*, 92(3):1668–1674, 2002.
- [58] BS Richards. Enhancing the performance of silicon solar cells via the application of passive luminescence conversion layers. *Solar energy materials and solar cells*, 90(15):2329–2337, 2006.
- [59] WGJHM van Sark, A Meijerink, and REI Schropp. *Solar spectrum conversion for photovoltaics using nanoparticles*. INTECH Open Access Publisher, 2012.
- [60] D Timmerman, I Izeddin, P Stallinga, IN Yassievich, and T Gregorkiewicz. Space-separated quantum cutting with silicon nanocrystals for photovoltaic applications. *Nature Photonics*, 2(2):105–109, 2008.
- [61] Rene T Wegh, Harry Donker, Koenraad D Oskam, and Andries Meijerink. Visible quantum cutting in ligdf4: Eu3+ through downconversion. *Science*, 283(5402):663–666, 1999.
- [62] M Oliver and T Jackson. Energy and economic evaluation of building-integrated photovoltaics. *Energy*, 26(4):431–439, 2001.
- [63] JJ Bloem. Evaluation of a pv-integrated building application in a well-controlled outdoor test environment. *Building and Environment*, 43(2):205–216, 2008.
- [64] DailyMail. It’s like living in a tanning salon! family’s agony over neighbour’s solar panels that reflects sunlight directly into their home. [Accessed Online on 19 October 2015 from; <http://www.dailymail.co.uk/news/article-2314691/Its-like-living-tanning-salon-Familys-agony-neighbours-solar-panels-reflects-sunlight-directly-home.html>].
- [65] Simon Roberts and Nicolo Guariento. *Building integrated photovoltaics: a handbook*. Walter de Gruyter, 2009.
- [66] Gopal Nath Tiwari and Swapnil Dubey. *Fundamentals of photovoltaic modules and their applications*. Number 2. Royal Society of Chemistry, 2010.
- [67] Utpal Gangopadhyay, Sukhendu Jana, Sayan Das, Sutapa Garain, and Soma Ray. Antireflective nanocomposite based coating on crystalline silicon solar cells for building-integrated photovoltaic systems. In *Conference Papers in Science*, volume 2013. Hindawi Publishing Corporation, 2013.
- [68] Motech Industries. Monocrystalline x-cells, 2013. [Accessed Online on 27 August 2013 from; <http://www.motechsolar.com/en/doc/cell/XS156B3-200R.pdf>].

- [69] Shin Woei Leow. *Low-cost photovoltaics: Luminescent solar concentrators and colloidal quantum dot solar cells*. PhD thesis, Department of Electrical Engineering, University of California, Santa Cruz, 2014.
- [70] Peter M Martin. *Handbook of deposition technologies for films and coatings: science, applications and technology*. William Andrew, 2009.
- [71] PerkinElmer. Lambda 650/850/950 hardware guide, 2004.
- [72] Experimental Techniques Centre. Practical scanning electron microscopy. [professional development course handout]. etc, brunel university london, uk, 2013.
- [73] Thermo Electron Corporation. Lindberg blue laboratory furnaces, USA, 2015. [Accessed Online on 22 August 2015 from; [http : //www.thermo.com.cn/Resources/200802/productPDF_31131.pdf](http://www.thermo.com.cn/Resources/200802/productPDF_31131.pdf)].
- [74] Günther Höhne, Wolfgang Hemminger, and H-J Flammersheim. *Differential scanning calorimetry*. Springer Science & Business Media, 2003.
- [75] Z Xia, D Cunningham, and J Wohlgemuth. A new method for measuring cross-link density in ethylene vinyl acetate-based encapsulant. *Photovoltaics International*, 5:150–159, 2009.
- [76] D Dimova-Malinovska. The state-of-the-art and future development of the photovoltaic technologies—the route from crystalline to nanostructured and new emerging materials. In *Journal of Physics: Conference Series*, volume 253, page 012007. IOP Publishing, 2010.
- [77] Deepak Verma, Tor O Saetre, and Ole-Morten Midtgård. Review on up/down conversion materials for solar cell application. In *Photovoltaic Specialists Conference (PVSC), 2012 38th IEEE*, pages 002608–002613. IEEE, 2012.
- [78] Jinkuk Kim, Jejun Park, Ji Hwa Hong, Sung Jin Choi, Gi Hwan Kang, Gwon Jong Yu, Nam Soo Kim, and Hee-eun Song. Double antireflection coating layer with silicon nitride and silicon oxide for crystalline silicon solar cell. *Journal of Electroceramics*, 30(1-2):41–45, 2013.
- [79] Youngseok Lee, Daeyeong Gong, Nagarajan Balaji, Youn-Jung Lee, and Junsin Yi. Stability of SiNx/SiNx double stack antireflection coating for single crystalline silicon solar cells. *Nanoscale research letters*, 7(1):1–6, 2012.
- [80] Guillermo Santana and Arturo Morales-Acevedo. Optimization of pecvd SiNx : H films for silicon solar cells. *Solar energy materials and solar cells*, 60(2):135–142, 2000.
- [81] Ihsanul Afdi Yunaz, Kenji Hashizume, Shinsuke Miyajima, Akira Yamada, and Makoto Konagai. Fabrication of amorphous silicon carbide films using vhf-pecvd for triple-junction thin-film solar cell applications. *Solar Energy Materials and Solar Cells*, 93(6):1056–1061, 2009.
- [82] Quiozola Cojocar, Soum-Glaude Larrieu, and L. Thomas Massines. Use of liquid precursor tms for deposition of antireflective and passivating a-sic(n):h

- thin films with low pressure/low frequency pecvd. *24th European Photovoltaic Solar Energy Conference Proceedings*, pages 1617 – 1622, 2009.
- [83] J De la Torre, G Bremond, M Lemiti, G Guillot, P Mur, and N Buffet. Using silicon nanostructures for the improvement of silicon solar cells' efficiency. *Thin Solid Films*, 511:163–166, 2006.
- [84] Ko-Shao Chen, Shu-Chuan Liao, Shao-Hsuan Tsao, Norihiro Inagaki, Hsin-Ming Wu, Chin-Yen Chou, and Wei-Yu Chen. Deposition of tetramethylsilane on the glass by plasma-enhanced chemical vapor deposition and atmospheric pressure plasma treatment. *Surface and Coatings Technology*, 228:S33–S36, 2013.
- [85] PubChem. Open chemistry database -tetramethylsilane, 2014. [Accessed Online on 22 December 2014 from; <http://pubchem.ncbi.nlm.nih.gov/compound/tetramethylsilane#section=Top>].
- [86] FluoroChem ltd. Tetramethylsilane, MSDS No.S16225, FluroChem ltd, Derbyshire, UK, 2015. [Accessed Online on 22 August 2015 from; <http://www.fluorochem.co.uk/Products/Product?code=S16225>].
- [87] Day-Shan Liu and Cheng-Yang Wu. Adhesion enhancement of hard coatings deposited on flexible plastic substrates using an interfacial buffer layer. *Journal of Physics D: Applied Physics*, 43(17):175301, 2010.
- [88] Boris V Lvov and VL Ugolkov. The self-heating effect in the process of kmno4 decomposition in vacuum. *Journal of thermal analysis and calorimetry*, 94(2):453–460, 2008.
- [89] N Nelson, RT Rakowski, J Franks, P Woolliams, P Weaver, and BJ Jones. The effect of substrate geometry and surface orientation on the film structure of dlc deposited using pecvd. *Surface and Coatings Technology*, 254:73–78, 2014.
- [90] M Stupca, M Alsalhi, T Al Saud, A Almuhanha, and MH Nayfeh. Enhancement of polycrystalline silicon solar cells using ultrathin films of silicon nanoparticle. *Applied Physics Letters*, 91(6):063107, 2007.
- [91] V Švrček, A Slaoui, and J-C Muller. Silicon nanocrystals as light converter for solar cells. *Thin Solid Films*, 451:384–388, 2004.
- [92] Jaime Aguilar, Yasuhiro Matsumoto, Gabriel Romero, and M Alfredo Reyes. Optical mismatch in double ar coated c-si, a simple theoretical and experimental correlation. In *Photovoltaic Energy Conversion, 2003. Proceedings of 3rd World Conference on*, volume 2, pages 1001–1004. IEEE, 2003.
- [93] Minghua Li, Hui Shen, Lin Zhuang, Daming Chen, and Xinghua Liang. SiO₂ antireflection coatings fabricated by electron-beam evaporation for black monocrystalline silicon solar cells. *International Journal of Photoenergy*, 2014, 2014.
- [94] B.S. Richards, Jeffrey E. Cotter, C.B. Honsberg, and S.R. Wenham. Novel uses of tio₂ in crystalline silicon solar cells. In *Photovoltaic Specialists Conference, 2000. Conference Record of the Twenty-Eighth IEEE*, pages 375–378, 2000.

- [95] BS Richards, JE Cotter, and CB Honsberg. Enhancing the surface passivation of tio₂ coated silicon wafers. *Applied Physics Letters*, 80(7):1123–1125, 2002.
- [96] BS Richards, SF Rowlands, A Ueranatasun, JE Cotter, and CB Honsberg. Potential cost reduction of buried-contact solar cells through the use of titanium dioxide thin films. *Solar Energy*, 76(1):269–276, 2004.
- [97] Jia Li, Yuehui Lu, Pinjun Lan, Xianpeng Zhang, Wei Xu, Ruiqin Tan, Weijie Song, and Kwang-Leong Choy. Design, preparation, and durability of tio₂/sio₂ and zro₂/sio₂ double-layer antireflective coatings in crystalline silicon solar modules. *Solar Energy*, 89:134–142, 2013.
- [98] Zhaoyong Wang, Ning Yao, and Xing Hu. Single material tio₂ double layers antireflection coating with photocatalytic property prepared by magnetron sputtering technique. *Vacuum*, 108:20–26, 2014.
- [99] PHV Sesha Talpa Sai, JV Ramana Rao, KC Devarayapalli, and KV Sharma. Preparation and characterization of tio₂-sio₂ sol-gel anti reflection coatings on multi crystalline silicon solar cell. *International Journal of Engineering and Advanced Technology*, 2013.
- [100] Ram Kishore, Ravi Kumar, NK Arora, and SN Singh. Screen printed titanium dioxide antireflection coating on silicon solar cells. In *Semiconductor devices*, volume 2733, page 448, 1996.
- [101] Ing-Song Yu, Yu-Wun Wang, Hsyi-En Cheng, Zu-Po Yang, and Chun-Tin Lin. Surface passivation and antireflection behavior of ald on n-type silicon for solar cells. *International Journal of Photoenergy*, 2013, 2013.
- [102] Barbara Swatowska, Tomasz Stapinski, Kazimierz Drabczyk, and Piotr Panek. The role of antireflective coatings in silicon solar cells—the influence on their electrical parameters. *Optica Applicata*, 41(2):487–492, 2011.
- [103] BS Richards. Single-material tio₂ double-layer antireflection coatings. *Solar Energy Materials and Solar Cells*, 79(3):369–390, 2003.
- [104] Seung Jae Oh, Sameer Chhajed, David J Poxson, Jaehee Cho, E Fred Schubert, Sung Ju Tark, Donghwan Kim, and Jong Kyu Kim. Enhanced broadband and omni-directional performance of polycrystalline si solar cells by using discrete multilayer antireflection coatings. *Optics express*, 21(101):A157–A166, 2013.
- [105] LA Dobrzański and M Szindler. Sol gel tio₂ antireflection coatings for silicon solar cells. *Journal of Achievements in Materials and Manufacturing Engineering*, 52(1), 2012.
- [106] D Hocine, MS Belkaid, M Pasquinelli, L Escoubas, JJ Simon, GA Rivière, and A Moussi. Improved efficiency of multicrystalline silicon solar cells by tio₂ antireflection coatings derived by apcvd process. *Materials Science in Semiconductor Processing*, 16(1):113–117, 2013.
- [107] MJ Ariza, F Martin, and D Leinen. Xps in-depth composition study on commer-

- cial monocrystalline silicon solar cells. *Surface and interface analysis*, 35(3):251–255, 2003.
- [108] MJ Ariza, F Martín, and D Leinen. Xps surface analysis of monocrystalline silicon solar cells for manufacturing control. *Applied Physics A*, 73(5):579–584, 2001.
- [109] EV Buta, P Pascariu, F Prihor, L Vlad, V Pohoată, R Apetrei, D Luca, A Nastuță, I Alupoaei, and D Mardare. characterization of sputtered tio2 thin films. *Biomaterials in Biophysics Medical Physics and Ecology*, page 5, 2008.
- [110] Sonya Calnan. Applications of oxide coatings in photovoltaic devices. *Coatings*, 4(1):162–202, 2014.
- [111] Deepti A Rukade and Varsha Bhattacharyya. Single-phase tio2 formation by plasma oxidation of titanium thin films. *Surface and Interface Analysis*, 2015.
- [112] Khuram Ali, Sohail A Khan, and MZ Mat Jafri. Enhancement of silicon solar cell efficiency by using back surface field in comparison of different antireflective coatings. *Solar Energy*, 101:1–7, 2014.
- [113] Shui-Yang Lien, Dong-Sing Wu, Wen-Chang Yeh, and Jun-Chin Liu. Tri-layer antireflection coatings (sio₂/sio₂-tio₂/tio₂) for silicon solar cells using a sol-gel technique. *Solar Energy Materials and Solar Cells*, 90(16):2710–2719, 2006.
- [114] Ching-Hua Wei and Ching-Min Chang. Polycrystalline tio2 thin films with different thicknesses deposited on unheated substrates using rf magnetron sputtering. *Materials transactions*, 52(3):554–559, 2011.
- [115] Sakae Tanemura, Lei Miao, Wilfried Wunderlich, Masaki Tanemura, Yukimasa Mori, Shoichi Toh, and Kenji Kaneko. Fabrication and characterization of anatase/rutile-tio₂ thin films by magnetron sputtering: A review. *Science and Technology of Advanced Materials*, 6(1):11–17, 2005.
- [116] MM Abd El-Raheem and Ateyyah M Al-Baradi. Optical properties of as-deposited tio2 thin films prepared by dc sputtering technique. *International Journal of Physical Sciences*, 8(31):1570–1580, 2013.
- [117] Khuram Ali, Sohail A Khan, and MZ Mat Jafri. Effect of double layer (sio₂/tio₂) anti-reflective coating on silicon solar cells. *Int. J. Electrochem. Sci*, 9:7865–7874, 2014.
- [118] Leslie Holland. Vacuum deposition of thin films. *London: Chapman & Hall, 1970*, 1, 1970.
- [119] Sreenivasan Koliyat Parayil, Rhett J Psota, and Ranjit T Koodali. Modulating the textural properties and photocatalytic hydrogen production activity of tio₂ by high temperature supercritical drying. *International Journal of Hydrogen Energy*, 38(25):10215–10225, 2013.

- [120] M Saif, SMK Aboul-Fotouh, SA El-Molla, MM Ibrahim, and LFM Ismail. Improvement of the structural, morphology, and optical properties of tio₂ for solar treatment of industrial wastewater. *Journal of Nanoparticle Research*, 14(11):1–11, 2012.
- [121] Nevill Francis Mott and Edward A Davis. *Electronic processes in non-crystalline materials*. Oxford University Press, 2012.
- [122] PK Manoj, P Koshy, and VK Vaidyan. Transparent anatase titania films: A critical study on optical properties. *Progress in Natural Science: Materials International*, 22(2):79–85, 2012.
- [123] K Madhusudan Reddy, Sunkara V Manorama, and A Ramachandra Reddy. Bandgap studies on anatase titanium dioxide nanoparticles. *Materials Chemistry and Physics*, 78(1):239–245, 2003.
- [124] MD Hamilton, A Butt, S Patel, C Sukotjo, D Royhman, and CG Takoudis. Anatase phase, hydrophilicity, and thickness of thermally oxidized tio₂ layer on titanium-v alloy. *Journal of Undergraduate Research*, 6:16–19, 2013.
- [125] D Velten, V Biehl, F Aubertin, B Valeske, W Possart, and J Breme. Preparation of tio₂ layers on cp-ti and ti6al4v by thermal and anodic oxidation and by sol-gel coating techniques and their characterization. *Journal of biomedical materials research*, 59(1):18–28, 2002.
- [126] Bryce Sydney Richards. Novel uses of titanium dioxide for silicon solar cells. 2002.
- [127] GA Battiston, R Gerbasi, A Gregori, M Porchia, S Cattarin, and GA Rizzi. Pecvd of amorphous tio₂ thin films: effect of growth temperature and plasma gas composition. *Thin Solid Films*, 371(1):126–131, 2000.
- [128] Samuel Chen, MG Mason, HJ Gysling, GR Paz-Pujalt, TN Blanton, T Castro, KM Chen, CP Fictorie, WL Gladfelter, A Franciosi, et al. Ultrahigh vacuum metalorganic chemical vapor deposition growth and insitu characterization of epitaxial tio₂ films. *Journal of Vacuum Science & Technology A*, 11(5):2419–2429, 1993.
- [129] Efthymios Klampaftis, Martina Congiu, Neil Robertson, and Bryce S Richards. Luminescent ethylene vinyl acetate encapsulation layers for enhancing the short wavelength spectral response and efficiency of silicon photovoltaic modules. *Photovoltaics, IEEE Journal of*, 1(1):29–36, 2011.
- [130] Keith R McIntosh, Gay Lau, James N Cotsell, Katherine Hanton, Derk L Bätzner, Fabian Bettiol, and Bryce S Richards. Increase in external quantum efficiency of encapsulated silicon solar cells from a luminescent down-shifting layer. *Progress in Photovoltaics: Research and Applications*, 17(3):191–197, 2009.
- [131] Patrick Campbell and Martin A Green. Light trapping properties of pyramidally textured surfaces. *Journal of Applied Physics*, 62(1):243–249, 1987.

- [132] Juanita Kurtin. Improved solar cell efficiency through the use of an additive nanostructure-based optical downshifter. *Contract*, 303:275–3000, 2011.
- [133] R Abrams Zeev, Avi Niv, and Xiang Zhang. Solar energy enhancement using down-converting particles: A rigorous approach. *Journal of Applied Physics*, 109(11):114905, 2011.
- [134] Philip Chung, Hsiu-hsin Chung, and Paul H Holloway. Phosphor coatings to enhance si photovoltaic cell performance. *Journal of Vacuum Science & Technology A*, 25(1):61–66, 2007.
- [135] S Marchionna, F Meinardi, M Acciarri, S Binetti, A Papagni, S Pizzini, V Malatesta, and R Tubino. Photovoltaic quantum efficiency enhancement by light harvesting of organo-lanthanide complexes. *Journal of luminescence*, 118(2):325–329, 2006.
- [136] Tongxin Wang, Bo Yu, Zhijia Hu, Xin Wang, Gang Zou, and Qijin Zhang. Enhancing the performance of multi-crystalline silicon photovoltaic module by encapsulating high efficient eu 3+ complex into its pre-existing eva layer. *Optical Materials*, 35(5):1118–1123, 2013.
- [137] Chen Yen-Chi, Huang Woan-Yu, and Chen Teng-Ming. Enhancing the performance of photovoltaic cells by using down-converting keagd (po 4) 2: Eu 3+ phosphors. *Journal of Rare Earths*, 29(9):907–910, 2011.
- [138] Yen-Chi Chen and Teng-Ming Chen. Improvement of conversion efficiency of silicon solar cells using up-conversion molybdate la 2 mo 2 o 9: Yb, r (r= er, ho) phosphors. *Journal of Rare Earths*, 29(8):723–726, 2011.
- [139] Jian Liu, Kai Wang, Wei Zheng, Wei Huang, Cheng-Hui Li, and Xiao-Zeng You. Improving spectral response of monocrystalline silicon photovoltaic modules using high efficient luminescent down-shifting eu3+ complexes. *Progress in Photovoltaics: Research and Applications*, 21(4):668–675, 2013.
- [140] J-Y Chen, CK Huang, WB Hung, KW Sun, and TM Chen. Efficiency improvement of si solar cells using metal-enhanced nanophosphor fluorescence. *Solar Energy Materials and Solar Cells*, 120:168–174, 2014.
- [141] Liqin Liu, En Ma, Renfu Li, and Xueyuan Chen. Preparation, characterization and spectroscopy of eu3+ in gd2o3 nanorods. *Journal of nanoscience and nanotechnology*, 8(3):1398–1403, 2008.
- [142] Xiao Yan. *Phosphors for Lighting Applications*. PhD thesis, Wolfson Centre for Materials Processing, Brunel University, 2012.
- [143] L Hernández-Adame, F Medellín-Rodríguez, A Méndez-Blas, R Vega-Acosta, and G Palestino. Synthesis of gd2o2s: Tb nanoparticles and optical characterization. In *SPIE OPTO*, pages 86261P–86261P. International Society for Optics and Photonics, 2013.
- [144] Swapnil Dubey, Jatin Narotam Sarvaiya, and Bharath Seshadri. Temperature

dependent photovoltaic (pv) efficiency and its effect on pv production in the world—a review. *Energy Procedia*, 33:311–321, 2013.

- [145] Ali Serpenguzel, Temel Bilici, Ibrahim Inanç, Adnan Kurt, Jim Carey, and Eric Mazur. Temperature dependence of photoluminescence in noncrystalline silicon. In *Integrated Optoelectronic Devices 2004*, pages 454–462. International Society for Optics and Photonics, 2004.
- [146] EI Gorokhova, VA Demidenko, OA Khristich, SB Mikhlin, and PA Rodnyi. Luminescence properties of ceramics based on terbium-doped gadolinium oxy-sulfide. *Journal of Optical Technology*, 70(10):693–698, 2003.
- [147] Peter Klemchuk, Myer Ezrin, Gary Lavigne, William Holley, James Galica, and Susan Agro. Investigation of the degradation and stabilization of eva-based encapsulant in field-aged solar energy modules. *Polymer Degradation and Stability*, 55(3):347–365, 1997.
- [148] FJ Pern. Luminescence and absorption characterization of ethylene-vinyl acetate encapsulant for pv modules before and after weathering degradation. *Polymer degradation and stability*, 41(2):125–139, 1993.
- [149] YM Chen, P Lin, Y He, JQ He, J Zhang, and XL Li. Fast quantifying collision strength index of ethylene-vinyl acetate copolymer coverings on the fields based on near infrared hyperspectral imaging techniques. *Scientific reports*, 6, 2016.
- [150] PerkinElmer. Curing determination of eva for solar panel application by dsc, 2010.
- [151] Javier Camacho, Eduardo Díez, Gabriel Ovejero, and Ismael Díaz. Thermodynamic interactions of eva copolymer-solvent systems by inverse gas chromatography measurements. *Journal of Applied Polymer Science*, 128(1):481–486, 2013.
- [152] Takuya Doi, Izumi Tsuda, Hiroaki Unagida, Akinobu Murata, Koichi Sakuta, and Kosuke Kurokawa. Experimental study on pv module recycling with organic solvent method. *Solar energy materials and solar cells*, 67(1):397–403, 2001.
- [153] Joseph J Jasper. The surface tension of pure liquid compounds. *Journal of physical and chemical reference data*, 1(4):841–1010, 1972.
- [154] Fisher Scientific. P-xylene, MSDS No. 106-42-3, Fisher Scientific, Loughborough, UK, 2015. [Accessed Online on 22 August 2015 from; <https://www.fishersci.com/shop/products/p-xylene-certified-fisher-chemical-2/p-216456>].
- [155] Fisher Scientific. Chlorobenzene, MSDS No.108-90-7 , Fisher Scientific, Loughborough, UK, 2015. [Accessed Online on 22 August 2015 from; <https://www.fishersci.com/shop/products/chlorobenzene-certified-fisher-chemical-2/p-215811>].
- [156] Fisher Scientific. Toluene, MSDS No. 108-88-3, Fisher Scientific, Loughborough, UK, 2015. [Accessed Online on 22 August 2015 from;

<https://www.fishersci.com/shop/products/toluene-acs-ar-macron-fine-chemicals-4/14650374>].

- [157] Wen-Jeng Ho, Guo-Chang Yang, Yu-Tang Shen, and Yu-Jie Deng. Improving efficiency of silicon solar cells using europium-doped silicate-phosphor layer by spin-on film coating. *Applied Surface Science*, 365:120–124, 2016.
- [158] Musa T Zarmai, NN Ekere, CF Oduoza, and Emeka H Amalu. A review of interconnection technologies for improved crystalline silicon solar cell photovoltaic module assembly. *Applied Energy*, 154:173–182, 2015.
- [159] Torpedo Speciality Wire Inc. Solar module ribbon wire specifications, Rocky Mount, NC 27804, USA, 2015. [Accessed Online on 12 January 2015 from; <http://www.torpedowire.com/solar-module-ribbon-wire-cell-interconnect-wire.html>].
- [160] Daniel D Pollock. *Thermocouples: theory and properties*. CRC press, 1991.
- [161] ASTM Committee E20 on Temperature Measurement. *Manual on the use of thermocouples in temperature measurement*, volume 28. ASTM International, 1993.
- [162] OMEGA Engineering, User’s Guide: CI-300, CI-301, CI-302, CI-303 Portable Simulator, OMEGA Engineering, INC, 2015. [Accessed Online on 11 December 2015 from; <https://www.omega.com/manuals/>].
- [163] PerkinElmer. Guide to selection of dsc sample pans, 2013. Technical notes-Thermal Analysis.

Appendices

Nanostructured Silicon Oxide Film for Enhanced Crystalline Solar Cell

Abdulla Tahhan^{*1}, Zahir Dehouche¹, Tony Anson², George Fern³

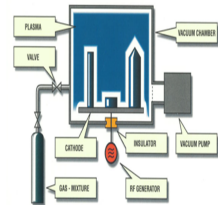
¹ School of Engineering and Design, Brunel University, Uxbridge, UB8 3PH, UK
² Experimental Techniques Centre, Brunel University, Uxbridge, UB8 3PH, UK
³ Wolfson Centre for Materials Processing, Brunel University, Uxbridge, UB8 3PH, UK
^{*} Corresponding author: Abdulla.Tahhan@brunel.ac.uk

Introduction:

The solar cells industry has been growing with astonishing rates over the past years and this is driven by the need of cost reduction and efficiency improvement. However, the conversion efficiency of the conventional silicon solar cell is based on its bandgap. This problem can be addressed by silicon based nanostructured materials which are one of the most promising candidates for enhancing the efficiency of the solar cells [1].

Methodology:

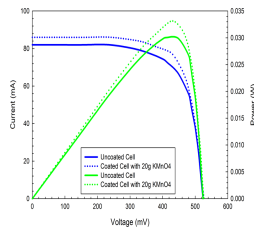
Silicon oxide thin-films were deposited on top of commercial monocrystalline photovoltaic solar cell by Plasma Enhanced Chemical Vapour Deposition (PECVD) using TetraMethylSilane (TMS) precursor as silicon source and oxidized with different percentages with potassium permanganate with the formula $KMnO_4$ as an oxidant agent. This study compares the electrical and optical characteristics of silicon cells before and after coating. The surface structure and chemical composition was observed by Scanning Electron Microscopy (SEM).



Schematic of PECVD System [2]

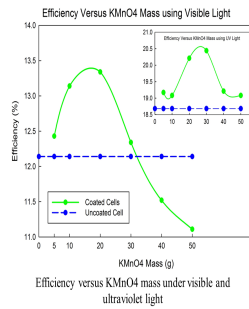
Electrical Characteristics:

The electrical performance of the solar cells with and without silicon oxide nanoparticles treatment is characterized by current versus voltage (I-V) and power versus voltage (P-V) curves using visible and ultraviolet light source.



I-V & P-V curves of the coated and uncoated cell under visible light source

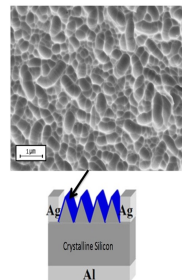
The electrical conversion efficiency of the coated cells is affected by the concentration of the oxygen in the deposited layer which is controlled by the mass of $KMnO_4$ introduced during the PECVD process.



Efficiency versus $KMnO_4$ mass under visible and ultraviolet light

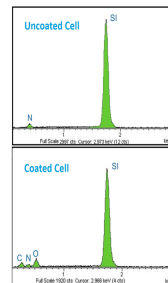
Structural Analysis:

SEM image of silicon oxide nanoparticles deposited on top of monocrystalline solar cell surface indicates that the nanoparticles self-assembled into closely packed structure.



SEM image on the top surface of the coated solar cell

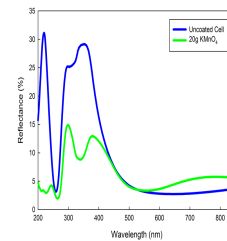
SEM composition analysis for the coated cell with maximum enhancement shows the presence of carbon, nitride, oxygen and silicon elements in the deposited layer.



Chemical composition of the top surface of the uncoated and coated cell with maximum enhancement

Optical Properties:

Reflectance analysis of the coated cell with maximum electrical output enhancement shows less reflectance in comparison with uncoated one in the range of ultraviolet, visible and near infra red light region which is resulted in absorbing more photons that generate more charges carrier which increase the electrical conversion efficiency.



Reflectance spectrum of the uncoated and coated solar cell with maximum electrical output enhancement

Conclusion:

The experimental results show a relative enhancement of 10% (from 12.13% to 13.34%) in the monocrystalline cell electrical conversion efficiency. However, this can be further enhanced by optimizing the coating process.

References:

[1] Sugeca M., Alshali M., Al Saad T., Almalhama A. and Nayfeh, M.H. (2007) "Enhancement of polycrystalline silicon solar cells using silicon thin films of silicon nanoparticles", Applied Physics Letters, vol. 91, no. 6.
 [2] Duras: ACM Ltd. Diamond-Like Carbon Coating Centre, Brunel University.

School of Engineering and Design

This poster was presented in the 40th IEEE Photovoltaic Specialist Conference (PVSC), 2014. The poster titled "Nanostructured silicon oxide film for enhanced crystalline solar cell". Authors of the work were Mr Abdulla Tahhan, Dr Zahir Dehouche, Prof Tony Anson, and Dr George Fern

TiO₂ Nanoparticles for Enhanced Monocrystalline Solar Cell

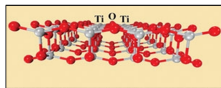
Chiara Breda¹, Zahir Dehouche¹, Abdulla Tahhan¹, Tony Anson², George Fern³
¹School of Engineering and Design, Brunel University, Uxbridge, UB8 3PH, UK
²Experimental Techniques Centre, Brunel University, Uxbridge, UB8 3PH, UK
³Wolfson Centre for Materials Processing, Brunel University, Uxbridge, UB8 3PH, UK

1. Introduction

The continuing demand for energy, in the near future, has led many researchers to investigate alternative sources of clean energy. Nanoparticles have been recently investigated as a possible way to improve absorption of the light in solar cells. The strong interaction of nanoparticles with light allows control over the propagation of light at the nanoscale and thus the design of solar cells, in which the light is trapped in an active layer and efficiently absorbed. In this way the **efficiency increase** and the cost of the solar cell decrease.

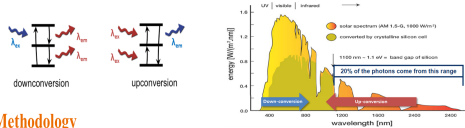


Recently, the use of dielectric nanoparticles has been demonstrated theoretically to lead to similar and even higher enhancement compared to that of metallic nanoparticles [1]. TiO₂ is a dielectric material. Other properties include band gap in the range of: 3.0-3.2 eV, high-refractive index and an excellent transparency to visible, near and infrared light.



Objectives

- In the current monocrystalline solar cells, photons with energies higher than the band gap are not absorbed but also are converted in thermal losses through the device. Consequently, these cells lack long wavelength response and efficiency.
- Investigates how TiO₂ particles layer affect the performance of monocrystalline solar cells.
- Compare two different oxidation methods. In this way, a Titanium (Ti) layer was deposited on monocrystalline solar cells and subsequently oxidised. One sample of coated PV cell was heated in a furnace in contact with atmospheric air and the other by Plasma Enhanced Chemical Vapour Deposition (PECVD) using a highly oxidising material: potassium permanganate KMnO₄.
- Analyse the electrical characteristics, optical and morphological properties of the solar cells.



2. Methodology

The Titanium was deposited over a monocrystalline solar cell by thermal evaporator. The evaporated titanium is condensed on the PV cell substrates and the thickness of 7.9 nm was measured. After this, one cell was oxidised by a furnace (LINDBERG BLUE M Thermo scientific) at 400°C for 1 hour and the other cell was oxidised by the thermal decomposition of the potassium permanganate in the PECVD machine. Argon is used as plasma sources and 30g Potassium Permanganate (by Fisher Scientific UK) was used to oxidise the sample. The chemical reaction inside the chamber was:



Total pressure and total gas flow rate are fixed at 3x10⁻⁴ Torr and 25 sccm, respectively for the period of 60 minutes, the cathode voltage 100V and the power 15W.



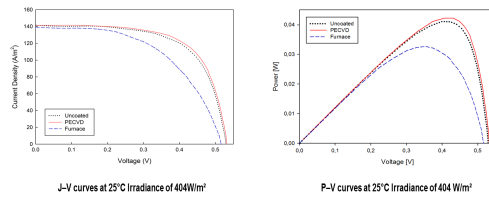
PECVD machine



Thermal evaporator

3. Electrical Properties

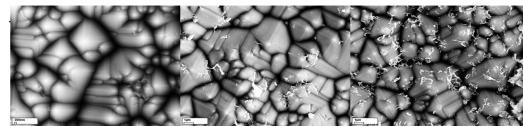
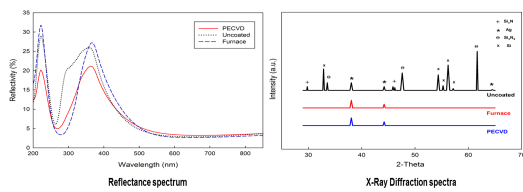
The electrical characteristics of the solar cells were tested at 25°C at G=404 W/m² irradiances with visible light and a cell area of 9 cm² was used. The characteristic J-V and P-V curves of these monocrystalline solar cells are presented and the corresponding photovoltaic parameters are tabulated below.



	J _{sc}	V _{oc}	P _{max}	J _{mp}	V _{mp}	Efficiency	Fill Factor
	A/m ²	V	mW	A/m ²	V	-	-
Uncoated	141.54	0.529	41.1	120.49	0.399	11.90 %	0.64205
Furnace	139.20	0.516	32.6	107.61	0.355	9.46 %	0.53189
PECVD	141.54	0.532	42.2	121.67	0.406	12.23 %	0.65615

4. Optical properties

The reflectivity measurements were taken using the UVVisible spectrometer (Perkin-Elmer Precisely Lambda 650S UVVis) with wavelengths range between 200 and 850 nm. The crystallization behaviour of TiO₂ films deposited on silicon substrates was studied by grazing angle X-ray diffraction, using the Bruker AXS D8 Advance X-Ray Diffract meter in 2θ range between 0.75 and 3 degrees with a copper non-monochromatic source.



5. Conclusion

Efficiency enhancements have been observed in monocrystalline silicon solar cells with deposition of TiO₂ using PECVD. An increase in power conversion efficiency from 11.9% to 12.23% in visible light has been observed. This demonstrates that TiO₂ films created with different oxidising process contribute to efficiency enhancement of solar cells without adding much to the manufacturing cost. It has been observed that the deposition of TiO₂ film on monocrystalline silicon solar cell prepared in PECVD process reduces the reflectance. This can be due to a better matching between the refractive index in both the film and the substrate. Furthermore, the use of PECVD during the oxidising process improves the antireflective properties. The cell oxidised in PECVD process, show a different structure on a microscopic scale: the layer is more uniform than the others and the decrease of the grain size can be clearly observed. Such morphology is advantageous for efficient cells, because a fast and uninterrupted ionic charge transport can prevent recombination losses.

References

- [1] Yu, A. Akimov, W.S. Koh, S.Y. Sian, and S. Ren. Nanoparticle-enhanced thin film solar cells: Metallic or Dielectric nanoparticles? s.l.: Applied Physics letters 96,073111, 18 February 2010.

School of Engineering and Design



This poster was presented in the 40th IEEE Photovoltaic Specialist Conference (PVSC), 2014. The poster titled “Titanium dioxide for enhanced monocrystalline solar cell”. Authors of the work were Mrs Chiara Breda, Dr Zahir Dehouche, Mr Abdulla Tahhan, Prof Tony Anson, and Dr George Fern

Abdulla Tahhan*, Dr. Zahir Dehouche, Dr George Fern, Prof. Tony Anson
*Email: Abdulla.Tahhan@Brunel.ac.uk

Introduction

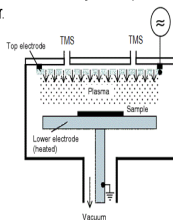
The solar cell industry has been growing with astonishing rates over the past years and this is driven by the need of cost reduction and efficiency improvement. However, the conversion efficiency of the conventional silicon solar cell is based on its bandgap. This problem can be addressed by silicon based nanostructured materials which are one of the most promising candidates for enhancing the efficiency of the solar cells [1].

Methodology

In this work, an investigation into the effects of nanostructured materials on photovoltaic solar cell is carried out. Silicon nanoparticles produced by Plasma Enhanced Chemical Vapour Deposition (PECVD) are applied on the top of conventional polycrystalline silicon solar cell. The electrical and optical characteristics of the coated solar cell are monitored and compared to non-coated solar cell for each different coating condition in order to observe any enhancement in performance. The electrical characteristics of the cell are observed under the visible and ultraviolet light source. Furthermore, structure properties of the deposited layer has been analysed using Scanning Electron Microscope (SEM) and Raman microscope in order to evaluate the size of the nanoparticles and also to examine the composition of the deposited particle are also presented. The experimental investigations on the structural, electrical and optical properties of the coated layer can lead to a better design of the device. Thus, more promising results could be expected.

Material Fabrication

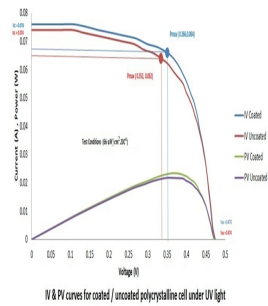
The silicon nanoparticles grown on polycrystalline solar cells by PECVD method using tetramethylsilane as a precursor.



[2] Schematic of PECVD chamber

Electrical Characteristics

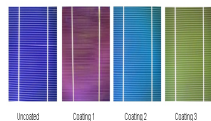
The coating conditions have been refined through the experimental work in order to find the optimum coating conditions that give the best electrical output enhancement of the PV cell.



The table below shows the best results of the electrical characteristics of the cells under the UV and visible light source. It can be seen with the naked eye that each coating has a different colour due to the different size of the silicon nanoparticles.

	Cell	Ir [mA]	Voc [V]	Power [mW]	FF	EFF [%]
UV Light	Uncoated	05.13	470.13	1672	0.413	4.09
	Coating 1	08.2	480.72	3916	0.455	5.73
	Coating 2	05.6	480.25	2727	0.42	5.85
	Coating 3	07.70	475.09	3533	0.443	5.41
Visible Light	Uncoated	68.15	442.83	3026	0.397	13.29
	Coating 1	05.91	489.18	2948	0.464	28.62
	Coating 2	09.7	457.24	4579	0.433	18.59
	Coating 3	01.54	481.76	7472	0.453	18.25

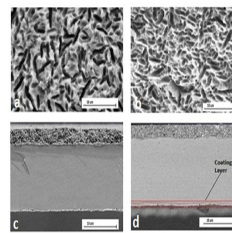
Table of the Electrical characteristics of different coatings conditions



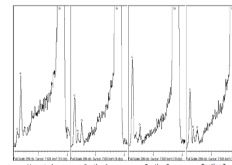
The effects of coatings on the color of the solar cell

Surface Analysis

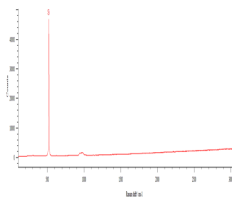
SEM images of silicon nanoparticles deposited on the surface of Polycrystalline solar cell before (a) and after (b) coating while (c) is cross section images of the same sample before and after (d) coating.



SEM composition analysis for uncoated and the other the coated cells clearly illustrates the variance of the compositions measured for each coating with a large increase in the amount of carbon in the coated cells compared to the uncoated cell. The varying level of carbon present is one of the main causes in the differing results.

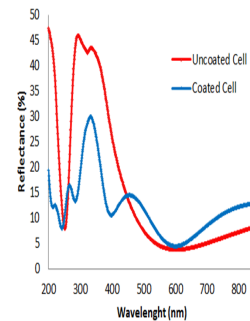


The spectra of Raman microscope analysis show the sharp band at 521cm⁻¹ which indicate the formation of crystalline silicon structure.



Optical Properties

Reflectance analysis of the coated cells in the Ultraviolet Visible and Near Infra Red (NIR) range shows that the nanoparticles improve the light absorption in particular in the UV light region and the short wavelength part of the visible light which resulted in absorbing more photons that generates charges carrier which increase the electrical output.



Conclusion

In summary, silicon nanoparticles in the range of 9-12 nm are integrated on PV silicon solar cells. The efficiency of polycrystalline cells is enhanced by 7% in the UV and by only 0.84% in the visible. The results also show that the efficiency enhancement is correlated with the presence of carbon in the fabricated silicon particles.

References

[1] Stupca, M., Alsilmi, M., Al Saad, T., Almuhamma, A. and Nagfeh, M.H. (2007) "Enhancement of polycrystalline silicon solar cells using ultrathin films of silicon nanoparticle", Applied Physics Letters, vol. 91, no. 6.
[2] Schmidt, J., Kern, M., Cuevas, A. Surface passivation of silicon solar cells using plasma-enhanced chemical-vapour-deposited SiN₂ films and thin thermal SiO₂ plasma SiN₂ stacks. Semiconductor Science and Technology 20(1):16-164

This poster was presented in the World Congress on Sustainable Technologies (WCST), 2012. The poster titled "Nanostructured materials for silicon solar cells grown by PECVD". Authors of the work were Mr Abdulla Tahhan, Dr Zahir Dehouche, Dr George Fern and Prof Tony Anson

Soldering Solar Cells

After preparing the required size of the solar cell, soldering solar cells can be completed using a 1.2 mm wide and 0.1 mm thick solder coated tabbing wire for solar cell consists of oxygen free soft copper clad with silver, tin and lead, supplied from (Torpedo Speciality Wire Inc., USA). The tabbing wire physical properties are shown in Table 1. Soldering solar cells was carried out using the following procedures:

- Before soldering solar cells, it is a good practice to do soldering on broken ones.
- The tabbing wire was cleaned and cut to 50 mm length.
- Rosin flux pen, no-clean soldering flux pen, was used to paint the flux on the tabbing wire.
- The soldering iron was heated to 350 °C. The temperature of the soldering iron is controlled by a soldering station (TENHAM model). It is important to keep the temperature for soldering, and the pressure applied as low as possible because differences in the thermal and mechanical properties of the used silicon solar cell and the tabbing wire cause a residual stress around the bonding area leading to cracks in the crystalline solar cell [158].
- Two tabbing wires were soldered to the solar cells, the tabbing wire was placed on the top of the front surface of the cell, and the soldering iron is dragged along it. Similarly, the second wire was soldered onto the back side of the cell.

Table 1: Physical properties of the Sn-Pb-Ag solder [159].

Composition	Copper	Tin	Lead	Silver
Standards (%)	0	36	2	62
Physical state	Solid			
Colour	Gray			
Melting point	179 °C (solder alloy)			
Yield strength	<90 N/mm ²			

Calibration of Thermocouples

The temperature unit used in the experiment consists of a thermocouple in contact with the back of the solar cell and data acquisition system connected to the computer. The thermocouple is a type of temperature sensor. It is made by joining two dissimilar metals at one end. The first joined end is referred to as the hot junction which is exposed to heat where the other end is the cold junction in which is formed at the last point of thermocouple material. Once a difference in temperature between the hot and cold junction occurs, a small voltage is created. This voltage is used to indicate temperature [160].

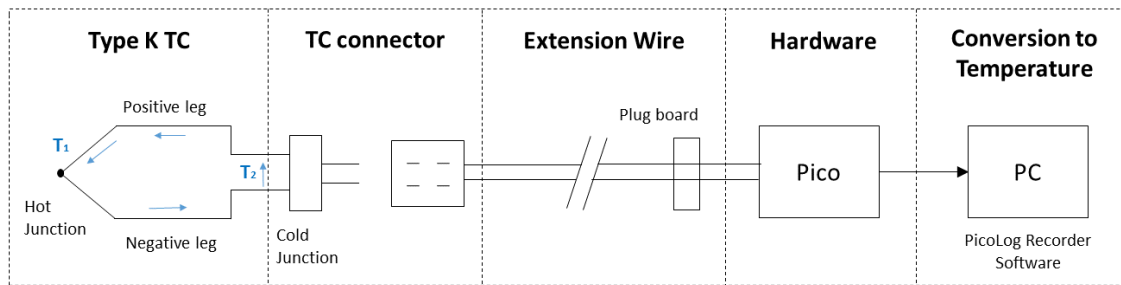


Figure 1: Schematic of the temperature data acquisition system.

The used thermocouples in the experiments were Type K thermocouple which is made from chromel (positive leg) and alumel (negative leg) alloys with a tip diameter of 1.5 and temperature range from -70 to 250 °C. Thermocouples and Data loggers were purchased from (Pico Technology, UK). The limits of error stated by the manufacturer, adhered to the American Society for Testing Materials (ASTM) specifications, is greatest of 0.75% of the reading in °C [161].

Figure 1 shows a schematic of the Temperature Data Acquisition System (TDAS). To establish the error for TDAS including the error for thermocouples, extension wire and data logging device used in the experiments. TDAS is connected to a portable OMEGA model CI-3512A thermocouple source as can be seen in Figure 2 which provides with equivalent temperature millivolt simulated signals in accordance with ASTM standards. The calibration device is a cold junction compensated for ambient temperature variations and provides a thermocouple connector output [162].

A 10 point calibration curve is created across the temperature range of $(10-50)$ °C. The calibration curve for the used thermocouple is shown in Figure 3. Each point on the calibration curve is a representation of the average results from 4 readings of the thermocouples. The standard deviation (σ), is taken for each set of readings, where

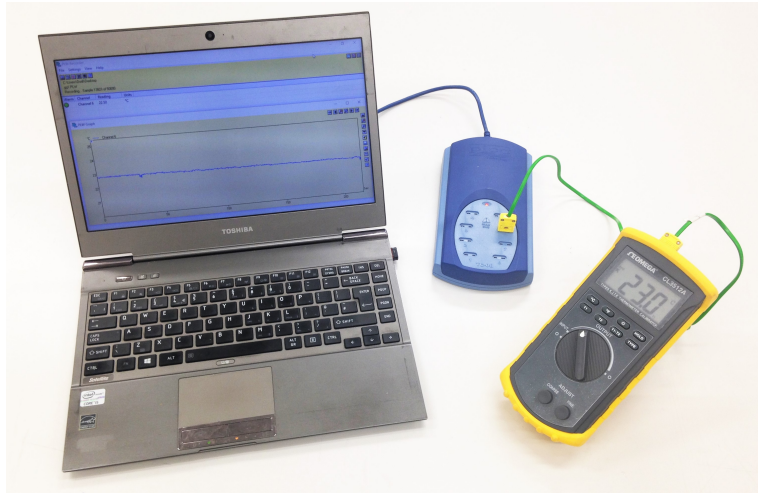


Figure 2: Calibration of thermocouples and data logger.

(σ) is used in instances where the uncertainty is associated with the measurements of a known value such as calibration of thermocouples. Standard deviation is calculated using Equation 1:

$$\sigma = \sqrt{\frac{\sum(x - \bar{x})^2}{n - 1}} \quad (1)$$

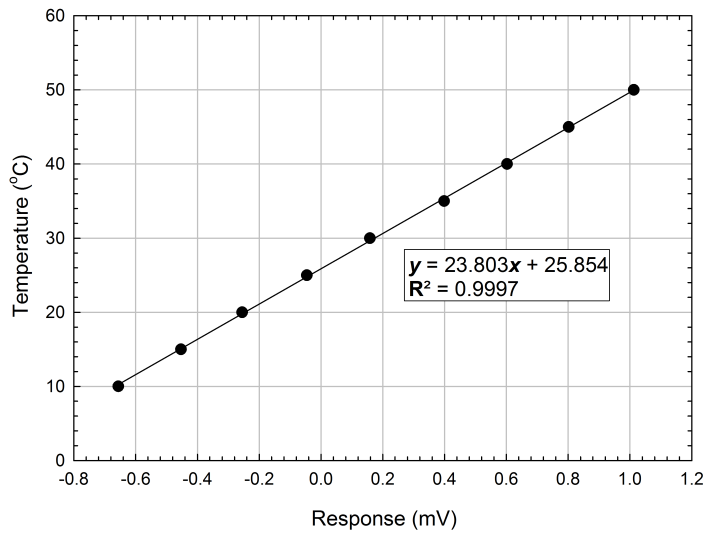


Figure 3: Calibration curve for thermocouples.

The °C error at each temperature is calculated using the gradient of the calibration curve, as shown in figure 3. The error is calculated as a percentage of the reference temperature provided by the OMEGA thermocouple source simulator. Calibration data for thermocouple are summarised in Table 2.

Table 2: Calibration data for 1.5 mm thermocouple.

Ref	TC ₁ (mV)	TC ₂ (mV)	TC ₃ (mV)	TC ₄ (mV)	Average (mV)	Standard Deviation (mV)	Standard Deviation (°C)	Uncertainty
10	-0.655	-0.658	-0.653	-0.658	-0.656	0.00245	0.058	0.58%
15	-0.449	-0.455	-0.45	-0.453	-0.420	0.00275	0.066	0.44%
20	-0.250	-0.257	-0.254	-0.259	-0.255	0.00392	0.093	0.47%
25	-0.048	-0.046	-0.047	-0.043	-0.046	0.00216	0.051	0.21%
30	0.158	0.163	0.152	0.157	0.158	0.00451	0.107	0.36%
35	0.397	0.404	0.400	0.395	0.399	0.00392	0.093	0.27%
40	0.604	0.605	0.601	0.610	0.605	0.00374	0.089	0.22%
45	0.805	0.813	0.799	0.804	0.805	0.00580	0.138	0.31%
50	1.013	1.007	1.018	1.001	1.010	0.00737	0.175	0.35%

Preparation of SEM Samples Using Sputter Coater

The standard coating procedures using POLARON sputter coater is as follow:

Before placing the samples in the vacuum chamber, check the LEAK valve is closed, and Argon gas regulator is open and set the pressure to 0.7 bar. Then, shut the sputter coater lid and press the MANUAL button. Set the coating time for 30 seconds and 1.5 KV respectively before starting the rotary pump by pressing the START SEQUENCE button. After that, the chambers pressure metre will fall to about 10^{-1} mbar where the LEAK valve will open for 5 seconds purging the system with a processing gas. The system will continue to pump down.

When reaching an ultimate pressure approximately 1×10^{-2} mbar, operate the START button to start the coating process in which the plasma will strike, and the sputtering process will deposit target material on the base plate. On completion of the sputtering process, the plasma discharge will extinguish, and the END indicator will illuminate.

To vent the system, press and hold the VENT/STOP button. The Vent indicator will illuminate, and the rotary vacuum pump will stop, and the chamber will be vented to Argon gas. Wait for the chamber to pressurise and remove the coated samples. Shut the chamber lid and switch of the argon gas.

Preparation of DSC Samples

Preparation of DSC samples requires a precision microbalance placed on a stable table, latex gloves, tweezers crucible box with crucibles, a crucible ceiling press and DSC samples.

DSC samples are enclosed in a sample pan to avoid the direct contact between sample, furnace and sensor. Standard aluminium sample pans and covers from (PerkinElmer, USA) with the volume of 50 μl [163] were used. DSC sample consists of uncured Ethylene-Vinyl Acetate (EVA) sheet supplied from (STR solar, USA) with a thickness of 0.4 mm. Small discs were cut from EVA sheet to be used for the different experiments. The mass of a disc was typically about 10 mg.

The procedures for preparing samples for DSC measurements are as follow:

- Check the level of balance, the air bubble should be at the centre of the black circle. Then, tare the scale to zero with a crucible and a lid.
- Insert 10 mg of EVA disc into the crucible.
- Weigh the whole (crucible + lid + material) to determine the mass.
- Crimped pans improve the thermal contact between the sample, pan and disc, reduce thermal gradients in the specimen, minimise spillage, and enable retention of the sample for further study.